A detailed, stochastic population balance model for twin-screw wet granulation

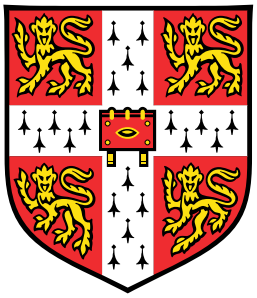

Andrew D. McGuire

Department of Chemical Engineering and Biotechnology

University of Cambridge

This dissertation is submitted for the degree of

Doctor of Philosophy

St Edmund's College May 2018

A detailed, stochastic population balance model for twin-screw wet granulation

Andrew D. McGuire

This thesis concerns the construction of a detailed, compartmental population balance model for twin-screw granulation using the stochastic weighted particle method. A number of new particle mechanisms are introduced and existing mechanisms augmented including immersion nucleation, coagulation, breakage, consolidation, liquid penetration, primary particle layering and transport. The model's predictive power is assessed over a range of liquid-solid mass feed ratios using existing experimental data and is demonstrated to qualitatively capture key experimental trends in the physical characteristic of the granular product.

As part of the model development process, a number of numerical techniques for the stochastic weighed method are constructed in order to efficiently solve the population balance model. This includes a new stochastic implementation of the immersion nucleation mechanism and a variable weighted inception algorithm that dramatically reduces the number of computational particles (and hence computational power) required to solve the model. Optimum operating values for free numerical parameters and the general convergence properties of the complete simulation algorithm are investigated in depth.

The model is further refined though the use of distinct primary particle and aggregate population balances, which are coupled to simulate the complete granular system. The nature of this coupling permits the inclusion of otherwise computational prohibitive mechanisms, such as primary particle layering, into the process description. A new methodology for assigning representative residence times to simulation compartments, based on screw geometry, is presented. This residence time methodology is used in conjunction with the coupled population balance framework to model twin-screw systems with a number of different screw configurations. The refined model is shown to capture key trends attributed to screw element geometry, in particular, the ability of kneading elements to distribute liquid across the granular mass.

Preface

I hereby declare that except where specific reference is made to the work of others, the contents of this dissertation are original and have not been submitted in whole or in part for consideration for any other degree or qualification in this, or any other University. This dissertation is my own work and contains nothing which is the outcome of work done in collaboration with others, except as specified in the text and Acknowledgements.

This dissertation contains approximately 55,000 words, 33 figures and 10 tables. Some of the work in this thesis has been accepted for publication. These publications are:

1. **Andrew D. McGuire**, Sebastian Mosbach, Kok Foong Lee, Gavin Reynolds and Markus Kraft. A high-dimensional, stochastic model for twin-screw granulation Part 1: Model description. *Chemical Engineering Science*, (in press).

2. **Andrew D. McGuire**, Sebastian Mosbach, Kok Foong Lee, Gavin Reynolds and Markus Kraft. A high-dimensional, stochastic model for twin-screw granulation Part 2: Numerical Methodology. *Chemical Engineering Science*, (in press).

Other work not included in this thesis:

1. **Andrew D. McGuire**, Kok Foong Lee, Maksym Dosta, Sebastian Mosbach , Jan-Georg Rosenboom, Stefan Heinrich and Markus Kraft. Compartmental residence time estimation in batch granulators using a colourimetric image analysis algorithm and Discrete Element Modelling. *Advanced Powder Technology*, 28:2239 - 2255, 2017. doi:0.1016/j.apt.2017.06.005.

2. Kok Foong Lee, Maksym Dosta, **Andrew D. McGuire**, Sebastian Mosbach, Wolfgang Wagner, Stefan Heinrich, and Markus Kraft. Development of a multi-compartment population balance model for high-shear wet

granulation with Discrete Element Method. *Computers and Chemical Engineering*, 99:171–184, 2017. doi:10.1016/j.compchemeng.2017.01.022.

Andrew D. McGuire
May 2018

I would like to dedicate this thesis to my loving parents.

Acknowledgements

I would like to begin by thanking my supervisors, Dr Sebastian Mosbach and Prof. Markus Kraft for giving me a home in the CoMo group and without whom this thesis would not have been possible. Throughout my time in the group, Sebastian has always been willing to lend his expertise in numerical methods and programming in discussions on which this thesis was born. I owe a great debt to both of my supervisors for proof reading many iterations of the preprints which went on to become the chapters of this work. On numerous occasions, Sebastian has aided me with his uncanny ability to find botched reference formatting. I would like to extend my gratitude to all members of the CoMo group, who provided a wealth of encouragement, intellectual stimulation and technical expertise throughout my time at Cambridge. In particular, I thank Eric Bringley and Chung Ting Lao for those late nights at the white board in Pembroke street, and later at Philippa Fawcett Drive. The CAD diagrams of twin-screw devices in Chapters 2 and 7 were kindly provided by Jochen Dreyer. I also thank Jethro Akroyd, Radomir Slavchov, Nick Eaves, Astride Boje, Gustavo Leon, Jacob Martin, Angiras Menon and Janusz Sikorski for their continued support.

A number of people outside the CoMo group have generously given up their time to enable the realisation of many of the ideas in this thesis. At CMCL, I extent my gratitude to Kok Foong Lee (whose work this thesis extends), Daniel Nurkowski, for many an in-depth conversation at the tea table and George Brownbridge, for his heroic technical support with MoDS. I am also indebted to Dr Sebastian Mosbach and Dr Robert Patterson for lending their expertise in stochastic methods in many useful discussions and whose own work continually served as an invaluable resource. I owe a great deal of thanks to Prof. Gavin Reynolds at AstraZeneca for sharing his extensive knowledge of granulation processes, both theoretical and experimental.

I am lucky to call Liam Wilbraham and Fraser Baigent friends. Both of these people not only supported me in the completion of this work, but also expanded my knowledge of music, politics, technology and beyond. I also thank the gang at 92 Milton Road, who, though years of mutual toil, became a second family to me. To my undergraduate supervisor, Dr Leo Lue, I owe a wealth a gratitude. Dr Lue introduced me to the field that brings me such joy and, over the years, has helped me develop not just as a researcher, but as a person. For that, I am eternally grateful.

I would also like to thank the EPSRC and AstraZeneca for providing the financial support that made this work possible.

I am indebted to my partner, Mairi Urquhart, who has continued to stand by my side through this journey. Without her unfailing support, none of this would have been possible. Finally, I thank my parents, whose hard work and unshakeable faith in my abilities have led me to where I am today.

Table of contents

List of figures

List of tables

Chapter 1

Introduction

1.1 Motivation

Granulation is the transformation of particles into larger aggregates. This process has a rich industrial history, particularly within the pharmaceutical industry. Traditionally, granulation has been carried out as a batch process, however, recent changes in regulations have afforded the use of more dynamic, continuous processing techniques. One such continuous granulation technique under active use and development is twin-screw granulation. Twin-screw granulation has a number of inherent benefits over traditional batch granulation, however, in order for these benefits to be realised, and such that manufacturers comply with regulations, the underlying processes must be understood. Until quite recently, twin-screw granulation remained something of a black box process, though a plethora of experimental studies over the past few years have begun to shine some light on mechanisms at work. Despite these efforts, the process is still not fully understood, certainly when one considers the catalogue of knowledge that exists for more established, batch granulation processes. To exacerbate this situation, the potential variability in the operation of twin-screw devices makes process optimisation impractical.

Detailed models of twin-screw granulation would permit the rapid optimisation of process operating conditions based on some target product specification. These models would ideally have the ability to predict key granular attributes such as size distribution, porosity and active ingredient distribution for arbitrary device operating conditions. Such models could be inverted and used within model-based control systems to ensure that product material remained within the

specification. A model that can achieve all of the above must also do so in within an acceptable time-frame for it to be useful.

Process models for twin-screw granulation have been adapted from their batch granulation counterparts and have begun to deliver qualitative agreement with experimental data. Most existing twin-screw models simulate the process using population balance equations, which are solved using variations of the sectional method. With the sectional approach, the composition space (i.e. the amount of solid, liquid, gas in a particle) is mapped onto a discrete grid, transforming the problem to the solution of a system of ordinary differential equations. A fundamental draw-back of this approach is that it is prohibitively expensive to track more than three particle components. As such, incorporating additional particle components (such as active ingredient content or spatial distribution of liquid in the particles) into the process model description requires some sort of coupling between the tracked and un-tracked particle properties. This technique, known as parameter lumping, can be useful in some circumstances, however, the appropriate choice of model is often unclear. Twin-screw population balance models have, in general, not yet achieved an acceptable level of predictive ability over significant operating ranges. Other twin-screw modelling efforts have employed machine learning on experimental data sets. This approach results in the generation of black box models that have performed relatively well, but have not shed any light on the underlying particle processes.

The stochastic particle method (SPM) for population balance models is a promising method for the construction and solution of twin-screw models with high-dimensional particle descriptions. SPMs eliminate the need for parameter lumping and have, in the past, been successfully employed in the simulation of batch granulation systems with up to five dimensions. The application of SPMs to twin-screw granulation still presents a number of difficulties. Firstly, the utilisation of additional tracked particle properties must still be integrated into the particle description by way of a physical model. Secondly, the implementation of new and existing particle mechanisms using SPM presents a number of numerical challenges that must be overcome, in order for resulting framework to be computationally feasible.

The **objective of this thesis** is to construct a detailed population balance model for twin-screw granulation using the SPM. This model will build on existing stochastic efforts that exist for batch granulation, and will include a number of new particle mechanisms that are inherent to twin-screw granulation processes.

In practice, this also requires the development of a number of numerical tools that permit such models to be solved in an efficient manner.

1.2 Novel elements of this thesis

This thesis presents the following **novel developments**:

- A new four-dimensional compartmental population balance model for twin-screw granulation is presented. A number of new particle mechanisms have been developed and a number of other particles mechanisms from existing stochastic batch granulation models have been adpated to twin-screw granulation. These include a new, high-dimensional interpretation of an immersion nucleation mechanism and an enhanced consolidation model.
- A stochastic weighted particle framework is constructed for the efficient simulation of the new population balance model. This framework includes a new stochastic implementation of the immersion nucleation particle mechanism. It also includes the formalisation of a new weighting algorithm for particle inception that is demonstrated to reduce the computational cost of simulation by up to two orders of magnitude. The sensitivity of the framework to newly introduced 'free' numerical parameters is assessed in detail.
- A new model framework is constructed which permits the simulation of different screw configurations through the inclusion of a novel method for assigning residence times to model compartments.
- Coupling of distinct primary particle and aggregate particle population balances is carried out. This permits the addition of a novel primary particle layering mechanism to the twin-screw process description in a computationally feasible manner.

1.3 Structure of the thesis

The remainder of the thesis is structured as follows: Chapter 2 introduces the background material. This includes a discussion of granule structure, processing methods and an overview of current experimental findings in the literature that

will be used to construct the new particle mechanisms of the model. This chapter also provides an overview of the existing frameworks for granulation modelling, followed by a discussion of the various numerical tools that exist to solve them.

Chapter 3 introduces the twin-screw population balance model that forms the foundation of this thesis. The model particle description is introduced and each particle mechanism within the model is described in detail. This chapter also considers the manner in which the twin-screw barrel is represented as a series of connected compartments within the model space.

In Chapter 4, the stochastic particle framework developed and used to solve the newly formulated population balance model is presented. This begins by an overview of stochastic particle methods and the motivation for selecting the weighted particle method used throughout out the thesis. This is followed by the introduction of the weighted population balance problem to be solved and the stochastic particle process associated with each of the physical particle mechanisms of the twin-screw model.

Chapters 5 and 6 are concerned with the performance of the new model framework. The new model is validated in Chapter 5 by assessing its predictive abilities over a range of liquid flowrates using an existing experimental data set. The experimental system to be simulated is described and the procedure for estimating unknown model parameters is established. A number of areas for further model development are identified. Chapter 6 provides a numerical investigation of the stochastic particle method described in Chapter 4. A number of existing and newly introduced, 'free' model parameters are investigated and optimised. In addition to this, an efficient algorithm for primary particle inception is established.

Chapter 7 is concerned with the enhancement of the model, based on the findings of Chapter 5 and 6. This involves the introduction of a novel layering mechanism to describe the interaction of large agglomerate particles and the primary particle phase. From a numerical perspective, this involves the construction of a separate population for primary particles and its coupling to the stochastic particle solver used for the agglomerate phase. This chapter also establishes a method for assigning compartment residence times in model representations of arbitrary screw configurations. The enhanced model is validated across a range of screw configurations using existing experimental data in the literature.

Finally, Chapter 8 summarises the conclusions derived from the thesis and suggests areas for future development, of both a mechanistic and numerical

nature. A nomenclature section and bibliography are located at the back of this thesis, together with a number of appendices that concern the various derivations relevant to this work.

Chapter 2

Background

This chapter serves to introduce the concept of a granule, identify the position of the granulation industry in the process chain of tablet manufacture, its applications to the pharmaceutical industry and beyond. Existing methods of granulation and more recent developments, including the use of twin-screw devices, are examined in brief. This is followed by a review of the existing body of experimental research into twin-screw granulation systems and the conclusions which can be drawn from this work. The chapter continues with a review of each of the key frameworks that have been employed in the modelling of granulation systems. This is followed by an examination of the various numerical methods that have been applied to simulate these models and a discussion of their various strengths and weaknesses.

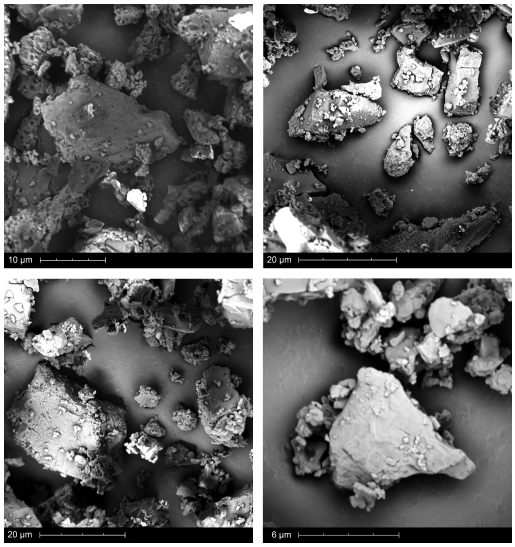

Fig. 2.1 Scanning electron microscope images of individual granules of α-lactose monohydrate formed using batch granulation. Source Rosenboom et al. [144].

2.1 What is a granule/granulation?

Granulation is the process of combining individual particles into agglomerates, from which the original component particles may still be identified [75]. In the case of wet granulation, the addition of a liquid binding agent provides a medium through which the individual particles may coalesce, through the creation of pendular bridges and capillary regions. Semi-permanent agglomerates are formed through the solidification of these bridges. Solidification can be driven by evaporation of solvent from the binder, cooling of molten binder, crystallisation or reaction between the solid and liquid components [50, 163]. This process yields larger agglomerated forms of the original powder, with some degree of porosity, such as those shown in Figure 2.1. Within the pharmaceutical industry, the original solid material will typically be a blend of various powders (known as excipients) and some active pharmaceutical ingredient (API). Common excipients include various grades of lactose-monohydrate, micro-crystalline cellulose and mannitol. Typical binder solutions include distilled water and water-based solutions of hydroxypropylcellulose (HPC). The granulation process results in particles which have a number of benefits over their constituent powder particles, including reduced caking and dust formation [75], improved flow properties for transport [159], controlled release of API [75], reduced segregation of components in transport [159] and improved tabletability.

2.2 Applications of granulation

The process of granulation is widely employed across industries including detergents, food stuffs, pesticides, fertilisers and pharmaceutical products [154, 164]. From an economic perspective Iveson et al. [75] reported that, in the chemical industry, 60% of products were manufactured as particulates and an additional 20% used powders as a feedstock, making the annual value of such products around $1 trillion as of 2001 in the US alone [49]. Within the context of the

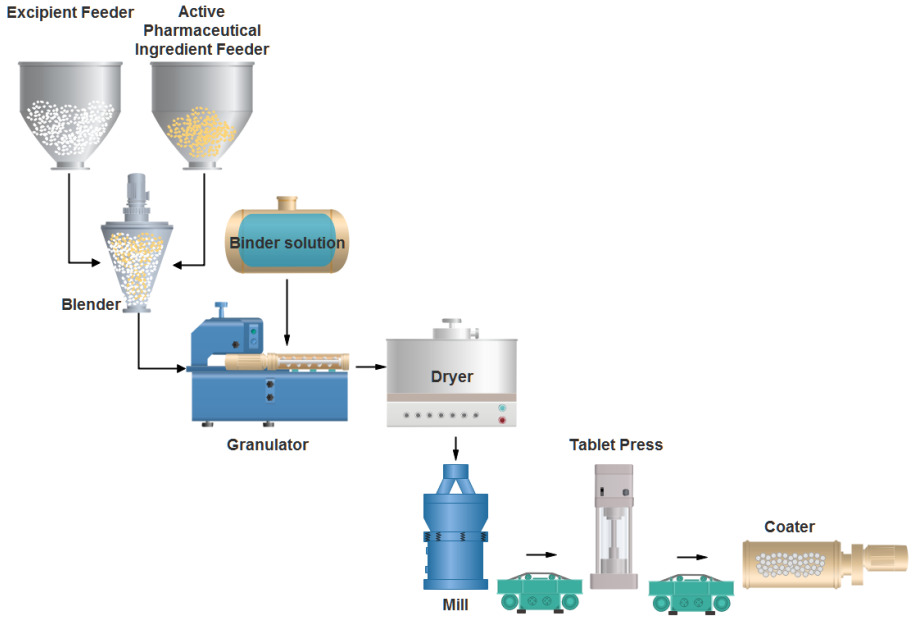

Fig. 2.2 Tablet production flow diagram featuring wet granulation.

pharmaceutical industry, granulation features as a critical step in the production of tablets, as depicted in the process train in Figure 2.2. In this case, the physical attributes of the granular product have a direct effect on the tabletability of the mixture, tablet strength [41] and, ultimately, the rate of release of the API in vitro and in vivo [109, 168].

2.3 Granulation as a unit operation

The granulation step (depicted in Figure 2.2) has traditionally been carried out as a batch operation, using equipment such as fluidised bed spray granulators and high-shear mixers. Alternatively the blending, granulation and drying stages are carried out in a the same vessel using single-pot processing devices [130]. The

use of batch systems was in-line with the quality-by-testing (QbT) regulatory framework put in place by United States Food and Drug Administration (FDA) and adopted across the world. Within the QbT framework, product quality is safeguarded through the testing of raw materials, consistency in the equipment employed, the configuration of the equipment and testing of the final product [93]. The situation changed in 2001, when the FDA announced a shift in its regulatory approach [51], which was subsequently added to again by the FDA and other regulation authorities [52, 53, 69–71]. The new framework encouraged quality assurance by design of the processes known as Quality-by-Design, QbD [56]. QbD promotes the use of control strategies, the employment of mathematical tools to design experiments, model processes and the use of continuous improvement tools to ensure increased product quality over time [105]. The promotion of QbD, and the newly gained flexibility it afforded in production methods, encouraged the use of continuous processing methods for granulation. Continuous granulation devices offer a number of advantages over their batch counterparts, namely:

- The ability to implement online process control, permitting consistently high quality product and reduced wastage [80, 143] - which the pharmaceutical industry is known to be particularly poor at achieving [75, 143]
- Ease of scale up [98]. The same equipment can be used in the formulation development stage and industrial stages, eliminating the need for numerous scales of device that are often required in the case of batch granulation.
- Reduced plant footprint. Continuous devices are often much smaller than their batch counterparts.
- A reduction in the cost of increasing production capacity to meet market demand: The capital cost of adding larger or additional batch systems generally comes at a high capital cost [170].
- Reduced API consumption during formulation development stage, where the amount of raw material can be limited. [169]
- Reduction in equipment down-time associated with product removal and device cleaning in batch systems. This is particularly true when the same product is being manufactured using the same batch equipment over multiple batches.

Although it has been demonstrated that, in general, continuous granulation has economic benefits over traditional batch granulation [149], there are some

drawbacks to consider. Most important of which is the loss of the product containment inherent to batch methods, which permits off-specification batches to be isolated [98, 170]. Other draw backs include the loss of predictability in terms of process behaviour and the inability to directly lean on the large body of batch granulation research.

2.3.1 Methods of continuous granulation

A number of devices for the continuous granulation of powders are currently utilised in an industrial context [170]. These include continuous fluid bed granulators, spray driers, so-called instant agglomerates (generally a high speed turbine into which powder and liquid are separately fed with continuous outflow). Other continuous devices such as roller compactors are attractive as they do not require a drying stage after the agglomerates have been formed [79]. A number of semi continuous systems also exist, such as the linking of high-shear batch systems to fluidised bed driers in series [98]. In addition to these methods, alternative extrusion based devices have been developed and employed for the purposes of continuous granulation. The device with which this thesis is concerned is twin-screw granulation and its description is the subject of the next section.

2.3.2 A closer look at twin-screw granulation

Twin-screw granulation (TSG) is a relatively new method of continuous granule production. The process itself was originally developed from melt extrusion granulation devices. Extrusion devices may use a single or double screw configuration to convey the material and drive the particle processes that ultimately result in a granular product. The screw barrel is equipped with a die plate at the material exit to reduce the number of oversized agglomerates. The resulting granules are then generally passed to a drying stage (such as a fluidised bed dryer). In some cases the extrusion uses a molten form of binder to facilitate the agglomeration of the powder feed. The molten binder solidifies upon exit of the device leading to rigid granules. Screw based devices have a number of desirable qualities over alternative forms of twin-screw granulation devices, namely the ability of the high-shear environment of the screw to create granules with very high drug loading [114] and the fact that the device can be considered self-cleaning [169]. Lindberg et al. [102, 103] appear to be the first to employ a twin-screw extruder for the purposes of granulation. This involved the testing

Fig. 2.3 ConsiGma™-1 twin-screw granulator from GEA Pharma Systems, featuring powder and liquid feed systems, controllers and a semi-continuous fluidised bed drier system. Source [57].

of such a device, with and without the use of the die plate, in the preparation of granules composed on anhydrous citric acid and sodium bicarbonate using an ethanol binding agent. This technology was later investigated by Keleb et al. [78], who noted that the product quality from such twin-screw granulation devices was highly reproducible. At this point the technique of twin-screw granulation began to gain traction within the research community and the use of this technology in a continuous processing line has been the subject of at least one patent [58]. Before the key studies within this body of research are reviewed, the configuration of a typical twin-screw device and its implications to formulation development in the pharmaceutical industry are considered.

Figure 2.3 shows an example of a commercial twin-screw granulation unit with mass and liquid feeders, device controller, and fluidised bed. Figure 2.4 highlights the internal configuration of part of the twin-screw itself. From this figure, one sees that each screw is composed of a number of elements in sequence. This sequence defines what will be referred to as the screw configuration. Powder is continually feed to the start of the screw barrel and, in the case of wet granulation, the binder is introduced in the form of liquid droplets via one or more ports along the length of the screw. This provides a natural divide in the device. The section of the screw that is positioned prior to the liquid addition port (relative to the direction of powder flow) is termed the metering zone and that after the liquid addition port is known as the variation zone. In the metering zone the screw is typically constructed from conveying elements, to transfer material to the variation zone. Within the variation zone a number of different elements are typically employed, the most common of these are conveying elements (CE),

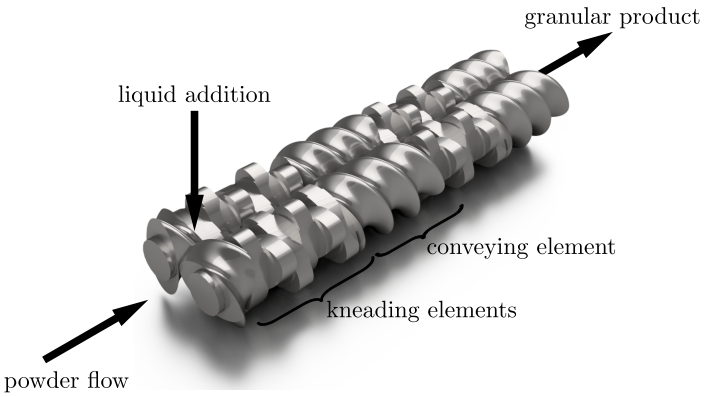

Fig. 2.4 Variation zone of a twin-screw granulator.

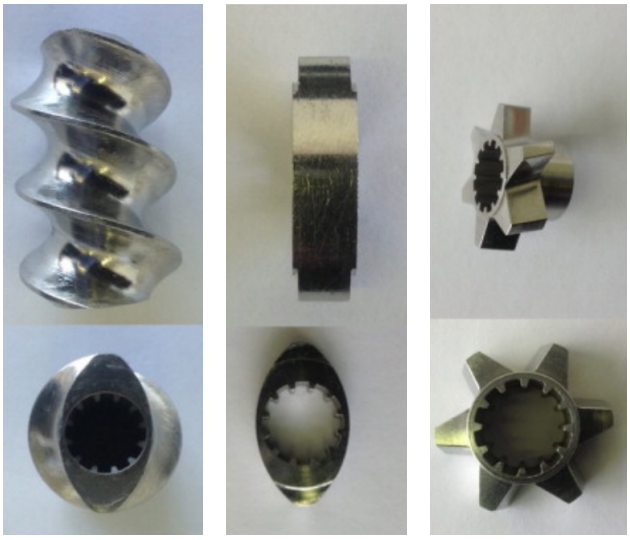

(a) Conveying (b) Kneading (c) Mixing

Fig. 2.5 Common twin-screw element geometries. Source [169]

kneading elements (KE) and mixing elements, also know as distributive mixing elements (DME), each of which is shown in Figure 2.5.

Each type of element acts differently on the particle mass as it passes through. Thus, the screw element configuration may be altered to produce a granular product with different physical properties. The screw speed, liquid feed rate and powder feed formulation may also be varied in this way, resulting in a system with an exceptionally large operating space. Conservative estimates of the number of different variation zone configurations that can be constructed, using the common elements depicted in Figure 2.5, is greater than two million. It is therefore unfeasible to search any appreciable fraction of this operating space during formulation development. Instead, testing is generally limited to screw

configurations that are composed primarily of conveying elements and a handful of kneading and mixing elements. The inability to quickly optimise the operating space by exhaustive search means that the roles of each screw element and the process sensitivity to other operating variables (such as feed formulation, liquid flowrate etc.) must be understood at a particle level. This information can then be used to intelligently optimise the set-up of the device, by effectively narrowing the search space, or, in line with the focus of this thesis, drive the development and construction of twin-screw process models that can be used to predict key product attributes for arbitrary device operating conditions. Taking this even further, these models could then be employed in model-based dynamic control systems to continuously monitor and correct deviations in product quality in an in-line fashion [157].

2.4 Experimental investigations of twin-screw granulation

Before considering the critical features that a model for twin-screw granulation must contain, it is important to first understand what is known about twin-screw systems from an experimental perspective.

In recent years, numerous experimental studies have been carried out to investigate many aspects of TSG. This review begins by focusing in on the role of the screw configuration and the effect of using different types of element in TSG processes. This subject has been tackled in depth by numerous groups and at various scales. The most large scale study to date, in terms of screw configurations tested, was carried out by Vercruysse et al. [167]. In that study, the authors used many different screw configurations whilst fixing and varying other operating conditions, to assess the effect of the number and position of certain element types on the particle size and liquid distributions. This study, and others [99, 106], concluded that kneading elements aided the distribution of liquid within the granular mass, by squeezing the internal liquid in large agglomerates to the surface, promoting further growth. This was observed to shift the distribution from highly bi-modal distributions (for pure conveying screws) to narrower, sometimes mono-modal distributions [165, 167]. However, these studies have generally used a fixed formulation (excipient material, liquid-solid feed ratio etc.), so it is hard to gauge the generality of the results. Furthermore, by extracting material only at the end of the barrel, it becomes difficult to assess the role of specific elements.

Li et al. [99] addressed this issue by taking samples from positions between the start and end of the variation zone. Using this method, the authors again found the role of kneading elements to be the distribution of binding agent and compaction as well as fragmentation of agglomerates. It was concluded that this effect permitted further fragmentation of particles down-stream from these elements.

An number of experimental investigations into the breakage processes in twin-screw devices [47, 86, 106, 138, 167] have highlighted the role of screw element geometry on the breakage dynamics along the barrel. Sayin et al. [147] performed experiments in which the liquid addition port was placed very close to the end of the screw barrel, allowing the element-specific effects to be observed in isolation. Although useful information can be gathered from such studies, Li et al. [99] noted that the effectiveness of an element in changing the physical attributes of the material passing through it is very much dependent on the state of the material entering the element. This again puts in question the generality of results derived from elements in isolation. Nevertheless, several studies [106, 138] have shown that the large agglomerates in conveying elements undergo size reduction through cutting or edge chipping, where small fragments are continually taken from the edge of the agglomerates. No daughter distribution breakage data is currently available for kneading elements, however, based on their somewhat similar geometry, it is expected that the primary breakage mechanism in these elements will be similar to that in distributive mixing elements (DME) [147]. The particle size distribution transformation induced by DME work by Pradhan et al. [138] suggests that breakage in these elements occurs through a combination of crushing and chipping [138]. Hence, it is hypothesised that the primary breakage mechanisms in kneading elements will be the crushing behaviour observed in DME, with less emphasis on the chipping mechanism, due to the absence of the pronounced blades that are present in DME.

In addition to the investigation of screw configuration effects in TSG, a number of authors have also looked at how the granular material flows through twin-screw devices. Works by Dhenge et al. [38] and Kumar et al. [88] have investigated the residence time distribution of particles in TSG devices using chemical imaging techniques. Both studies found that the residence time distributions feature a particularly long tail, indicating that material becomes ‘stuck’ to the barrel wall and/or screw elements and is slowly released over a long period, relative to the mean residence time. It was noted by Kumar et al. [88] that the screw speed had a distinct effect on the mean residence time, though the number of kneading

elements also had a marked effect. Further work by Kumar et al. [89] went on to conceptualise these residence time distributions as a series of ideal reactors. It was noted that the kneading zones could be represented as plug flow zones, whereas conveying zones could be represented as well mixed tanks attached to 'dead-zones' representing the 'stuck' material. The resulting flow model demonstrated good agreement with experimental residence time data.

The distribution of mass in the twin-screw devices was investigated using Positron Emission Particle Tracking (PEPT) by Lee et al. [97] and further investigated by Seem et al. [151]. Lee et al. [97] showed that the residence time of kneading elements was around twice that of conveying elements (for the operating conditions tested). Furthermore, the authors showed that the fill level of kneading elements was significantly higher than that in conveying elements, though the level of disparity was strongly related to the operating conditions. Seem et al. [151] observed that the fill level also varied between the two screws, with the so-called driving screw holding much more material than the loading screw in conveying zones.

Moving away from screw geometry effects, it is noted that non-screw geometry based operating parameters such as binder properties and the liquid-solid mass feed ratio (LSR) also have a strong effect on the product granular state. Dhenge et al. [38] found that binder viscosity affected the fill ratio of the screw barrel. Furthermore, it was noted that more viscous binder solutions were able to shift the particle size distributions (PSDs) from a bi-modal state with a small mean size, to mono-modal state with a much larger mean size. It was hypothesised that this occurred as the liquid bridges grew in strength, resulting in less breakage and less pronounced bi-modality. Dhenge et al. [38] and also noted that there is a tendency for high LSR to form mono-modal peaks. This is due to an increase in the number of liquid bridges that can be formed, resulting in stronger granules, higher material hold-up and higher residence times. These factors lead to increased levels of surface liquid (through particle consolidation or squeezing), which enhances the rate of adhesion of primary particles onto agglomerates, known as layering. El Hagrasy et al. [46] looked at the effect of varying the LSR with several excipient materials and, for the screw configuration investigated, observed that increasing the LSR caused the PSD to shift from sharp agglomerate peaks with a high percentage of fines (undersized or un-granulated material), to mono-modal and finally to bi-modal.

Nucleation is known to be an important process in the context of twin-screw granulation. It is generally agreed upon [38, 40, 47, 106, 124] that this occurs as an immersion nucleation process [75] in TSG. This follows from the fact that incepted liquid droplets are much larger than the excipient powder which they are being dropped onto. This process was investigated in detail for TSG systems by Ai et al. [1].

Finally, to explore the importance of the excipient material in TSG, Willecke et al. [175] performed a principal component analysis on nine excipient types and grades of commercial interest. The authors found that excipient flow-related properties: density and particle size-related properties; charge and adhesion properties and moisture-related properties all played an important role in determining the physical attributes of the granular product.

2.5 Modelling of high-shear granulation systems

This section provides an overview of high-shear granulation modelling techniques, firstly from the particle level (particle descriptions and transformation mechanisms) and secondly from the process description level (i.e. the frameworks in which the particle model may be embedded and the manner in which the granulation device may be represented in the model space).

2.5.1 Modelling at the particle level

The construction of a useful model for a process such as high-shear granulation requires knowledge of the underlying process mechanisms [75]. In general, these mechanisms are not well-established for twin-screw granulation and hence, in order to formulate such a model, it is essential to familiarise oneself with existing mechanistic descriptions of batch and continuous granulation processes (including twin-screw) and their associated particle representations. As mentioned at the beginning of this chapter, granules may be composed of a mixture of solid materials, with some degree of internal porosity. Pore regions are generally viewed as a mixture of trapped gas and liquid volumes. These particles may also have a degree of surface liquid than can permit adhesion of contacting particles and growth of the granules. Together, these properties form a hypothetical particle representation, such as that illustrated in Figure 2.6. Ennis [48] outlined the

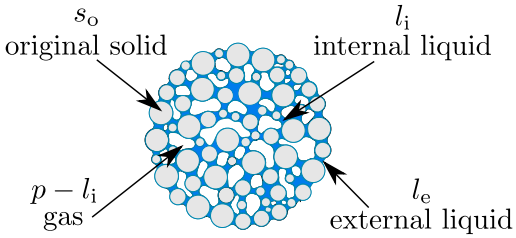

Fig. 2.6 Particle description.

four key rate processes that occur in granulation as wetting or nucleation, coalescence or growth, consolidation and densification. Iveson et al. [75] provided an in-depth review of these mechanisms and discussed how existing knowledge from alternative areas of chemical engineering could be utilised to model those mechanisms that had not yet been studied in depth in the context of granulation. Iveson et al. [75] partitioned the mechanisms into the following three stages:

Nucleation and wetting

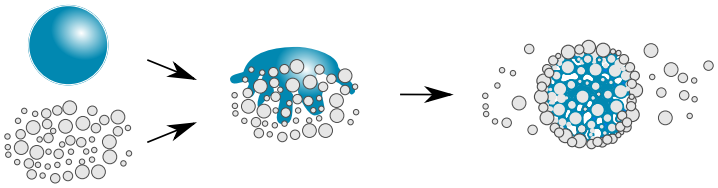

Fig. 2.7 Immersion nucleation process. Adapted from [75].

This is the process by which the binder comes into contact with the dry feed powder bed. The liquid travels through the voids between granules under the force of gravity or capillary forces. In doing so the liquid interacts with the feed particles which combine with the liquid to form nuclei particles [75, 172]. The area within which the nucleation occurs is termed the nucleation zone, droplet zone, wetting zone or spray zone. The properties of the resulting nuclei are a strong function of the solid-binder properties, mode of droplet inception and the rate of agitation of the powder bed at this stage [104, 174].

The formation of nuclei within granulation processes is generally modelled as a droplet incident on and subsequently penetrating into a porous particle bed. The rate of liquid penetration is then estimated using the Washburn equation, which takes into account the capillary pressure driving force, coupled with a viscous dissipation factor. For the case where constant drawing area (i.e. constant drop

radius) is assumed, the penetration time τ_{pen} takes the form [34]:

$$\tau_{\text{pen}} = \frac{2v_{\text{drop}}^2}{\pi^2 \varepsilon_{\text{surf}}^2 r_{\text{drop}}^4 R_{\text{pore}}} \frac{\mu}{\gamma_{\text{LV}} \cos\theta}, \tag{2.1}$$

where v_{drop} is the droplet volume, $\varepsilon_{\text{surf}}$ is the surface porosity, r_{drop} is the radius of the droplet footprint on the powder surface, R_{pore} is the effective pore radius, γ_{LV} is the liquid surface tension, μ is the binder viscosity and θ is the solid-liquid contact angle. Hapgood et al. [65] and Iveson et al. [75] note that bed penetration times are negligible in cases where the binder viscosity is low and a wetting liquid is used (such as water-lactose mixtures).

The binder delivery method (i.e. the size and rate of liquid droplets hitting the powder bed) is known to have a strong effect on the size of nuclei distribution. The binder addition conditions and the resulting nuclei formation kinetics are typically viewed within a regime map with two areas (with an intermediate zone) such as that presented by Hapgood et al. [65]. The two regimes are distributive nucleation and immersion nucleation [75, 150]. The distributive mechanism is dominant in cases where the droplet size is similar to that of the feed powder. As a result, the binder is spread over many particles and these particles transfer liquid between each other and coalesce as they are brought into contact with each other by the mechanical action of the granulation device [75]. Immersion nucleation (Figure 2.7) was briefly touched upon in Section 2.4 and noted to occur when the droplet size greatly exceeds that of the primary powder. In this way, the small feed powder particles disperse into the large droplet particle. Therefore, in this regime, the size of the nuclei is a strong function of the size of the droplets being introduced.

In TSG, liquid is introduced via relatively large ports (nozzles) which can be several millimetres in diameter [46] whilst primary particles are typically of the order of 10 to 100μm. Hence, primary agglomerates are generally formed by way of immersion nucleation [37, 38, 151]. It is hypothesised that these liquid-rich primary agglomerates (or nuclei) are subject to compaction and breakage, particularly in kneading elements, as described by the destructive nucleation mechanism of Vonk et al. [172]. Within the TSG modelling community, the nucleation mechanisms are often ignored (see [7, 87]) and liquid is simply added to all particles in the liquid addition zone, weighted by some parameter such as solid volume (see [7]). A notable exception to this statement is the work by Barrasso and Ramachandran [12], who modelled the TSG nucleation

processes as penetration into a porous bed as described by Iveson et al. [75]. In this model, the droplets entering the system can either form a single nucleus or wet existing agglomerates (depending on the volume fraction of agglomerates within the nucleation zone). The resulting nuclei are saturated with liquid (liquid-solid ratios at the point of saturation are material dependent) and have a porosity which is equal to the voidage of the particle bed.

Growth and consolidation

The growth of primary particles, nuclei and nuclei fragments occurs through contact and collisions between particles in the granulation device. The rate at which binary collisions occur between two particles with specific properties (volume, aspect ratio etc.) is captured by a construct known as a collision kernel K_{col}. Given particles x and y, these kernels generally take the form

$$K_{\text{col}}(x,y) = \beta_0 C(x,y), \tag{2.2}$$

where β_0 represents the contribution from process parameters such as impeller or screw speed (generally a semi-empirical function which may or may not have a spatial or time dependence) and $C(x,y)$ is a collision rate function which dictates how the properties of the collision pair (such as their respective particle diameters) influence how often they will collide with each other. Numerous forms of $C(x,y)$ exist for high-shear granulation collision modelling, some rooted in kinetic theory and others of a semi-empirical nature. Excellent overviews of the existing kernels for high-shear granulation is provided by Kumar et al. [85] and Reynolds et al. [141].

The coagulation kernel determines the rate at which particles x and y coagulate (also termed coalescence). This is defined as

$$K_{\text{coag}}(x,y) = K_{\text{col}}(x,y)\mathbb{1}_{\{x,y|\mathcal{S}(x,y)\}}(x,y), \tag{2.3}$$

where $\mathbb{1}_{\mathcal{A}}$ is the indicator function on set $\mathcal{A}$ and $\mathcal{S}$ represents some criterion that determines whether a collision results in coalescence of the particles involved. Iveson [73] notes that there are two classes of thought regarding successful coalescence:

Class I particles may move freely within the granulator and colliding particles may coalesce if and only if the kinetic energy of the collision pair can

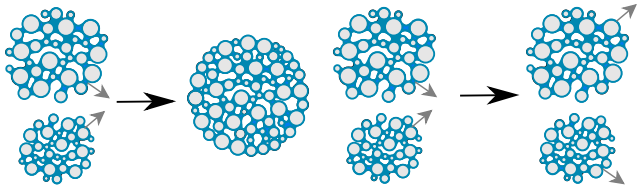

(a) Coalescence (b) Rebound

Fig. 2.8 Class I collision model outcomes.

be dissipated by the particles. The bonds are considered permanent. See Figure 2.8.

Class II particles form a permanent bond only if they come into contact for long enough such that a bond can be formed. This bond must be strong enough to withstand subsequent impacts.

Existing high-shear granulation models tend to adopt the Class I approach due to the relative ease of implementation. In such cases, the physically based Stokes criterion [50] (discussed in more detail in Chapter 3) is typically used as $\mathcal{S}$ [12, 19].

Within the Stokes criterion, the ability for the particles to dissipate the collision energy is partly controlled by the amount of surface liquid present. The amount of surface liquid can change through processes including particle consolidation (Figure 2.9(a)), penetration of liquid into pore through capillary forces (Figure 2.9(b)) and the reduction in total particle surface area associated with coalescence. Particle consolidation may occur as particles collide with other particles, impellers or walls of the granulation device. This in turn reduces the porosity of the particles and can squeeze liquid to the particle surface. As previously mentioned, several TSG experimental studies [38, 47, 152, 167, 168] have concluded that internal liquid is squeezed to the surface of nuclei and nuclei fragments in areas of high compaction such as kneading blocks.

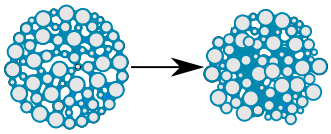

(a) Consolidation, also known as compaction, leads to a reduction in particle porosity. This may lead to an increase in the fraction of pore volume occupied by internal liquid and/or an increase in the available surface liquid volume.

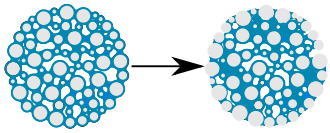

(b) Penetration involves the transfer of external liquid to the particle interior. This subsequently increases the fraction of pore volume occupied by liquid.

Fig. 2.9 Consolidation and intra-particle liquid distribution mechanisms.

Fragmentation

Fragmentation (depicted in Figure 2.10), also known as breakage or attrition, is the size reduction of granules. This occurs as the particles come in to contact with the walls, agitation device (impeller, screw etc.) or other particles within the granulator. Kumar et al. [85] notes that research into the fragmentation mechanisms within high-shear granulation is still in its infancy, relative to other mechanisms such as coagulation. From a modelling perspective, the fragmentation process can be described as a combination of a breakage kernel and a daughter distribution. The former describes the propensity for a particle to break. The latter describes the probability distribution on the space of fragment sizes or states. As in the case of coagulation, the breakage kernel may take into account the properties of both the particle (such as size, porosity, material etc.) and the granulation environment (such as the agitation rate). A review of existing high-shear breakage kernels, from the semi-empirical to the mechanistic, is presented by Kumar et al. [85].

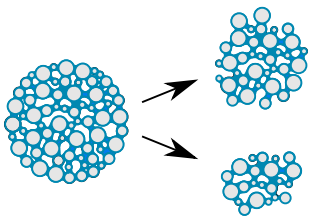

Fig. 2.10 Breakage/fragmentation mechanism.

Within TSG modelling, the breakage kernel $g_{\text{break}}(x)$ usually derives from the form presented by Pandya and Spielman [129], originally used to describe the

splitting of Koalin-hydrous ferric-oxide flocks. This has the form

$$g_{\text{break}}(x) \propto k_{\text{att}} v(x)^{\omega_{\text{att}}}, \tag{2.4}$$

where x represents the particle description, k_{att} is some breakage rate constant that may be a function of the agitation rate (such as screw speed), $v(x)$ is the particle volume and ω_{att} is a scaling parameter. Barrasso et al. [7] and Kumar et al. [87] both used breakage kernels of the form in Equation 2.4 to describe the breakage process within twin-screw granulation models, though the combination of multiple mechanisms in these studies makes it difficult to deduce the effectiveness or suitability of such kernels.

The breakage of a physical granule may result in the production of many fragments, however, from a model perspective, breakage is usually viewed as the splitting of a particle into two fragments. No purely theoretical work has been done on the formulation of daughter distributions in TSG. Instead, the distributions employed for TSG modelling are typically borrowed from other high-shear device models such as ball milling [4, 87] or, as in Barrasso and Ramachandran [12], the granules are assumed to be split into two fragments of equal size and composition.

2.5.2 Modelling at the unit operation level

Modelling of granulation processes at the unit operation level can be split into three main categories, namely: population balance modelling, the discrete element method (DEM) and so called black box models.

Population balance models

The temporal evolution of a system of particles, such as those in a granulator, due to nucleation, coalescence, fragmentation and other processes may be simulated using population balance models (PBM) [140]. In order to formulate such a model, a particle representation or type-space must be selected. The type-space provides a characterisation of any particle using a vector of components. Typically, within the field of granulation modelling, the particles are described using a one to five-dimensional particle representation. These dimensions describe the volume of each component that the granule is supposed to be constructed from. This can include un-reacted primary solid, solid that has reacted with

the binder, particle gas volume, internal and external liquid volumes. Although one-dimensional models are useful for model development, Iveson [74] has noted that one-dimensional models are ineffective in capturing distribution of properties across particle size classes, driving the developed of multi-dimensional PBMs.

A simple example of a one-dimensional population balance model, which only considers coagulation between particles, is the Smoluchowski coagulation equation [158]. Given some type space $\mathbb{X} = \mathbb{R}^+$, $x, y \in \mathbb{X}$ and particle number density n, the Smoluchowski equations reads:

$$\frac{\partial n(x,t)}{\partial t} = \frac{1}{2}\int_0^x K_{\text{col}}(x-y,y)n(x-y,t)n(y,t)\mathrm{d}y - \int_0^\infty K_{\text{col}}(x,y)n(x,t)n(y,t)\mathrm{d}y, \tag{2.5}$$

where, again, K_{col} is the collision kernel. Equation (2.5) has been extended to included the additional particle mechanisms associated with high shear granulation by a number of authors [20–24, 77, 108].

Historically, population balance-based modelling efforts in granulation have considered the granulator to be a single well mixed compartment with homogeneous processing conditions. However, in recent years, it has been shown that such single compartment representations can be inadequate and that multi-compartment frameworks can better capture effects that arise from in-homogeneous operating conditions [30]. To do so, the PBM is extended to include a spatial component. The device to be modelled is divided into a set of discrete compartments with pre-defined connection. Particles may then interact only with other particles located within the same compartment and transport mechanisms are constructed to permit the flow of particles between spatial zones. Compartmental PBMs have been constructed and simulated for high-shear batch granulation [9, 95, 96], silica nano-particle synthesis [116], Titania synthesis [16], coating as well as layering processes [100] and more. Such compartmentalisation is critical in TSG modelling due to variations in screw geometry (and therefore processing environment) along the length of the screw and the restricted back-mixing of material.

Compartmental PBMs for twin-screw granulation have been constructed and simulated by Barrasso et al. [7, 9], Barrasso and Ramachandran [12], Kumar et al. [85, 87]. These have ranged from one to three-dimensional models and have included nucleation, coalescence, fragmentation and layering mechanisms. A lumped parameter method is typically used to estimate additional particle properties beyond those explicitly tracked by the model [9]. This is achieved by

asserting a constant relationship between two or more particle properties (such as liquid content and porosity). Existing modelling efforts have been shown to capture observed trends in porosity and particle size distribution with key process variables. However, quantitative agreement with experimental data has proven much more difficult to achieve. The reason for this is most likely a combination of missing knowledge, in regards to the particle mechanisms in TSG, and secondly because the particle descriptions have remained simple (low in dimension). The restriction on the complexity of the particle description is a direct consequence of the traditional numerical methods employed to solve the associated multi-dimensional PBMs (further discussed in Section 2.6).

Although population balance models are an effective tool for granulation modelling, they require a number of key pieces of information to be known a-priori. Arguably, the most important among these are the collision kernel and transport rates between spatial zones. In order for the parameters to be estimated, PBMs for high-shear and fluidised bed granulation have been coupled to DEM [94] and, less frequently, Computational Fluid Dynamics (CFD) [101] simulations to create so called hybrid frameworks. Both uni-directional [94] and bi-directional [9, 42, 160] PBM-DEM couplings exist for high-shear granulation. In work by Barrasso and Ramachandran [12], the DEM stage was used to collect residence time data for each compartment, particle impact velocities (at the point of collision) and collision frequencies between particle types. The resulting hybrid model showed good agreement with experimentally observed trends between particle size and liquid distribution and changes in the screw configuration.

Even with the knowledge of collision and transport rates from DEM studies, complex granulation PBMs still have a number of unknown parameters, such as breakage rate constants. The presence of these unknown parameters require PBMs to be tuned against existing experimental data, which often involves massive scale parameter estimation efforts.

The Discrete Element Method

DEM simulations were not carried out in the context of this thesis, however, an outline of this method is presented here in brief since the technique has been applied in the context of high-shear granulation [54] and specifically to TSG modelling by other authors [9, 12], as noted in the previous section.

Unlike PBM, DEM simulations track the coordinates and momentum of discrete particles as they move around, driven by collisions with other particles and/or system boundaries and any force fields employed (such as gravity). Particle contact forces associated with particle-particle and particle-wall interactions are resolved by modelling the collision events as a spring, dash-pot and slider as described in [32]. Given such a model, the motion of each particle is solved through the integration of Newton's equations of motion. In general, DEM simulations do not consider the particle mechanisms involved in the granulation process (such as coalescence, fragmentation etc.), hence, they are typically employed within hybrid DEM-PBM frameworks. There are, however, some studies that have incorporated particle processes such as particle-particle liquid-transfer [155].

Traditionally, DEM particles have spherical geometry, though, in recent years, algorithms to handle more complex representations have been developed and employed to the modelling of particulate systems [83]. All existing PBM-DEM couplings for twin-screw granulation [9, 12] have used spherical particle representations within the DEM simulation, however, it is know that granules produced by TSG can exhibit large aspect ratios [36, 38, 63, 86, 115]. Hence, the resulting collision statistics and material flow characteristics may significantly differ from those of the real system. Another significant drawback of DEM is the computational cost of simulation. Simulations can take days or weeks to simulate a second of real time, making it ill-suited to massive scale parameter estimation required in the tuning of PBMs.

Black box Models

The high computational cost of DEM simulations has, in cases, incentivised their replacement with artificial neural networks (ANN) in the context of PBM-DEM couplings. Barrasso and co-workers [13, 14] demonstrated the use of an ANN (trained on DEM data) in PBM-ANN couplings. The resulting hybrid model was shown to reduce the computational cost of solution by several orders of magnitude (over pure PBM-DEM couplings), whilst maintaining the ability to predict key DEM data.

Recently, Shirazian et al. [156] modelled a twin-screw granulation system using a pure ANN approach. The network was trained against experimental size distribution data obtained using various screw configurations, screw speeds, LSR and mass feed rates. The authors showed that the resulting ANN was capable

of predicting key percentile diameters of the observed experimental PSD to a high degree of accuracy. Furthermore, the solution speed of this method means that it is suitable for use in model-based control systems for TSG. An obvious drawback of such an approach is that it does not give any real insight into the underlying mechanisms at work in TSG.

2.6 Numerical methods for population balance modelling

This thesis is concerned with the application of PBM to the simulation of TSG systems. The solution techniques for PBM can be placed into three main categories, namely: sectional methods, moment based methods and Monte-Carlo methods. In the following section, the principles of each of these numerical methods will be reviewed and instances of their application to high-shear granulation discussed. For an in-depth treatment of these methodologies and their applications to particulate process modelling, the reader is referred to the review by Kraft [84].

2.6.1 Sectional methods

Variations of the sectional method [90–92] are by far the most common technique for solving PBMs within the granulation community. This technique involves the discretisation of the type-space into a finite number of cells. Doing so approximates the PBM as system of ODEs (with respect to time) which can be integrated, using standard methods, to simulate the dynamics of the PBM [30]. Each particle that exists within each grid cell is then assumed to be identical, and hence, increased resolution (of the particle component distributions) requires a reduction in the grid spacing or adaption of the grid in the regions of interest.

Sectional methods are attractive due to the relative ease with which new mechanisms may be added. However, since the number of equations to be solved increases exponentially with the dimensionality of the particle representation, this technique is (generally) limited to the solution of PBM with at most three tracked particle dimensions. Examples of four dimensional PBMs for granulation do exist, but can take days or even weeks to solve using sectional methods [6, 10].

Within the granulation literature, sectional models have been employed in the solution of PBMs for drum and high-shear granulation [29, 30, 60, 137, 139], fluidised bed granulation [31, 119], continuous powder mixers [153], twin-screw granulation [9, 15, 87, 127] and conceptual systems within the context of parametric studies [11, 137].

2.6.2 Moment methods

The method of moments was pioneered by Karl Pearson in 1894 [136] and its application to particulate processes was demonstrated by Hulburt and Katz [68]. Within the class of moment methods, the full PBM is reduced to a finite set of moment equations, acquired by taking integrals of various moments of the full distribution. This is partly motivated by the fact that the full distribution of the particle system is not often required for the purposes of formulation development or process control. Hence, the knowledge of various integrals of the distribution is sufficient. For an in-depth review of the various classes of moment methods, see Müller et al. [125].

Application of moment methods to granulation has been limited. Wang and Cameron [173] used the method of moments to assess the viability of incorporating population balance models into model-based control for drum granulators. The technique was selected due to associated rapid computation times. It was shown that the moment models could produce results with acceptable degrees of accuracy but only permit the control of average particle properties. Furthermore, the technique still required knowledge of the shape of the particle distributions a-priori. This is acceptable in some granulation systems where log-normal distribution persist, but certainly not the case of twin-screw granulation, where distributions are highly non-ideal. Alopaeus et al. [3] used a simplistic granulation model as a test case in a study which investigated the numerical properties of several moments methods while Marchisio and Fox [110] applied moment based methods to model general particulate systems. This used PBMs with one and two internal coordinates that were closely related to granulation models in terms of the particle mechanisms present. To the best knowledge of the author, no studies have employed the method of moments to model twin-screw granulation systems.

2.6.3 Stochastic particle methods

An alternative method of solving population balance models, and the technique that will be applied throughout the remainder of this thesis, is the Monte Carlo (MC) particle method (sometimes referred to as MC-PBM or stochastic PBM). Under this framework, a representative sample volume of the system is modelled using an ensemble of computational particles. One implementation of the stochastic particle method is Direct Simulation Monte Carlo (DSMC), also know as the Direct Simulation Algorithm (DSA). In the DSA, each computational particle represents a single physical particle in the 'real' system. Each computational particle has an associated particle vector x that is used to characterise the physical particle it represents. In the case of granulation, this particle description may include the solid volume, various states of liquid volume and internal gas volume. A distinct advantage of Monte Carlo methods is the ability to construct and employ arbitrarily complex particle representations, without incurring the exponential run-time scaling inherent to the sectional approach. The additional particle dimensions not afforded to traditional sectional methods can then be integrated into the process description.

One of the earliest examples of Monte Carlo methods being applied to particulate processes, such as coalescence, is that by Spielman and Levenspiel [161]. The formalisation of a continuous time Markov Chain Monte Carlo simulation algorithm was later carried out by Gillespie [59] for stochastic coagulation processes within a cloud. Peborgh Gooch and Hounslow [166] appear to have been the first to specifically apply MC methods, in the now conventional form, to the modelling of crystallisation, which shares many features with granulation processes. It appears that the first application of stochastic particle techniques specifically to granulation modelling was carried out by Gantt and Gatzke [55]. The authors of this study used a 3D PBM with a constant number Monte Carlo method to model a granulation process in a high-shear batch mixer. That is to say, the number of computational particles remained constant over the course of the simulation. Since then, MC-PBMs have been successfully applied to the simulation of high-shear batch granulation [17, 19–24, 76, 95, 96, 126]; nano-particle synthesis [72, 116]; combustion engine modelling [26, 123]; soot formation [5, 27]; aerosol wet scavenging [179]; metallic nano-particle formation [16] and more general coagulation processes [171]. To the best knowledge of the author, this thesis presents the first use of a stochastic PBM for twin-screw granulation modelling.

MC-PBM ensembles are evolved in time through Markov jump events. The events may act on and transform one or more particles at a time. The waiting time between successive jump events follows a Poisson distribution. These jump events represent the various particle mechanisms such as coagulation, breakage etc, that form the process description. These processes can be numerically challenging to perform using the DSA, since highly unbalanced coagulation-breakage rates can lead to the undesired depletion or accumulation of computational particles [95]. The importance of maintaining a constant number of computational particles within MC-PBM, or enforcing a lower bound on this value in order to control variance in the solution, was demonstrated by Kolodko and Sabelfeld [81]. Constant number DSMC is achieved through the expansion or contraction of the sample volume and replication or deletion of computational particles. Doubling methods (otherwise known as step-wise constant number Monte Carlo) were first demonstrated in the context of DSMC by Maisels et al. [107], to enforce a lower bound on the number of particles. Although these techniques can mitigate some sources of variance, the DSA method still requires a large number of computational particles and repetitions of the simulation in order achieve an accurate sampling of the solution, both of which come at the cost of increased CPU time and memory [177].

The stochastic weighted particle method (also called the Stochastic Weighted Algorithm (SWA)), originally proposed by Rjasanow and Wagner [142], has been developed to overcome a number of the limitations of the DSA. In the SWA, each computational particle has an associated statistical weight w. Using a number based weighting scheme with the SWA, the number of 'real' particles represented by each computational particle x is proportional to w, and the ensemble is represented as a collection of coordinates (x, w). SWA analogues of various particle processes such as coagulation [33, 44, 134, 178] and breakage [96, 182] have been developed. Using the SWA, these processes can be formulated such that they conserve the number of computational particles, through the transformation of statistical weights. Examples of constant number SWA processes are the coagulation jump processes presented by Patterson et al. [135] and the breakage processes of Lee et al. [96]. Zhao and co-workers [178, 180, 181] have also presented a SWA scheme to dynamically control the number of computational particles that fall within predefined volume intervals. This is done through the periodic modification of the number of computational particles and statistical weights within each volume interval. This "shift" action acts to maintain statistical precision across the full range of the distribution. The mathematical

formulation of a SWA framework for twin-screw granulation is discussed in Chapters 4 and 7.

Chapter 3

A new model for twin-screw granulation

This thesis is concerned with the development of a population balance model for twin-screw granulation. In this chapter, the fundamental twin-screw population balance equation that forms the basis of the rest of the work in this thesis is presented. Each of the particle mechanisms within the model is described in detail, including nucleation, coagulation, compaction, liquid penetration, fragmentation, inception and transport.

3.1 Background

It is desired to construct a stochastic population balance model to describe the twin-screw granulation process. To do so, this work builds upon the existing high-shear stochastic PBM, introduced by Braumann et al. [19] and further developed by Lee et al. [95]. The model of Braumann et al. [19] used a five-dimensional particle representation in which each particle was considered to be composed of solid original (primary powder volume), reacted solid (solidified binder volume), internal liquid volume, external liquid volume and porosity. Within the batch model, particle compositions were evolved in time according to a number of physical and semi-empirical mechanisms. These particle mechanisms were: liquid inception; binary particle collisions, which could lead to coagulation, rebound and compaction; binary breakage; liquid penetration, into the pore volume; and reaction (solidification) of binder into reacted solid. This model was successfully employed to simulate the evolution of granular material in a high-shear ploughshare mixer with atomised liquid inception.

The model of Braumann et al. [19] was extended by Lee et al. [95] and further developed in [94] to include spatial inhomegenities. In this way, a batch system could be represented as a number of connected compartments. The rates of each mechanism could then be set individually for each compartment, reflecting localised agitation rates, liquid addition rates etc. The addition of a transport mechanism permitted particles to move between compartments according to the predefined connections and residence times. The resulting model framework was demonstrated to better capture experimental product particle size distributions than the single compartment case. However, it is worth noting that a direct comparison of the predictive abilities of the two models was not possible, since the number of adjustable parameters was greater in the case of the multi-compartment simulation.

The extension of the compartmental model of Lee et al. [95] to twin-screw granulation requires the development and addition of several new mechanisms to reflect the disparities between TSG and high-shear batch granulation. Most important, is the inclusion of an immersion nucleation mechanism to capture the formation of nascent agglomerates in the droplet zone of the TSG. Furthermore, the transition from a batch to a continuous PBM necessitates the need for continuous particle inflow and outflow from the compartmental network . In addition to these mechanism additions, it is also necessary to revisit the existing mechanisms within the

model of Braumann et al. [19] and assess their applicability to TSG, based on existing experimental twin-screw studies.

The remainder of the chapter is dedicated to the presentation of the new population balance equation for twin-screw granulation. Following the presentation of the PBE is a description of each of the new and existing particle mechanisms that take their place within the PBE. Where adaptions to the existing mechanisms of Braumann et al. [19] and Lee et al. [95] are made, this is noted within the text and the new mechanisms formulations (and their justifications) are given in full.

3.2 The model

3.2.1 Particle type-space

Within the twin-screw model the particle type-space $\mathbb{X}$ is employed to describe the physical state of a particle. Within this type-space, particles are represented by a vector with the form $x = (s_{\mathrm{o}}, l_{\mathrm{e}}, l_{\mathrm{i}}, p), x \in \mathbb{X}$, where: s_{o} is the original solid volume , l_{e} is the external liquid volume , l_{i} is the internal liquid volume and p is the pore volume, as illustrated in Figure 2.6. Internal liquid only exists within the pore volume and the remaining pore volume is occupied with gas (i.e. $l_{\mathrm{i}} \leq p$). This type-space is capable of representing any of the phases present in a placebo granulation system, namely: primary particles, granules and free liquid droplets.

It should be noted that the type-space in this thesis is a sub-space of the five-dimensional type-space employed within the high-shear batch models of Braumann et al. [19] and Lee et al. [95] (described in Section 3.1). The decision was made to drop the additional reacted solid volume component (s_r) from the type-space, firstly due to the low residence times present in TSG, relative to high-shear batch systems. TSG residence times are generally under 10s, whereas the duration of the high-shear batch experiments considered by Braumann et al. [19] and Lee et al. [94, 95] were on the order of several minutes. The slow rate of this process (as estimated by Lee et al. [94]) suggests that it is of little importance to TSG systems, at least for α-lactose monohydrate-water formulations that are considered within this thesis. The second reason for the removal of the reacted solid component from the type-space was the relatively poor knowledge of the mechanism through which this phase is generated, and the lack of experimental evidence of it within the twin-screw literature. When comparing the models presented in this thesis with that of Braumann et al. [19] and Lee et al. [95] it is

convenient to consider the particles in the twin-screw model to have a composition with $s_r(x) = 0 \; \forall \, x \in \mathbb{X}$ and the reaction rate constant k_{reac} of Braumann et al. [19] to be zero at all times.

Using this particle description, the derived particle properties follow the definitions given in Table 3.1. Particles are assumed to be spherical for the purposes

Table 3.1 Summary of derived particle properties. ρ_{s} and ρ_{l} are the solid and liquid densities, respectively.

Property	Nomenclature	Expression	Unit
Volume	$v(x)$	$s_{\text{o}}(x) + l_{\text{e}}(x) + p(x)$	m^3
Diameter	$d(x)$	$(6v(x)/\pi)^{1/3}$	m
Mass	$m(x)$	$\rho_{\text{s}} s_{\text{o}}(x) + \rho_{\text{l}}(l_{\text{i}}(x) + l_{\text{e}}(x))$	kg
Porosity	$\varepsilon(x)$	$p(x)/v(x)$	-
External surface area	$a_{\text{surf}}(x)$	$\pi^{1/3}(6v(x))^{2/3}$	m^2

of computing particle surface areas and diameters, however, all non-liquid particles are assumed to have surface asperities with characteristic length scale h_{a}. These asperities, along with other properties, control the likelihood of successful coalescence between two particles, described further in Section 3.2.3.

Building on the work of Lee et al. [95], the granulator is represented by a series of connected, well-mixed compartments, in which particles x take position. The set of all valid compartments is denoted $\mathbb{L} = \{1, 2, 3, ..., z_{\text{max}}\}$. Particles in compartment $z \in \mathbb{L}$ are only permitted to interact with those particles in the same compartment and particles are permitted to move between compartment z to $z+1$, simulating the flow of material along the screw barrel. The rates associated with the various TSG mechanisms may very between compartments to represent changes in the screw geometry and localisation of some processes such as liquid and solid particle addition. For simplicity, it is enforced that all compartments are of equal volume. This assumption is applied from this point, up to and including Chapter 6 of this thesis. It is revisited in Chapter 7, where more complex and variable screw geometries are considered.

3.2.2 The population balance equation

In order to formulate the full multi-dimensional population balance model for the twin-screw granulation process, it is useful to first examine a simplified PBE. Consider a one-dimensional type-space in which only the particle size is tracked,

where $x = s_o$. Note that, in this reduced type-space, it is not possible to include all the particle processes of the full multi-dimensional twin-screw PBM, and so this example will only consider those for which a single dimensional analogue exists. For each $z \in \mathbb{L}$, the single dimensional PBE may be formulated in terms of the number concentration of particles of size x, denoted $c(t,z,x)$, as

$$\begin{aligned}\frac{\mathrm{d}}{\mathrm{d}t}c(t,z,x) = I(z,x) \\ &+ \frac{1}{2}\int_0^x K_{\text{coag}}(x-x_j,x_j)c(t,z,x-x_j)c(t,z,x_j)\mathrm{d}x_j \\ &- \int_0^\infty K_{\text{coag}}(x,x_j)c(t,z,x)c(t,z,x_j)\mathrm{d}x_j \\ &- g_{\text{break}}(z,x)c(t,z,x) + 2\int_x^\infty g_{\text{break}}(z,x_j)B(x_j,x)c(t,z,x_j)\mathrm{d}x_j \\ &+ \frac{1}{\tau(z-1)}c(t,z-1,x) - \frac{1}{\tau(z)}c(t,z,x).\end{aligned} \tag{3.1}$$

Each term on the RHS of Equation (3.1) represents a particle mechanism in the reduced order model. The first term on the RHS of Equation (3.1) represent a particle inception process. The second term represents the creation of particles of size x from the coalescence of smaller particles according to the coagulation kernel K_{coag}. The third term accounts for the depletion of particles of size x as they coalesce with other particles to form larger particles. The fourth term in Equation (3.1) represents the depletion of particles of size x as they break into smaller particles. The fifth term represents the creation of particles of size x through the breakage of larger particles, according to breakage frequency function g_{break} and fragment probability distribution B. The final two terms of Equation (3.1) capture the particle inflow and outflow processes on compartment z, respectively.

In order to transition from the reduced order model of Equation (3.1) to the full multi-dimensional model, it is necessary to consider not number concentration $c(t,z,x)$ but rather concentration measures of the form $\lambda(z,t,\mathrm{d}x)$. In this way a more general type-space $\mathbb{X}$ can be employed, which can be multi-dimensional and either continuous or discrete in nature. Since this thesis is concerned with simulating the TSG model using a stochastic particle method, the population balance equation is constructed in weak form. That is to say, the new concentration measure $\lambda(z,t,\mathrm{d}x)$ is integrated against some suitable test function $\varphi(z,x)$, which is continuous with compact support. Let

1. $\lambda(z,t,\mathrm{d}x)$ be a concentration measure on $\mathbb{X}$ at time t in compartment z, or more simply, a concentration measure on the interval $x+\mathrm{d}x$ in compartment z at time, t.
2. Addition and subtraction on $\mathbb{X}$ correspond to particle coagulation and breakage, respectively.
3. $\varphi(z,x) : \mathbb{X} \mapsto \mathbb{R}$ be a suitable test function which is smooth with compact support,
4. $\mathbb{X}_{\text{nuc}} \subset \mathbb{X}$ be the set of all partially formed granular nuclei.
5. $\mathbb{X}_{\text{incept}} \subset \mathbb{X}$ be the set of all possible inception particle forms.

The full twin-screw PBE may then be formulated $\forall z \in \mathbb{L}$ as

$$\begin{aligned}
\frac{\mathrm{d}}{\mathrm{d}t}\int_{x\in\mathbb{X}} \varphi(z,x)\lambda(z,t,\mathrm{d}x) = \qquad & (3.2)\\
&\int_{x\in\mathbb{X}_{\text{incept}}} \varphi(z,x) I_{\text{solid}}(z,t,\mathrm{d}x)\\
&+\frac{1}{2}\int_{x,y,\xi,\zeta\in\mathbb{X}} [\varphi(z,\xi+\zeta)-\varphi(z,x)-\varphi(z,y)] K_{\text{coag}}(z,\xi,\zeta)\\
&\qquad \mathbb{P}(D_t x=\mathrm{d}\xi)\mathbb{P}(D_t y=\mathrm{d}\zeta)\\
&\qquad \lambda(z,t,\mathrm{d}x)\lambda(z,t,\mathrm{d}y)\\
&+\frac{1}{2}\int_{x,y,\xi\in\mathbb{X}} [\varphi(z,\xi)-\varphi(z,\xi-y)-\varphi(z,x)] F(z,\xi,\mathrm{d}y)\\
&\qquad \mathbb{P}(D_t x=\mathrm{d}\xi)\lambda(z,t,\mathrm{d}x)\\
&+\int_{x,\xi\in\mathbb{X}} \varphi(z,\xi)\frac{1}{\tau(z-1)}\mathbb{P}(D_t x=\mathrm{d}\xi)\lambda(z-1,t,\mathrm{d}x)\\
&-\int_{x,\xi\in\mathbb{X}} \varphi(z,\xi)\frac{1}{\tau(z)}\mathbb{P}(D_t x=\mathrm{d}\xi)\lambda(z,t,\mathrm{d}x)\\
&+\int_{x\in\mathbb{X}} \varphi(z,x) I_{\text{drop}}(z,t,\mathrm{d}x)\\
&+\int_{x,\xi\in\mathbb{X}_{\text{nuc}},y,\zeta\in\mathbb{X}\setminus\mathbb{X}_{\text{nuc}}} [\varphi(z,T_{\text{nuc}}(\xi,\zeta))-\varphi(z,x)-\varphi(z,y)]\\
&\qquad K_{\text{nuc}}(z,\xi,\zeta)\mathbb{P}(D_t x=\mathrm{d}\xi)\mathbb{P}(D_t y=\mathrm{d}\zeta)\\
&\qquad \lambda(z,t,\mathrm{d}x)\lambda(z,t,\mathrm{d}y).
\end{aligned}$$

In this form, each integral on the RHS of Equation (3.2) represents an aggregate particle processes within the model. The $\varphi(\cdot)$ component of each integrand represents the particle transformation of the associated mechanism. The remainder of the integrand defines the rate at which this event occurs. As in Equation (3.1), the first term in Equation (3.2) represents the inception of solid particle into the system (simulating the inflow of feed powder i.e. primary particles). The second term in (3.2) combines the birth and death terms related to coagulation processes (terms two and three in Equation (3.1)). The third term of Equation (3.2) represents the birth and death terms associated with particle fragmentation, combining the fourth and firth terms of (3.1). The fourth and fifth terms of Equation (3.2) capture the inter-compartment particle transport terms features in the last two terms of (3.1). The second last term in Equation (3.2) represents the inception of liquid droplets into the liquid addition zone of the twin-screw. Finally, the last term in Equation (3.2) concerns the growth of nuclei within the twin-screw device. The physical model and type-space transformations associated with each of these particle processes will be explained, in detail, in Section 3.2.3.

One notable term that appears in Equation (3.2) is the deferment operator D_t. This operator $D_t : (\mathbb{L}, \mathbb{X}) \mapsto \mathbb{X}$ represents the continuous particle process (liquid penetration) of the twin-screw model. Deferred processes are processes which are both continuous (as opposed to discrete events such as collisions, fragmentation) and are, in general, linear in nature. Here, the term 'linear' should be interpreted as only changing the state of the particle that they act on, and thus the rest of the system is not directly affected by their application. The deferment of these processes is motivated by the significant computational cost of approximating their continuous nature as a discrete process with a large rate. This concept was formalised as the Linear Process Deferment Algorithm (LPDA) presented by Patterson et al. [133]. In the LPDA, the deferment is implemented by tagging particles with their current time t_p. Whenever a non-deferred process is to be applied to a particle or group of particles, D_t is applied to each in particle in sequence to evolve them (numerically integrate them) from their current time t_p to the true system time t. A discussion of the precise implementation of the LPDA is left to Chapter 4. In terms of the nomenclature of Equation (3.2), for any particle x and compartment z, $D_t(z,x)$ is distributed as the value at time t of the Markov chain defined by the undeferred jump events and their associated rates. In this way, $\mathbb{P}(D_t(z,x) = \mathrm{d}\xi)$ defines that probability that particle $D_t(z,x)$ will lie within the type-space $[\xi, \xi + \mathrm{d}\xi]$.

Table 3.2 Comparison with existing stochastic high-shear granulation models.

	Braumann et al. [19], Lee et al. [95]	This work
Particle description	$(s_\mathrm{o}, s_\mathrm{r}, l_\mathrm{e}, l_\mathrm{i}, p)$	$(s_\mathrm{o}, l_\mathrm{e}, l_\mathrm{i}, p)$
Mechanisms	collision (coagulation+compaction) fragmentation liquid inception transport reaction	collision (coagulation+compaction) fragmentation liquid inception transport nucleation particle inception

3.2.3 Particle processes

The subject of this section is the description of the physical models that characterise the various terms in Equation (3.2). A comparison between the mechanism set of Braumann et al. [19], Lee et al. [95] and that used in this work is provided in Table 3.2.

Liquid addition

As in Lee et al. [95], liquid addition involves the addition of a droplet particle into one of the compartments. In this work, this is always the compartment with $z = 1$, representing the start of the variation zone of the granulator. Droplets are assumed to be mono-disperse, such that incepted droplet particles take the form

$$x_\mathrm{drop} = (0, v_\mathrm{drop}, 0, 0), \tag{3.3}$$

where v_drop is the droplet volume. Droplets are presumed to be spherical such that

$$v_\mathrm{drop} = \pi d_\mathrm{drop}^3/6, \tag{3.4}$$

where d_drop is the droplet diameter. Throughout this thesis it is assumed that d_drop is equal to the the diameter of liquid inception port of the twin-screw device, denoted d_nozzle.

This process occurs with rate

$$I_\mathrm{drop}(z, t, \mathrm{d}x) = \frac{\dot{V}_l(z)}{V_\mathrm{real}(z) v_\mathrm{drop}} \delta_{x_\mathrm{drop}}(x)\mathrm{d}x, \tag{3.5}$$

where $V_\mathrm{real}(z)$ is physical volume of the compartment z, $\dot{V}_l(z)$ is the liquid flow-rate delivered to compartment z, v_drop is the volume of the droplets being incepted

Table 3.3 Nucleation-related definitions.

Term	Definition
nucleus	A particle formed from the combination of liquid droplet and some amount of solid particles
partially formed nucleus	Any particle which was formally incepted into the granulator as a liquid droplet that may or may not have acquired some degree of solid mass and pore volume through 'nucleation' events (defined in Equation 3.7). Partially formed nuclei have a non-zero volume of external liquid, thus permitting the further addition of solid mass to its body.
fully formed nucleus	Any particle that was formally a partially formed nucleus, which has, through the nucleation process, gained sufficient mass to reduce its external liquid volume to zero.

and $\delta_{x_{\text{drop}}}$ is to be interpreted as the Dirac delta function, centred on x_{drop}. $\dot{V}_l$ is given by the LSR and the liquid density ρ_{l} as

$$\dot{V}_l(z) = \begin{cases} \frac{(\text{LSR})\dot{m}_{\text{feed}}}{\rho_{\text{l}}}, & \text{if } z = 1, \\ 0 & \text{otherwise,} \end{cases} \tag{3.6}$$

where $\dot{m}_{\text{feed}}$ is the operating mass feed rate to the device.

Nucleation

Nucleation is the process by which a droplet particle or partially formed nucleus acquires mass from the particle bed. Throughout the remainder of this thesis, the nucleation-related definitions given in Table 3.3 will be used. The set of droplets and partially formed nuclei is denoted $\mathbb{X}_{\text{nuc}} \subset \mathbb{X}$. In this chapter, an interpretation of the immersion nucleation mechanism (see Chapter 2, Section 2.5.1) is adapted to the type-space of the current model. In this way, a single droplet will produce a single nucleus and no re-wetting of granular material in the droplet zone is considered. As a particle is added to the partially formed nucleus, this results in the drying of the nucleus surface (internalisation of liquid). The degree of drying is assumed to be dependent on the state of the particle being added.

A nucleation event (i.e. particle addition to a droplet or partially formed nuclei) takes the form:

$$x, x_{\text{nuc}} \mapsto T_{\text{nuc}}(x, x_{\text{nuc}}), \tag{3.7}$$

where $x \in \mathbb{X} \setminus \mathbb{X}_{\text{nuc}}$, $x_{\text{nuc}} \in \mathbb{X}_{\text{nuc}}$ and T_{nuc} is the nucleation transform (a vector valued function).

T_{nuc} is characterised by the following type-space transformations

$$s_{\text{o}}(x_{\text{nuc}}) \leftarrow s_{\text{o}}(x_{\text{nuc}}) + s_{\text{o}}(x), \tag{3.8}$$

$$l_{\text{e}}(x_{\text{nuc}}) \leftarrow l_{\text{e}}(x_{\text{nuc}}) - \min([\phi_{\max} - \phi(x)]s_{\text{o}}(x), l_{\text{e}}(x_{\text{nuc}})), \tag{3.9}$$

$$l_{\text{i}}(x_{\text{nuc}}) \leftarrow l_{\text{i}}(x_{\text{nuc}}) + l_{\text{i}}(x) + l_{\text{e}}(x) + \min([\phi_{\max} - \phi(x)]s_{\text{o}}(x), l_{\text{e}}(x_{\text{nuc}})), \tag{3.10}$$

$$p(x_{\text{nuc}}) = l_{\text{i}}(x)/s^*. \tag{3.11}$$

Here, $\mathbb{1}_{\mathcal{A}}$ is to be interpreted as the indicator function on set $\mathcal{A}$ and $\phi(x)$ is the liquid saturation level of the particle to be added, given as:

$$\phi(x) = \frac{l_{\text{i}}(x) + l_{\text{e}}(x)}{s_{\text{o}}(x)}. \tag{3.12}$$

$\phi_{\max}$ is the maximum level of liquid saturation in the nuclei. To quantify this value, a similar approach to that used by Barrasso and Ramachandran [12] is employed. This approach is consistent with the nucleation mechanism described by Iveson et al. [75], where nuclei are formed by way of droplet penetration into a porous bed. This is captured by the relation:

$$\phi_{\max} = \frac{(1 - \varepsilon_{\text{bed}})s^*}{\varepsilon_{\text{bed}}}, \tag{3.13}$$

where ε_{bed} is the bed packing fraction and s^* is the maximum internal pore liquid saturation level of the nuclei.

The addition of particles to the nucleus through the nucleation processes ceases when $l_{\text{e}}(T_{\text{nuc}}(x, x_{\text{nuc}})) = 0$ (i.e. at this point $T_{\text{nuc}}(x, x_{\text{nuc}}) \notin \mathbb{X}_{\text{nuc}}$). It is noted that the particle transform in Equation (3.9) allows the addition of over-saturated particles to the nucleus. This permits the generation of additional nuclei surface liquid and, hence, allows for further particle addition (growth) to (of) the nucleus.

The rate of process (3.7) is dictated by the nucleation kernel K_{nuc}. It is assumed that the probability that a particle will join a partially formed nucleus is proportional to the volume of the particle only. This is justified for immersion

nucleation, since the volume of x_{nuc} will generally far exceed that of other non-nuclei particles in the droplet zone. Additionally, it is postulated that there is a maximum particle size that can be integrated into the nucleus. The size limit for integration $v_{\text{nuc}}^{\max} = v_{\text{drop}}$ is used in this work. For $x \in \mathbb{X} \setminus \mathbb{X}_{\text{nuc}}$, $x_{\text{nuc}} \in \mathbb{X}_{\text{nuc}}$ the nucleation kernel is formulated as

$$K_{\text{nuc}}(z,x,x_{\text{nuc}},t) = \begin{cases} k_{\text{nuc}}(z)v(x) & \text{if } v(x) < v_{\text{drop}}, \\ 0 & \text{otherwise,} \end{cases} \tag{3.14}$$

where $k_{\text{nuc}}(z)$ is the nucleation rate constant that controls the rate of particle addition to the nuclei.

This model is to be calibrated against experimental data sets that employ common placebo formulations. These typically consist of α-lactose monohydrate as the excipient and a distilled water binder. As noted by Hapgood et al. [65], in such formulations, the droplet penetration time can likely be considered to be negligible. Hence, it is assumed that particle addition to the nuclei is instantaneous (i.e. $k_{\text{nuc}}(z) \to \infty \, \forall z \in \mathbb{L}$). As such, directly after a liquid addition event has occurred, event (3.7) occurs repeatedly (i.e there are no other events occurring between them) until the condition $l_{\text{e}}(T_{\text{nuc}}(x,x_{\text{nuc}})) = 0$ is satisfied. In this way, there is at most one droplet or partially formed nucleus particle (members of $\mathbb{X}_{\text{nuc}}$) present in the droplet zone ($z = 1$) at any given time. Furthermore, members of $\mathbb{X}_{\text{nuc}}$ do not exist in any compartment other than $z = 1$.

Coagulation and compaction

Model particles may undergo binary collisions which may lead to coagulation and compaction of the collision pair. This is characterised by the jumps

$$\begin{aligned} \text{Coalescence successful: } & (x_i),(x_j) \to (T_{\text{comp}}(T_{\text{coag}}(x_i,x_j))), \\ \text{Coalescence unsuccessful: } & (x_i),(x_j) \to (T_{\text{comp}}(x_i)),(T_{\text{comp}}(x_j)), \end{aligned}$$

where T_{coag} and T_{comp} are the coagulation and compaction transformations, respectively.

Coagulation

The rate of collision between particles x_i and x_j is modelled using the size

independent collision kernel:

$$K_{\text{col}}(z, x_i, x_j) = n_{\text{screw}} k_{\text{col}}(z), \tag{3.15}$$

where n_{screw} is the screw speed and k_{col} is the collision rate constant.

As in [22, 95], the success of failure of a collision in coalescing the collision pair is governed by the Stokes criterion, formalised by Ennis et al. [50]. This criterion states that, given a collision particle pair x_i, x_j, coalescence only occurs if

$$\text{St}_{\text{v}}(x_i, x_j) \leq \text{St}^*_{\text{v}}(x_i, x_j), \tag{3.16}$$

where St_{v} is the viscous Stokes number and St^*_{v} is the critical stokes number.

The viscous Stokes number is defined as [50]

$$\text{St}_{\text{v}}(x_i, x_j) = \frac{\tilde{m}(x_i, x_j) U_{\text{col}}}{3\pi\mu\tilde{R}(x_i, x_j)^2}, \tag{3.17}$$

and $\tilde{m}$ is the mean harmonic mass of the collision pair, U_{col} is the particle collision velocity, μ is the binder viscosity and $\tilde{R}$ is the harmonic mean radius of the collision pair.

The critical Stokes number is defined as [22]

$$\text{St}^*_{\text{v}}(x_i, x_j) = \left(1 + \frac{1}{e_{\text{coag}}}\right) \ln\left(\frac{\bar{h}_{\text{binder}}(x_i, x_j)}{h_{\text{a}}}\right), \tag{3.18}$$

where e_{coag} is the coefficient of restitution of the granule material, $\bar{h}_{\text{l}}$ is arithmetic average binder thickness of the collision pair and h_a is the height of surface asperities. As in [22], individual particle binder levels h_{l} are computed as

$$h_{\text{l}}(x) = \frac{1}{2}\sqrt[3]{\frac{6}{\pi}}\left[\sqrt[3]{v(x)} - \sqrt[3]{v(x) - l_{\text{e}}(x)}\right] \tag{3.19}$$

Given this criterion, the full coagulation kernel K_{coag} ,which features the PBE (Equation (3.2)), can be formulated as

$$K_{\text{coag}}(z, x_i, x_j) = K_{\text{col}}(z, x_i, x_j) \mathbb{1}_{\{x_i, x_j | \text{St}_{\text{v}}(x_i, x_j) \leq \text{St}^*_{\text{v}}(x_i, x_j)\}}(x_i, x_j). \tag{3.20}$$

Following the approach of Goodson et al. [62], if a coagulation event is successful, then a fraction of the external liquid l_{e} from the particles involved in the collision

becomes internal liquid l_i in the newly formed particle (see Figure 3.1). The pore

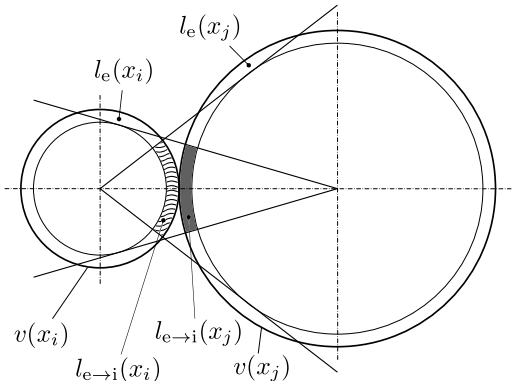

Fig. 3.1 Internalisation of liquid and pore creation during coalescence. Adapted from [19].

volume of the newly formed particle is further modified to describe successful collisions. This process is encoded within the coagulation transformation T_coag, whose coordinate functions are defined as [19, 22]

$$T_\mathrm{coag}(x_i,x_j)_{s_\mathrm{o}} = s_\mathrm{o}(x_i) + s_\mathrm{o}(x_j) \tag{3.21}$$

$$T_\mathrm{coag}(x_i,x_j)_{l_\mathrm{e}} = l_\mathrm{e}(x_i) + l_\mathrm{e}(x_j) - l_{\mathrm{e}\to\mathrm{i}}(x_i,x_j) \tag{3.22}$$

$$T_\mathrm{coag}(x_i,x_j)_{l_\mathrm{i}} = l_\mathrm{i}(x_i) + l_\mathrm{i}(x_j) + l_{\mathrm{e}\to\mathrm{i}}(x_i,x_j) \tag{3.23}$$

$$\begin{aligned} T_\mathrm{coag}(x_i,x_j)_p = &\frac{a^+_\mathrm{surf}(x_i,x_j)^{\frac{3}{2}}}{6\pi^{1/2}} \\ &- \left[s_\mathrm{o}(x_i) + s_\mathrm{o}(x_j) - l_\mathrm{e}(x_i) - l_\mathrm{e}(x_j) + l_{\mathrm{e}\to\mathrm{i}}(x_i,x_j)\right], \end{aligned} \tag{3.24}$$

where

$$\begin{aligned} a^+_\mathrm{surf}(x_i,x_j) = &(1-e_\mathrm{coag})\left[a_\mathrm{surf}(x_i)^{3/2} + a_\mathrm{surf}(x_j)^{3/2}\right]^{2/3} \\ &+ e_\mathrm{coag}\left[a_\mathrm{surf}(x_i) + a_\mathrm{surf}(x_j)\right], \end{aligned} \tag{3.25}$$

and $l_{\mathrm{e}\to\mathrm{i}}(x_i,x_j)$ represents the amount of surface liquid that is internalised due to the contact area between the colliding particle pair. This is computed as [19]

$$l_{\mathrm{e}\to\mathrm{i}}(x_i,x_j) = \left\{ l_{\mathrm{e}}(x_i) l_{\mathrm{e}}(x_j) \left[1 - \sqrt{1 - \left(\frac{\sqrt[3]{v(x_i)} - l_{\mathrm{e}}(x_i)}{\sqrt[3]{v(x_i)} + \sqrt[3]{v(x_j)}} \right)^2} \right] \right. \\ \left. \times \left[1 - \sqrt{1 - \left(\frac{\sqrt[3]{v(x_j)} - l_{\mathrm{e}}(x_j)}{\sqrt[3]{v(x_i)} + \sqrt[3]{v(x_j)}} \right)^2} \right] \right\}^{1/2}. \tag{3.26}$$

Compaction

Each particle collision leads to the compaction of the particles involved. This is modelled as a porosity reduction (adapted from [19]), described by:

$$\Delta\varepsilon(x) = \begin{cases} k_{\mathrm{comp}}(z)[\varepsilon(x) - \varepsilon_{\mathrm{min}}], & \text{if } \varepsilon(x) \geq \varepsilon_{\mathrm{min}}, \\ 0, & \text{otherwise}, \end{cases} \tag{3.27}$$

where k_{comp} is the compaction rate constant and $\varepsilon_{\mathrm{min}}$ is the minimum porosity permitted.

Several experimental studies [38, 47, 152, 167, 168] have concluded that internal liquid is squeezed to the surface of nuclei and nuclei fragments in areas of high compaction such as kneading blocks. This newly surfaced liquid then permits the layering of dry primary material onto the surface of the compacted particles. To describe the movement of liquid during this squeezing process, some internal liquid is moved to external liquid.

Previous works by Braumann et al. [19], Gantt and Gatzke [55] formulated the compaction process such that liquid was only drawn to the surface when the process resulted in a particle state with $p < l_{\mathrm{i}}$. Although this does seem like a sensible choice, preliminary twin-screw simulations showed that the resulting granules had a very high degree of liquid content and that growth was limited due to lack of external liquid on the particles. The treatment of this process by Braumann et al. [19], Gantt and Gatzke [55] inherently assumes that the pore volume of the particle is uniformly reduced upon compaction. It would seem more likely that the pore volume of the regions close to the particle surface are reduced to a higher degree than those regions in the interior. It follows that it may be possible for these external pore regions to become saturated in liquid, thereby

releasing some liquid to the surface upon compaction. Again, this a very simple model of this grey box process that would need to be validated experimentally. The observations made in preliminary simulations may also be attributed to a missing mechanism for liquid penetration in the reverse direction. Such a phenomenon could arise from capillary-based driving forces, created through the addition of dry material to the surface of wet agglomerates, similar to that described by Schaafsma et al. [148]. The development of such a mechanism is left for future studies. Here a simplistic extension of the compaction of Braumann et al. [19] is used. In this adapted process, the amount of liquid transferred in a compaction event $l_{i\to e}$ is proportional to the relative change in pore volume, as described by the following relation:

$$l_{i\to e} = \Delta p_{\text{comp}} \left(\frac{l_{i,o}}{p_o} \right), \tag{3.28}$$

where $l_{i,o}$ and p_o are the internal liquid and pore volumes, respectively, prior to compaction and Δp_{comp} is the change in pore volume associated with a compaction event. Consistency between (3.27), (3.28) and the derived properties in Table 3.1 requires:

$$\Delta p_{\text{comp}} = p_o - \frac{\varepsilon_1 (s_{\text{o}} + l_{e,o} + l_{i,o})}{1 - \varepsilon_1 \left(1 - \frac{l_{i,o}}{p_o}\right)}. \tag{3.29}$$

Here, $l_{e,o}$ is the external liquid volume prior to compaction and ε_1 is the post compaction porosity.

Fragmentation

As in Braumann et al. [22], particles may undergo binary breakage, described by

$$T_{\text{break}}(x) \to (y), (x-y), \tag{3.30}$$

where T_{break} is the breakage operator.

This rate of this process is controlled by fragmentation kernel F of Equation (3.2), which is formulated as [96]

$$F(z,x,\mathrm{d}y) = \mathbb{1}_{\{x,y|m(y)<m(x)\}}(x,y) g_{\text{break}}(z,x) B(x,y) \mathrm{d}y, \tag{3.31}$$

where $g_{\text{break}}(z,x)$ is the breakage frequency function and $B(x,y)$ is the probability measure on the space of fragments y for each parent particle x. In this way, $B(x,y)\mathrm{d}y$ is the probability that a fragmentation product from parent particle x exists within the space $[y, y+\mathrm{d}y]$.

The choice of breakage frequency function varies significantly between high shear granulation modelling efforts, reflecting the relatively poor understanding of this particle process. Breakage kernels generally take the form of a volume-based kernel, which may have a fitted [7] or predefined exponent [87] and may also be partially dependent on the particle pore volume [22]. In preliminary model development, various power law kernels were tested and assessed through the PSD evolution of particles along the network. A volume based-kernel with direct proportionality was settled upon, due to its simplicity and the fact that it resulted in sensible PSD evolutions along the network. In Chapter 7, this selection is revisited and more complex forms are explored. Primary particles (i.e. pure solid particles) and particles with volume less than $v_{\text{parent}}^{\min}$ are considered to be unbreakable. The breakage frequency function for particle x is:

$$g_{\text{break}}(z,x) = \begin{cases} k_{\text{att}}(z) n_{\text{screw}}^2(z) v(x), & \text{if } v(x) \geq v_{\text{parent}}^{\min} \text{ and } l_{\text{e}}(x) + l_{\text{i}}(x) + p(x) \neq 0, \\ 0 & \text{otherwise,} \end{cases} \tag{3.32}$$

where k_{att} is the attrition rate constant.

As in Braumann et al. [22], the product particles of a breakage event are assumed to have the same composition are the parent particle x. The volume of the fragment particle y is defined using the random variable [22]

$$v_y(z,x,\chi_{\text{frag}}) = v_{\text{frag}}^{\min} + \chi_{\text{frag}} \left[\nu_{\max} v(x) - v_{\text{frag}}^{\min} \right], \tag{3.33}$$

where $v_{\text{frag}}^{\min}$ is the minimum fragment volume that can be produced and $\nu_{\max}$ defines the maximum fraction of the parent particle which can break off. χ_{frag} is a random measure on the interval $[0,1]$ with beta distribution [19]

$$f(\chi_{\text{frag}}) = \frac{1}{\Omega(\alpha_{\text{daughter}}, \beta_{\text{daughter}})} \chi_{\text{frag}}^{\alpha_{\text{daughter}}-1} (1-\chi_{\text{frag}})^{\beta_{\text{daughter}}-1}, \tag{3.34}$$

where

$$\Omega(\alpha_{\text{daughter}}, \beta_{\text{daughter}}) = \int_0^1 \chi_{\text{frag}}^{\alpha_{\text{daughter}}-1} (1-\chi_{\text{frag}})^{\beta_{\text{daughter}}-1} \mathrm{d}\chi_{\text{frag}}. \tag{3.35}$$

Liquid penetration

As previously mentioned, binder penetration is modelled as a continuous process within the model. The penetration process is intended to capture the flow of binder from the particle surface to the interior of the particle, driven by capillary forces. As in Braumann et al. [23], this involves the transformation of l_e to l_i at rate r_pen, controlled by the rate constant k_pen as:

$$r_\mathrm{pen}(z,x) = k_\mathrm{pen}(z)\mu_\mathrm{binder}^{-1/2} l_\mathrm{e}(x)(p(x) - l_\mathrm{i}(x)), \tag{3.36}$$

where μ_binder is the viscosity of the binder.

Each particle in the ensemble is modified between stochastic jump events according to the following set of ordinary differential equations:

$$\left.\frac{\mathrm{d}s_\mathrm{o}}{\mathrm{d}t}\right|_\mathrm{defer} = 0, \quad \left.\frac{\mathrm{d}l_\mathrm{e}}{\mathrm{d}t}\right|_\mathrm{defer} = -r_\mathrm{pen}, \quad \left.\frac{\mathrm{d}l_\mathrm{i}}{\mathrm{d}t}\right|_\mathrm{defer} = r_\mathrm{pen}, \quad \left.\frac{\mathrm{d}p}{\mathrm{d}t}\right|_\mathrm{defer} = -r_\mathrm{pen}. \tag{3.37}$$

and

$$\left.\frac{\mathrm{d}x}{\mathrm{d}t}\right|_\mathrm{defer} = \left(\left.\frac{\mathrm{d}s_\mathrm{o}}{\mathrm{d}t}\right|_\mathrm{defer}, \left.\frac{\mathrm{d}l_\mathrm{e}}{\mathrm{d}t}\right|_\mathrm{defer}, \left.\frac{\mathrm{d}l_\mathrm{i}}{\mathrm{d}t}\right|_\mathrm{defer}, \left.\frac{\mathrm{d}p}{\mathrm{d}t}\right|_\mathrm{defer} \right)^\top, \tag{3.38}$$

One can therefore define the deferment operator D_t of Equation (3.2) as

$$D_t(z,x,c_\mathrm{pp}) = x + \int_{t_p}^{t} \left.\frac{\mathrm{d}x}{\mathrm{d}t}\right|_\mathrm{defer} \mathrm{d}t, \tag{3.39}$$

where t_p is the time that particle x has been simulated to and t is the global system time.

Transport

Particle x flows out of compartment $z \in \mathbb{L}$ with rate

$$\frac{1}{\tau(z)}, \tag{3.40}$$

where $\tau(z)$ is the characteristic residence time of compartment z. Applying the assumption of equal-volume compartments, particle x in compartment z,

$z < \max \mathbb{L}$ flows into compartment $z+1$ with rate:

$$\frac{1}{\tau(z-1)}. \tag{3.41}$$

Particle Inception

Similar to liquid inception, solid particles $x \in \mathbb{X}_{\text{incept}}$ of the form

$$\left(\frac{\pi d^3}{6}, 0, 0, 0\right), \tag{3.42}$$

are incepted into the first compartment. Here, $d \in \mathbb{D}_{\text{incept}} \subset \mathbb{R}^+$ is the inception particle diameter and $\mathbb{D}_{\text{incept}}$ is the set of all particle diameters used for inception. This occurs with rate

$$I_{\text{solid}}(z, \mathrm{d}x) = \frac{\dot{m}_{\text{incept}}(z)}{V_{\text{real}}(z) \left\langle m_{\text{incept}} \right\rangle} q_{0,\mathbb{X}_{\text{incept}}}(x)\mathrm{d}x. \tag{3.43}$$

Here, $\dot{m}_{\text{incept}}(z)$ is the physical mass flow rate into compartment z, $q_{0,\mathbb{X}_{\text{incept}}}(x)$ is the inception distribution on the type-space $\mathbb{X}_{\text{incept}}$ to be sampled and $\left\langle m_{\text{incept}} \right\rangle$ is the arithmetic, number average mass of the feed particles. $\left\langle m_{\text{incept}} \right\rangle$ takes the form

$$\left\langle m_{\text{incept}} \right\rangle = \int_{\mathbb{X}_{\text{incept}}} m(x) q_{0,\mathbb{X}_{\text{incept}}}(x)\mathrm{d}x. \tag{3.44}$$

and $\dot{m}_{\text{incept}}$ is defined as

$$\dot{m}_{\text{incept}}(z) = \begin{cases} \dot{m}_{\text{feed}}, & \text{if } z = 1, \\ 0, & \text{otherwise.} \end{cases} \tag{3.45}$$

$q_{0,\mathbb{X}_{\text{incept}}}(x)$ is defined as

$$q_{0,\mathbb{X}_{\text{incept}}}(x) = \frac{q_0(d(x))}{\int_{\mathbb{D}_{\text{incept}}} q_0(d(x))\mathrm{d}d}, \tag{3.46}$$

where $q_0(d)$ is the number-based probability distribution of the inception species in inception diameter space ($\mathbb{D}_{\text{incept}}$). This is derived from the volume fraction distribution $q_3(d)$ presented in [46] for the Lactose Impalpable excipient grade

as [2]

$$q_0(d) = \frac{q_3(d(x))d(x)^{-3}}{\int_{\mathbb{D}_{\text{incept}}} q_3(d)d^{-3}\mathrm{d}d}. \tag{3.47}$$

Here, $q_3(d)\mathrm{d}d$ is the fraction of the total particle volume contained within the size range d to $d+\mathrm{d}d$

Chapter 4

Stochastic particle methods for the simulation of the twin-screw model

In this chapter, the stochastic particle framework used to simulate the twin-screw population balance model of Chapter 3 is presented. An overview of existing stochastic particle methods and their suitability to twin-screw modelling is discussed, namely the discrete simulation algorithm and stochastic weighted algorithm. The weighted population balance equation and stochastic simulation methodology is described. A stochastic particle jump is introduced for each of particle mechanism in the twin-screw model of Chapter 3 and a number of novel numerical tools are developed to reduce the variance in the simulated solutions.

4.1 Background

The twin-screw population balance equation (3.2) in the previous chapter is to be solved using the stochastic particle method. As mentioned in Chapter 2, stochastic particle methods generally take one of two forms: the direct simulation algorithm or the stochastic weighted algorithm. In both the DSA and SWA, each compartment would be described by a list of computational particles or ensemble. Each compartment is assigned a set of mechanism rate constants, which reflects the inhomogeneity in processing environment across the system. Each simulated compartment represents a sub-volume or sample volume of the physical compartment of the twin-screw device being modelled. The states of these computational particles are modified through various jump events that represent the various particle mechanisms of the model, thereby advancing the ensemble in time, simulating the dynamics of the PBE.

In DSA, each of the ensemble particle represents the same number of particles in the physical system. This is advantageous, in that it is conceptually easy to think about the various physical particle processes and their computational counterparts in the simulation. However, there are several disadvantages that prevent DSA from being used with the twin-screw model in Chapter 3. The first class of disadvantages is the difficulty in controlling the number of particles in the ensemble, due to unbalanced breakage and coalescence rates, which has already been discussed when the method was introduced in Chapter 2. The second class of issues with the DSA are more closely linked to the nature of granulation processes, and indeed, specifically those such as twin-screw systems. These derive from the fact that DSA requires a large number of computational particles to be used in order to adequately describe particle distributions in systems where species can vary in concentration by several orders of magnitude (one might typically be interested in the distribution of system mass across particle size classes). This issue is a direct consequence of fixing the relationship between computational particle number and physical particle number in the DSA. In granulation, an example would be the difference in concentration between primary particles and large agglomerate particles (which have a high impact on the mass distribution). Effective sampling of both of these phases in DSA requires the use of a high number of computational particles. Another issue, that is a direct consequence of the DSA particle representation, is that some particle mechanisms may occur very rarely but have a significant impact on the state of the system. An example in TSG would be the infrequent inception of

large droplet particles (relative to other particle processes such as collision and breakage). In the simulation of a small sample volume, such process become rare events that are poorly sampled, resulting in the simulation compartment oscillating between liquid rich and liquid poor states. This oscillatory behaviour induces a high degree of noise in the key ensemble properties of interest.

As will be demonstrated, the SWA has the potential to alleviate all of these issues, to some extent, by breaking the link between computational particle concentration and physical concentration. For this reason, it is the method of choice for the remainder of this thesis. In the SWA, for each compartment z, a set of stochastic particles is simulated in order to describe the population balance problem. The stochastic particles take the form

$$(z, x_i, w_i), \quad i = 1, \ldots, N(z,t), \tag{4.1}$$

where $x_i \in \mathbb{X}$, $w_i \in \mathbb{W} = \mathbb{R}^+$ is the statistical weight of the particle with index i and $N(z,t)$ is the number of stochastic particles in compartment z at time t.

The statistical weights offer an additional level of freedom in the construction of the simulation algorithm, whilst maintaining the property

$$\frac{1}{V_{\text{samp}}(z,t)} \sum_{i=1}^{N(z,t)} w_i \varphi(z, x_j) \xrightarrow[V_{\text{samp}(z,0)} \to \infty]{} \int_{\mathbb{X}} \varphi(z, x_j) \lambda(t, z, \mathrm{d}x). \tag{4.2}$$

Here, V_{samp} is the normalisation parameter or sample volume associated with compartment z that sets the scale of the system. Limit (4.2) may be interpreted as saying that the physical concentration of particles represented by stochastic particle $x_i(t)$ is approximately w_i / V_{samp}. In the same way, the total particle concentration in compartment z is $\sum w_i / V_{\text{samp}}$. As in Lee et al. [96], the sample volume is initialised such that

$$\frac{1}{V_{\text{samp}}(z,0)} \sum_{i=1}^{N(z,0)} w_i \approx \int_{\mathbb{X}} \lambda(0, z, \mathrm{d}x), \tag{4.3}$$

and

$$\int_{\mathbb{X}} \lambda(0, z, \mathrm{d}x) \approx \frac{N_{\text{real}}(z,0)}{V_{\text{real}}(z)}, \tag{4.4}$$

where $N_{\text{real}}(z,0)$ is the physical number of particles in physical compartment z at time $t = 0$.

The system of stochastic particles is evolved in time through a Markov jump process. This process is characterised by the possible jumps and their associated rates. Each available jump and the associated rate is a function of the state of the system at that point in time. At each t there exists a list of possible jumps which have independent, exponentially distributed waiting times. The waiting time between any two jumps Δt_{wait} is described by the distribution [59]:

$$\mathbb{P}_t(\Delta t_{\text{wait}} \geq \theta) = \exp(-R^{\text{SWA}}_{\text{total}}(t)\theta), \quad \theta \geq 0, \tag{4.5}$$

where $R^{\text{SWA}}_{\text{total}}$ is the total jump rate, which has the form

$$R^{\text{SWA}}_{\text{total}}(t) = \sum_{p\in\mathcal{P}, z\in\mathbb{L}} R^{\text{SWA}}_p(z,t). \tag{4.6}$$

Here $\mathcal{P}$ is the set of all possible jump processes and $R^{\text{SWA}}_p(z,t)$ is the total rate of jump process p in compartment z at time t.

Upon selection of the waiting time, jump process p is carried out in compartment z with probability

$$\frac{R^{\text{SWA}}_p(z,t)}{R^{\text{SWA}}_{\text{total}}(t)} \tag{4.7}$$

and the system moves forward in time. This process is continued until the stopping condition $t \geq t_{\text{stop}}$ is satisfied.

4.2 The weighted population balance equation

It is desired to formulate the SWA analogue of the twin-screw population balance equation (3.2). In order to do so, a number of the functions and measures in Equation (3.2) must be extended to accommodate the new domain $\mathbb{X}\times\mathbb{W}$. The test function $\varphi(z,x)$ is substituted with a new test function $\psi(z,x,w) = w\varphi(z,x)$ and the measure valued solution $\lambda(z,t,\mathrm{d}x)$ is replaced with a measure on the new domain, denoted $Q(z,t,\mathrm{d}x,\mathrm{d}w)$. These newly defined functions and measures satisfy [131]

$$\int_{\mathbb{X}\times\mathbb{W}} \psi(z,x,w)Q(z,t,\mathrm{d}x,\mathrm{d}w) = \int_{\mathbb{X}} \varphi(z,x)\lambda(z,t,\mathrm{d}x) \quad \forall\, t. \tag{4.8}$$

Similarly, the domain of the deferment operator D_t is extended such that new operator $\tilde{D}_t : \mathbb{X} \times \mathbb{W} \mapsto \mathbb{X} \times \mathbb{W}$. Note that the deferment operator has no effect on the particle weight. A number of the kernels (breakage, fragmentation etc.) are also replaced by their SWA analogue, which may have some dependence on w. In such cases a 'SWA' superscript has been appended to the kernel notation of Equation (3.2).

Given these extended definitions, the weighted PBM for the twin-screw model is formulated as

$$\begin{aligned}
\frac{\mathrm{d}}{\mathrm{d}t}\int_{\mathbb{X}\times\mathbb{W}}\psi(z,x,w)Q(z,t,\mathrm{d}x,\mathrm{d}w) = \qquad (4.9)\\
&\int_{\mathbb{X}_{\text{incept}}\times\mathbb{W}}\psi(z,x,w_{\text{incept}}(x))I^{\text{SWA}}_{\text{solid}}(z,t,\mathrm{d}x,\mathrm{d}u)\\
+\int_{(\mathbb{X}\times\mathbb{W})^4}&[\psi(z,\xi+\zeta,\gamma_{\text{coag}})-\psi(z,x,w)]K^{\text{SWA}}_{\text{coag}}(z,\xi,w,\zeta,u)\\
&\mathbb{P}(\tilde{D}_t(x,w)=(\mathrm{d}\xi,\mathrm{d}w))\mathbb{P}(\tilde{D}_t(y,u)=(\mathrm{d}\zeta,\mathrm{d}u))\\
&Q(z,t,\mathrm{d}x,\mathrm{d}w)Q(z,t,\mathrm{d}y,\mathrm{d}u)\\
+\int_{(\mathbb{X}\times\mathbb{W})^3}&[\psi(z,y,\gamma_{\text{frag}})-\psi(z,x)]F^{\text{SWA}}(z,\xi,w,\mathrm{d}y,\mathrm{d}u)\\
&\mathbb{P}(\tilde{D}_t(x,w)=(\mathrm{d}\xi,\mathrm{d}w))Q(z,t,\mathrm{d}x,\mathrm{d}w)\\
+\int_{(\mathbb{X}\times\mathbb{W})^2}&\psi(z-1,\xi,w)\frac{1}{\tau(z-1)}\mathbb{P}(\tilde{D}_t(x,w)=(\mathrm{d}\xi,\mathrm{d}w))\\
&Q(z-1,t,\mathrm{d}x,\mathrm{d}w)\\
-\int_{(\mathbb{X}\times\mathbb{W})^2}&\psi(z,\xi,w)\frac{1}{\tau(z)}\mathbb{P}(\tilde{D}_t(x,w)=(\mathrm{d}\xi,\mathrm{d}w))\\
&Q(z,t,\mathrm{d}x,\mathrm{d}w)\\
+\int_{\mathbb{X}\times\mathbb{W}}&\psi(z,x,w)I^{\text{SWA}}_{\text{drop}}(z,t,\mathrm{d}x,\mathrm{d}w)\\
+\int_{(\mathbb{X}_{\text{nuc}}\times\mathbb{W})^2((\mathbb{X}\setminus\mathbb{X}_{\text{nuc}})\times\mathbb{W})^2}&[\psi(z,T_{\text{nuc}}(\xi,\zeta),\gamma_{\text{nuc}})+\psi(z,\xi,w-\gamma_{\text{nuc}})\\
&+\psi(z,\zeta,u-\gamma_{\text{nuc}})-\psi(z,x,w)-\psi(z,y,u)]K^{\text{SWA}}_{\text{nuc}}(z,\xi,w,\zeta,u)\\
&\mathbb{P}(\tilde{D}_t(x,w)=(\mathrm{d}\xi,\mathrm{d}w))\mathbb{P}(\tilde{D}_t(y,u)=(\mathrm{d}\zeta,\mathrm{d}u))\\
&Q(z,t,\mathrm{d}x,\mathrm{d}w)Q(z,t,\mathrm{d}y,\mathrm{d}u)\\
&\forall z\in\mathbb{L}.
\end{aligned}$$

Each of the integrals on the RHS of Equation (4.9) represents a stochastic weighted analogue of the mechanisms of the twin-screw model. In order of appearance, these are: solid particle inception, coagulation, breakage, inflow, outflow, droplet inception and nucleation. Each of these jump processes will be described in Section 4.3.5.

4.3 Implementation considerations

4.3.1 Controlling particle number

The particle doubling and reduction methods employed by Lee et al. [96] is used to control the number of computational particles in the system. Each compartment is initialised with $N(z,0) = 0.75N_{\max}$ computational particles, where $N_{\max}$ is the maximum number of particles permitted in any compartment.

4.3.2 Ensemble doubling

For the purposes of error reduction, the minimum number of particles permitted is $(3/8)N_{\max}$. The choice of the factor $3/8$ is somewhat arbitrary, and conveniently corresponds to a lower bound on the number of computational particles which is half of that at the point of initialisation. Nevertheless, this choice has been demonstrated to give suitable performance in previous stochastic granulation studies [94–96]. This parameter is simply a way of enforcing $N(z,t)$ to be of the same order of magnitude as $N_{\max}$, thus allowing $N_{\max}$ to be used to control statistical error in the solution of the PBE. When $N(z,t) \leq (3/8)N_{\max}$ the sample volume is doubled and a single copy of each existing particle is added to compartment z, thereby preserving $\lambda(z,t,x)$. The doubling process has no effect on the statistical weight of the particles.

4.3.3 Ensemble reduction

For any compartment z, if $N(z,t) \geq N_{\max}$, then a particle (z,x,w) is uniformly selected and deleted from the ensemble. The sample volume is then updated such that

$$V_{\text{samp}}(z,t) \leftarrow V_{\text{samp}}(z,t)\frac{\left(\sum_{i=1}^{N(z,t)} w_i\right) - w_x}{\sum_{i=1}^{N(z,t)} w_i}. \tag{4.10}$$

4.3.4 Binary tree methods

The use of binary tree structures (see Figure 4.1) for the storage of ensemble information enables the rapid computation of ensemble-wide sums. An example

of such a sum is the computation of the total coagulation rate within a simulation compartment. The use of a binary tree data structure over an unordered list for the computation of coagulation rates reduces the complexity of this operation from a daunting $\mathcal{O}(N(z,t)^2)$ to a respectable $\mathcal{O}(N_{\max} \log N_{\max})$. Another advantageous property of the binary tree storage method is the ability to use the structure to efficiently perform weighted selection of ensemble particles, according to some arbitrary stored property $\phi(x_i, w_i)$. For a discussion of the particle selection procedure within binary tree structures, see [61]. In this work, each compartment z has a separate binary tree such that compartment specific jump rates can be quickly computed.

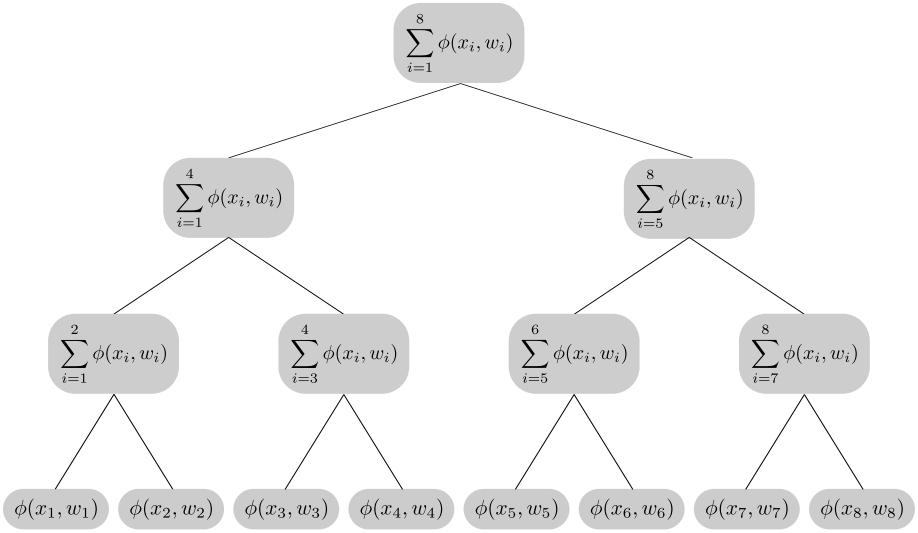

Fig. 4.1 Example of a binary tree data structure. In this case, the binary tree stores only a single 'leaf' property $\phi(x, w)$, however, this structure can be extended to a store an arbitrary number of properties.

4.3.5 Jump processes

The possible SWA jump processes and associated rates used in this work are:

Particle inception

The inception process is used to introduce pure solid particles into the system, representing the continuous addition of feed powder to the first simulated compartment of the twin-screw system. In this jump process, a new computational

particle of the form

$$(z, x, w_{\text{incept}}(x)) \tag{4.11}$$

is added to compartment z, where $x \in \mathbb{X}_{\text{incept}}$ and $w_{\text{incept}}(x)$ is some inception weight function that may have a dependence on x.

In order for the inception term of the weighted PBE (Equation 4.9) to recover that of the unweighted PBE (Equation 3.2), it is required that

$$\int_{\mathbb{X}} I_{\text{solid}}(z,t,\mathrm{d}x) = \int_{\mathbb{X}\times\mathbb{W}} w I^{\text{SWA}}_{\text{solid}}(z,t,\mathrm{d}x,\mathrm{d}w). \tag{4.12}$$

This is readily satisfied by a simple extension of the un-weighted inception rate with the form [131]

$$I^{\text{SWA}}_{\text{solid}}(z,t,\mathrm{d}x,\mathrm{d}w) = \frac{\delta_{w_{\text{incept}(x)}}(w)}{w_{\text{incept}}(x)} I_{\text{solid}}(z,t,\mathrm{d}x)\mathrm{d}w, \tag{4.13}$$

where δ_w is the Dirac delta function centred on w.

In this work, the weighted inception rate $I^{\text{SWA}}_{\text{solid}}$ is chosen to take the form

$$I^{\text{SWA}}_{\text{solid}}(z,t,\mathrm{d}x,\mathrm{d}w) := \frac{\dot{m}_{\text{incept}}(z)}{V_{\text{real}}(z)\left\langle m_{\text{incept}}\right\rangle K_{\text{w}}} \delta_{w_{\text{incept}(x)}}(w) q^{\text{SWA}}_{0,\mathbb{X}_{\text{incept}}}(x)\mathrm{d}x\,\mathrm{d}w, \tag{4.14}$$

where K_{w} is some constant and $q^{\text{SWA}}_{0,\mathbb{X}_{\text{incept}}}(x)$ is the probability distribution on the space $\mathbb{X}_{\text{incept}}$ to be sampled by the inception jump. In Equation (4.14), $\left\langle m_{\text{incept}}\right\rangle$ is again defined in terms of the physical distribution $q_{0,\mathbb{X}_{\text{incept}}}(x)$ (see Equation (3.44)). This seemingly arbitrary choice of inception function will be shown to have a number of desirable features in the remainder of this section.

One sees that, in order to satisfy the convergence criterion (4.13), given the unweighted inception rate I_{solid} (Equation (3.43)), it is required that

$$w_{\text{incept}}(x) = K_{\text{w}} \frac{q_{0,\mathbb{X}_{\text{incept}}}(x)}{q^{\text{SWA}}_{0,\mathbb{X}_{\text{incept}}}(x).} \tag{4.15}$$

Rearranging Equation (4.15) and integrating both sides over $\mathbb{X}_{\text{incept}}$, one sees that

$$K_{\text{w}} = \frac{\int_{\mathbb{X}_{\text{incept}}} w_{\text{incept}}(x) q^{\text{SWA}}_{0,\mathbb{X}_{\text{incept}}}(x)\mathrm{d}x}{\int_{\mathbb{X}_{\text{incept}}} q_{0,\mathbb{X}_{\text{incept}}}(x)\mathrm{d}x} \tag{4.16}$$

$$= \left\langle w_{\text{incept}}\right\rangle, \tag{4.17}$$

where $\langle w_{\text{incept}} \rangle$ is the number mean weight of particles selected for (solid) inception. Thus,

$$w_{\text{incept}}(x) = \langle w_{\text{incept}} \rangle \frac{q_{0,\mathbb{X}_{\text{incept}}}(x)}{q^{\text{SWA}}_{0,\mathbb{X}_{\text{incept}}}(x)} \tag{4.18}$$

and

$$I^{\text{SWA}}_{\text{solid}}(z,t,\mathrm{d}x,\mathrm{d}w) = \frac{\dot{m}_{\text{incept}}(z)}{V_{\text{real}}(z)\langle m_{\text{incept}} \rangle \langle w_{\text{incept}} \rangle} \delta_{w_{\text{incept}(x)}}(w) q^{\text{SWA}}_{0,\mathbb{X}_{\text{incept}}}(x)\mathrm{d}x\,\mathrm{d}w. \tag{4.19}$$

Note that, by asserting that the weights of incepted particles have some dependence on x, the distribution of computational particles on the space $\mathbb{X}_{\text{incept}}$ ($q^{\text{SWA}}_{0,\mathbb{X}_{\text{incept}}}(x)$) can be selected freely, whilst still reproducing some physical particle distribution $q_{0,\mathbb{X}_{\text{incept}}}(x)$. The repercussions of this feature are explored in Chapter 6. To the best of the author's knowledge, this is the first time that this weighting procedure has been formalised in the context of a stochastic population balance equation.

It is possible to alternatively express each distribution q and $\langle w_{\text{incept}} \rangle$, in terms of some other property, such as inception particle diameter $d \in \mathbb{D}_{\text{incept}}$. Since the mapping from $\mathbb{X}_{\text{incept}}$ to $\mathbb{D}_{\text{incept}}$ is one-to-one (as implied by (3.42)), then, applying the same argument as above with the new variable d yields a more useful form of the inception weighting function (from an implementation perspective), with form

$$w_{\text{incept}}(d) = \langle w_{\text{incept}} \rangle \frac{q_0(d)}{q^{\text{SWA}}_0(d)}. \tag{4.20}$$

In Chapter 6, the performance of the complete stochastic weighted algorithm for various forms of $q^{\text{SWA}}_0(d)$ (and hence $w_{\text{incept}}(d)$) is explored within the context of the twin-screw granulation model.

As a final point on the weighted inception jump process, ones notes that, given some sample volume $V_{\text{samp}}(z,t)$, the total rate of inception jump event is simply

$$R^{\text{SWA}}_{\text{incept}}(z,t) = V_{\text{samp}}(z,t) \int_{\mathbb{X}_{\text{incept}}} \int_{\mathbb{W}} I^{\text{SWA}}_{\text{solid}}(z,t,\mathrm{d}x) \tag{4.21}$$

$$= \frac{\dot{m}_{\text{incept}}(z) V_{\text{samp}}(z,t)}{V_{\text{real}}(z)\langle m_{\text{incept}} \rangle \langle w_{\text{incept}} \rangle}. \tag{4.22}$$

From the equation above, it is noted that the inclusion of the K_{w} ($\langle w_{\mathrm{incept}} \rangle$) term in Equation (4.14) has provided a free numerical which can be used to control the total rate of the inception process. This is important as it means that under sampling and over sampling of this jump process can be eliminated through the appropriate choice of $\langle w_{\mathrm{incept}} \rangle$.

Liquid-Addition and Nucleation

Liquid Addition
In the SWA, the liquid addition jump event results in the addition of a computational particle with the form

$$(z, x_{\mathrm{drop}}, w_{\mathrm{drop}}), \tag{4.23}$$

where x_{drop} is given by (3.3) and w_{drop} in the statistical weight of the incepted droplet particles. Unlike incepted solid particles, incepted droplet particles are mono-disperse, hence w_{drop} is simply a constant.

Extending the convergence criteria of Equation (4.13) to droplet inception, once sees that total jump rate for SWA droplet inception takes the form

$$I^{\mathrm{SWA}}_{\mathrm{drop}}(z,t,\mathrm{d}x,\mathrm{d}w) = \frac{\dot{V}_l(z)}{V_{\mathrm{real}}(z) v_{\mathrm{drop}} w_{\mathrm{drop}}} \delta_{w_{\mathrm{drop}}}(w)\delta_{x_{\mathrm{drop}}}(x)\mathrm{d}x\,\mathrm{d}w. \tag{4.24}$$

Given some sample volume $V_{\mathrm{samp}}(z,t)$, the jump rate associated with this process is then

$$R^{\mathrm{SWA}}_{\mathrm{drop}}(z,t) = V_{\mathrm{samp}}(z,t)\int_{\mathbb{X}}\int_{\mathbb{W}} I^{\mathrm{SWA}}_{\mathrm{drop}}(z,t,\mathrm{d}x,\mathrm{d}w) \tag{4.25}$$

$$= \frac{V_{\mathrm{samp}}(z,t)\dot{V}_l(z)}{V_{\mathrm{real}}(z) v_{\mathrm{drop}} w_{\mathrm{drop}}}. \tag{4.26}$$

An important point to be taken from (4.26) is that the rate of droplet inception jumps can be controlled through the selection of w_{drop}. This is critical when sampling rare model events which have a high impact on the ensemble properties of interest. In Chapter 6, the effect of the choice of w_{drop} on the performance of the complete simulation algorithm is investigated.

Nucleation
Remembering Chapter 3, the nucleation process is simply the rapid addition of primary particles and small agglomerates in the droplet zone to a droplet particle

or partially formed nuclei (i.e. a droplet which has acquired some degree of primary particle and/or agglomerate mass through the nucleation process). For this reason, they can be thought of a specialised type of coagulation event, which involves exactly one solid particle or aggregate and one droplet/partially formed nucleus. Following the approach taken by Kotalczyk and Kruis [82] to carry out coagulation processes, the addition of individual particles of the form (x_i, w_i) to the partially formed nucleus $(x_{\text{nuc}}, w_{\text{nuc}})$ is carried out as

$$\begin{matrix}(z, x_{\text{nuc}}, w_{\text{nuc}}),\\ (z, x_i, w_i)\end{matrix} \mapsto \begin{matrix}(z, T_{\text{nuc}}(x_{\text{nuc}}, x_i)\gamma_{\text{nuc}}(w_{\text{nuc}}, w_i)),\\ (z, x_{\text{nuc}}, w_{\text{nuc}} - \gamma_{\text{nuc}}(w_{\text{nuc}}, w_i)),\\ (z, x_i, w_i - \gamma_{\text{nuc}}(w_{\text{nuc}}, w_i)).\end{matrix} \tag{4.27}$$

In (4.27), T_{nuc} is the nucleation particle transform which represent the state of the partially formed nucleus $x_{\text{nuc}} \in \mathbb{X}_{\text{nuc}}$ after it has coalesced with particle $x_i \in \mathbb{X} \setminus \mathbb{X}_{\text{nuc}}$. γ_{nuc} is the nucleation weight transfer function which, again, follows the approach of Kotalczyk and Kruis [82] such that

$$\gamma_{\text{nuc}}(w_{\text{nuc}}, w_i) = \min(w_{\text{nuc}}, w_i). \tag{4.28}$$

The somewhat unusual form of the weight transfer function γ_{nuc} above arises from the difference between the process of combining physical particles and that of the combining weighted computational particles, as illustrated in Figure 4.2. In Figure 4.2(a), one see that, for a physical nucleation event, two particles combine to produce a single product particle. However, for the SWA nucleation event depicted in 4.2(b), two particles have combined to form two product particles. One can interpret the first and second computational particles on the LHS of 4.2(b) as having a statistical weight $w = 3$ and $w = 2$, respectively. As depicted by the dashed arrows in Figure 4.2(b), one can imagine two of the physical particle represented by the particle $(z, x_i, 3)$ pairing with each of the physical particles represented by particle $(z, x_j, 2)$ to create two physical product particles with the form (z, T_{nuc}). These product particles of the form (z, T_{nuc}) can equivalently be represented as a single weighted computational particle with the form $(z, T_{\text{nuc}}(x_i, x_j), 2)$. This leaves a single, unpaired physical particle of the form x_i which must be accounted for. This is done by creating a computational particle with the form $(z, x_i, 1)$. Note that the weight of the computational particle $(z, T_{\text{nuc}}(x_i, x_j), 2)$ is simply given by the maximum number of physical pairings that can be carried out between the 'reactant' species (i.e. those on the LHS

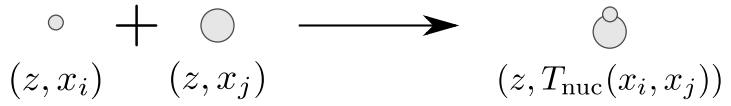

(a) A physical nucleation event.

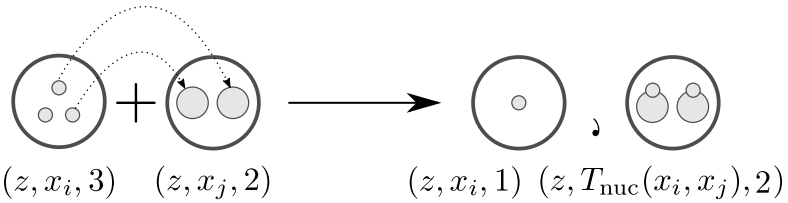

(b) A nucleation event between computational particles with different statistical weights.

Fig. 4.2 An illustration of the difference between the a physical nucleation event and a nucleation event between two weighted computational particles. 'Real' particles are represented by grey bodies. Computational particles are represented by dark grey circles containing real particles. The number of real particles in the computational particle is equal to the statistical weight w of the computational particle.

of the jump). This is equivalent to the minimum weight of the reactant species, hence the form of γ_{nuc} in Equation (4.28).

In order to recover the unweighted PBE nucleation process dynamics, the jump process in (4.27) occurs with rate [82]

$$K_{\text{nuc}}^{\text{SWA}}(x_{\text{nuc}}, w_{\text{nuc}}, x_i, w_i) = K_{\text{nuc}}(x_{\text{nuc}}, x_i) \max(w_{\text{nuc}}, w_i), \tag{4.29}$$

where K_{nuc} is the nucleation kernel.

One can show that the combination of the jump process (4.28), associated weight transfer function γ_{nuc} (4.27) and kernel (4.29) converges to the nucleation jump process of the unweighted PBE (3.2). To do so, firstly, for the sake of simplicity, one can consider the undeferred variant of the nucleation term in the weighted PBE (Equation (4.9)), which has the form

$$\begin{aligned}\int_{(x_{\text{nuc}}, w_{\text{nuc}}) \in \mathbb{X}_{\text{nuc}} \times \mathbb{W}, (x_i, w_i) \in (\mathbb{X} \setminus \mathbb{X}_{\text{nuc}}) \times \mathbb{W}} & [\psi(z, T_{\text{nuc}}(x_{\text{nuc}}, x_i), \gamma_{\text{nuc}}) + \psi(z, x_{\text{nuc}}, w_{\text{nuc}} - \gamma_{\text{nuc}}) \\ & + \psi(z, x_i, w_i - \gamma_{\text{nuc}}) - \psi(z, x_{\text{nuc}}, w_{\text{nuc}}) - \psi(z, x_i, w_i)] K_{\text{nuc}}^{\text{SWA}}(z, x_{\text{nuc}}, w_{\text{nuc}}, x_i, w_i) \\ & Q(z, t, \mathrm{d}x_{\text{nuc}}, \mathrm{d}w_{\text{nuc}}) Q(z, t, \mathrm{d}x_i, \mathrm{d}w_i).\end{aligned} \tag{4.30}$$

Substituting the definition $\psi(z,x,w) = \varphi(z,x)w$ and γ_{nuc} from (4.27) into the above expression yields

$$\begin{aligned}
&\int_{(x_{\text{nuc}},w_{\text{nuc}})\in\mathbb{X}_{\text{nuc}}\times\mathbb{W},\,(x_i,w_i)\in(\mathbb{X}\setminus\mathbb{X}_{\text{nuc}})\times\mathbb{W}} \\
&[\varphi(z,T_{\text{nuc}}(x_{\text{nuc}},x_i))\min(w_{\text{nuc}},w_i) + \varphi(z,x_{\text{nuc}})(w_{\text{nuc}} - \min(w_{\text{nuc}},w_i)) \\
&\quad + \varphi(z,x_i)(w_i - \min(w_{\text{nuc}},w_i)) - \varphi(z,x_{\text{nuc}})w_{\text{nuc}} - \varphi(z,x_i)w_i] \\
&\quad K_{\text{nuc}}^{\text{SWA}}(z,x_{\text{nuc}},w_{\text{nuc}},x_i,w_i)Q(z,t,\mathrm{d}x_{\text{nuc}},\mathrm{d}w_{\text{nuc}})Q(z,t,\mathrm{d}x_i,\mathrm{d}w_i) \\
&= \int_{(x_{\text{nuc}},w_{\text{nuc}})\in\mathbb{X}_{\text{nuc}}\times\mathbb{W},\,(x_i,w_i)\in(\mathbb{X}\setminus\mathbb{X}_{\text{nuc}})\times\mathbb{W}} \\
&\quad [\varphi(z,T_{\text{nuc}}(x_{\text{nuc}},x_i)) - \varphi(z,x_{\text{nuc}}) - \varphi(z,x_i)]\min(w_{\text{nuc}},w_i) \\
&\quad K_{\text{nuc}}^{\text{SWA}}(z,x_{\text{nuc}},w_{\text{nuc}},x_i,w_i)Q(z,t,\mathrm{d}x_{\text{nuc}},\mathrm{d}w_{\text{nuc}})Q(z,t,\mathrm{d}x_i,\mathrm{d}w_i).
\end{aligned} \tag{4.31}$$

This can be further reduced by substituting the SWA kernel in (4.29) into the above expression (noting that $\min(w_{\text{nuc}},w_i)\max(w_{\text{nuc}},w_i) = w_{\text{nuc}}w_i$) to give

$$\begin{aligned}
&\int_{(x_{\text{nuc}},w_{\text{nuc}})\in\mathbb{X}_{\text{nuc}}\times\mathbb{W},\,(x_i,w_i)\in(\mathbb{X}\setminus\mathbb{X}_{\text{nuc}})\times\mathbb{W}} [\varphi(z,T_{\text{nuc}}(x_{\text{nuc}},x_i)) - \varphi(z,x_{\text{nuc}}) - \varphi(z,x_i)] \\
&\quad K_{\text{nuc}}(z,x_{\text{nuc}},x_i)w_{\text{nuc}}w_i Q(z,t,\mathrm{d}x_{\text{nuc}},\mathrm{d}w_{\text{nuc}})Q(z,t,\mathrm{d}x_i,\mathrm{d}w_i).
\end{aligned} \tag{4.32}$$

Finally, by applying the equality (4.8) one arrives at an equivalent expression for (4.30) with the form

$$\begin{aligned}
&\int_{x_{\text{nuc}}\in\mathbb{X}_{\text{nuc}},\,x_i\in\mathbb{X}\setminus\mathbb{X}_{\text{nuc}}} [\varphi(z,T_{\text{nuc}}(x_{\text{nuc}},x_i)) - \varphi(z,x_{\text{nuc}}) - \varphi(z,x_i)] \\
&\quad K_{\text{nuc}}(z,x_{\text{nuc}},x_i)\lambda(z,t,\mathrm{d}x_{\text{nuc}}))\lambda(z,t,\mathrm{d}x_i),
\end{aligned} \tag{4.33}$$

which is the undeferred variant of the nucleation jump process in the unweighted PBE (Equation (3.2)) with $x = x_{\text{nuc}}$, $y = x_i$, $w = w_{\text{nuc}}$ and $u = w_i$.

Since it is computationally expensive to compute the expression in (4.29) for all possible ensemble particles (x_i,w_i), a majorant form of this kernel is used. This takes the form:

$$\tilde{K}_{\text{nuc}}^{\text{SWA}}(x_{\text{nuc}},w_{\text{nuc}},x_i,w_i) = K_{\text{nuc}}(x_{\text{nuc}},x_i)(w_{\text{nuc}} + w_i). \tag{4.34}$$

The procedure used to pick particles $(x_i,w_i),(x_{\text{nuc}},w_{\text{nuc}})$ to take part in the jump process (4.27) is discussed later Chapter 6. In order to ensure that the jump

process (4.27) is performed at the correct rate, upon selection of the particle pair (x_i, w_i), $(x_{\text{nuc}}, w_{\text{nuc}})$ to be added to the partially formed nucleus, the jump is performed with probability

$$\frac{\max(w_i, w_{\text{nuc}})}{w_i + w_{\text{nuc}}}, \tag{4.35}$$

otherwise the jump is fictitious (i.e one moves to the next jump event without altering the ensemble). For a more detailed account of the majorant kernel technique the reader is referred to Lee et al. [94].

Combining droplet inception and nucleation

As noted in Chapter 3, the addition of particles to the droplet or partially formed nucleus is assumed to be rapid relative to all other particle processes (for the excipient and droplet material combinations of interest within this thesis) i.e. $k_{\text{nuc}} \to \infty$. From an SWA perspective, this means

$$\tilde{K}^{\text{SWA}}_{\text{nuc}}(x_{\text{nuc}}, w_{\text{nuc}}, x_i, w_i) \to \infty, \tag{4.36}$$

and so, if

$$\int_{\mathbb{X}_{\text{nuc}}} \int_{\mathbb{W}} Q(z, t, \mathrm{d}x, \mathrm{d}w) > 0, \tag{4.37}$$

and

$$\int_{\mathbb{X}\setminus\mathbb{X}_{\text{nuc}}} \int_{\mathbb{W}} \tilde{K}^{\text{SWA}}_{\text{nuc}}(x_{\text{nuc}}, w_{\text{nuc}}, x_i, w_i) Q(z, t, \mathrm{d}x, \mathrm{d}w) > 0, \tag{4.38}$$

then the nucleation jump rate

$$R^{\text{SWA}}_{\text{nuc}}(z, t) \to \infty. \tag{4.39}$$

Thus, jump events of the form (4.27) are selected and carried out until inequality (4.37) and/or inequality (4.38) are no longer satisfied (without any other jump processes occurring between applications of (4.27)). This is equivalent to saying that nucleation stops when there are no droplets or partially formed nuclei and/or there are no appropriately sized primary particles or agglomerates in the system. It follows that, after any liquid inception event (at which point inequality (4.37) is satisfied since $x_{\text{drop}} \in \mathbb{X}_{\text{nuc}}$), nucleation jump events are repeatedly applied to the droplet particle. This occurs in an iterative manner i.e particle $(z, T_{\text{nuc}}(x_{\text{nuc}}, x_i), \gamma_{\text{nuc}}(w_{\text{nuc}}, w_i))$ is passed back through the jump process (4.27)

with a new ensemble particle x_i. This iterative process continues until

$$T_{\text{nuc}}(x_{\text{nuc}}, x_i) \notin \mathbb{X}_{\text{nuc}}. \tag{4.40}$$

When (4.40) is satisfied, $T_{\text{nuc}}(x_{\text{nuc}}, x_i)$ may no longer be passed through jump (4.27) and a new computational particle is incepted into compartment z with the form

$$(z, T_{\text{nuc}}(x_{\text{nuc}}, x_i), \gamma_{\text{nuc}}(w_{\text{nuc}}, w_i)). \tag{4.41}$$

In the event that the jump (4.27) creates two partially formed nuclei[1], then jump (4.27) must also be separately carried out on particle

$$(z, x_{\text{nuc}}, w_{\text{nuc}} - \min(w_{\text{nuc}}, w_i)),$$

until the stopping condition (4.40) is satisfied for this particle.

Since the nucleation process follows directly from any droplet inception event, and, since nucleation jumps occur consecutively until the described stopping condition is met, the droplet inception jump and complete formation of the nuclei particles can be carried out as a unified jump process. Given that this combined jump process is initiated by a liquid inception event, the rate of the unified process within a given sample volume is simply $R_{\text{drop}}(z,t)$. This unified jump process will be referred to hereafter as SWA immersion nucleation.

An important point to note is that the first time that the nucleation jump (4.27) is carried out after a droplet inception event, the partially formed nuclei is simply the newly incepted droplet particle, and hence $(z, x_{\text{nuc}}, w_{\text{nuc}}) = (z, x_{\text{drop}}, w_{\text{drop}})$ (at this point only). The implementation of this immersion nucleation process is considered in Chapter 6.

To the best of the author's knowledge, this is the first time that such a jump process has been formulated and utilised to carry out an immersion nucleation process in a stochastic fashion.

Coagulation

SWA coagulation jumps take different forms depending on whether the particles can be successfully coalesced. Additionally, this jump process includes a com-

[1] Note that additional, partially formed nuclei particles can be formed by jump (4.27) if $w_{\text{nuc}} > w_i$.

paction transformation on the particles involved. For successful coalescence, the jump takes the form

$$(z,x_i,w_i),(z,x_j,w_j) \mapsto (z,T_{\text{comp}}(x_i+x_j),\gamma_{\text{coag}}(x_i,w_i,x_j,w_j)),(z,x_j,w_j), \tag{4.42}$$

and for unsuccessful coalescence (i.e. a compaction and subsequent rebound):

$$(z,x_i,w_i),(z,x_j,w_j) \mapsto (z,T_{\text{comp}}(x_i),w_i),(z,x_j,w_j). \tag{4.43}$$

In the above, T_{comp} is the compaction transformation and in (4.42), γ_{coag} is the coagulation weight transfer function. As in Lee et al. [96], we impose that

$$\gamma_{\text{coag}}(x_i,w_i,x_j,w_j) = w_i \frac{m(x_i)}{m(x_i+x_j)}. \tag{4.44}$$

The convergence of SWA collisions and coagulation jumps with the form (4.42) and (4.43) with weight transfer functions of the form in Equation (4.44) to the appropriate form in the unweighted PBE (Equation (3.2)) has been demonstrated by Patterson et al. [135] and will therefore not be considered in this work. The SWA coagulation kernel takes the form

$$K_{\text{coag}}^{\text{SWA}}(z,x_i,w_i,x_j,w_j) = K_{\text{coag}}(z,x_i,x_j)w_j \tag{4.45}$$

and total collision jump rate in compartment z is

$$R_{\text{col}}^{\text{SWA}}(z,t) = \frac{1}{V_{\text{samp}}(z,t)} \sum_{i\neq j}^{N(z,t)} K_{\text{col}}(z,x_i,x_j)w_j. \tag{4.46}$$

Breakage

The breakage jumps take the form

$$(z,x_i,w_i) \mapsto (z,y,\gamma_{\text{frag}}(x_i,w_i,y)), \tag{4.47}$$

which occurs at rate

$$g_{\text{break}}(z,x). \tag{4.48}$$

Here, γ_{frag} is the breakage weight transfer function which takes the form [96]

$$\gamma_{\text{frag}}(x_i, w_i, y) = w_i \frac{m(x_i)}{m(y)}. \tag{4.49}$$

As in [94, 96], y is selected as:

$$y = x_j, \quad \text{with probability} = \frac{m(x_j)}{m(x_i)}, \tag{4.50}$$

$$y = x_i - x_j, \quad \text{with probability} = 1 - \frac{m(x_j)}{m(x_i)}, \tag{4.51}$$

and x_j is selected according to the probability measure B, characterised by model Equations (3.33)-(3.35).

The total breakage jump rate in compartment z is

$$R^{\text{SWA}}_{\text{break}}(z,t) = \sum_{i=1}^{N(z,t)} g_{\text{break}}(z, x_i). \tag{4.52}$$

Transport

The inflow and outflow processes of the weighted PBE (Equation (4.9)) are unified into a single jump process with the form

$$(z, x_i, w_i) \mapsto (z+1, x_i, F_{\text{c}}(z) w_i), \tag{4.53}$$

where F_{c} is the transport weight scaling factor. The weight scaling factor, as employed in [95], scales the effective rates of the inflow process, such that total inflow jump rate is equal to the unscaled outflow jump rate (and hence inflow and outflow may be carried out as a unified jump process). Again, it is assumed that all compartments are of equal real volume.

The jump (4.53) occurs with rate

$$\frac{1}{\tau(z)}, \tag{4.54}$$

indicating that (z, x_i, w_i) is to be selected uniformly from the ensemble of compartment z. As a reminder to the reader, $\tau(z)$ is the characteristic residence time of compartment z.

F_c takes the form [116]

$$F_c(z) = \frac{V_{\text{samp}}(z+1)}{V_{\text{samp}}(z)}. \tag{4.55}$$

The total transport jump rate in compartment z is [94–96]

$$R^{\text{SWA}}_{\text{outflow}}(z,t) = \frac{N(z,t)}{\tau(z)}. \tag{4.56}$$

4.3.6 Continuous processes

Intra-particle processes (in this case of this model, liquid penetration) may be modelled as continuous processes. To minimise the computational cost of modelling such mechanisms, these are carried out using the linear process deferment algorithm (LPDA) [133]. LPDA has been successfully employed in the solution of stochastic population balance models for granulation [96], silica nanoparticle synthesis [116] and soot particle formation [133, 135]. In the LPDA, each stochastic particle is time stamped and the application of all linear processes (via the extended deferment operator $\tilde{D}_t$) is deferred until:

1. The next occurrence of a non-linear event (e.g. coagulation). At which point $\tilde{D}_t$ is applied to the particles involved in the jump.
2. The compartmental system has been simulated to or beyond the next deferment check point time (based on predefined list of deferment check points). At which point $\tilde{D}_t$ is applied to all stochastic particles, thereby updating each particle to the current simulation time. This occurs between stochastic jumps events.

The extended deferment operator $\tilde{D}_t : \mathbb{X} \times \mathbb{W} \to \mathbb{X} \times \mathbb{W}$ can be expressed in terms of the unweighted deferment operator of Chapter 3 as

$$\tilde{D}_t(w,x) = (w, D_t x). \tag{4.57}$$

Chapter 5

Application of the model

In this chapter, the predictive ability of the twin-screw model developed in Chapter 3 is assessed through comparison with an experimental data set. The model is solved using the stochastic weighted population balance methodology described in Chapter 4. The experimental system to be simulated is described and the associated model inputs are provided. This is followed by a presentation of the methodology used to estimate the unknown parameters within the twin-screw model. Simulations are carried out using the optimised set of rate constants for various operating liquid-solid mass feed ratios and the results are compared against experimental data. This chapter concludes with a review of the model's performance and identification of areas for potential model refinement.

5.1 Experimental description

The experimental studies by El Hagrasy et al. [46] were used to test the model. This study employed a screw configuration consisting of a conveying section followed by a section of conveying and kneading elements and then an additional conveying section. This is modelled as a series of three well-mixed compartments as illustrated in Figure 5.1. Compartments $z = 1$ and $z = 3$ are assumed to represent pure conveying sections, which are asserted to share the same set of rate constants. Droplet inception and nucleation are only permitted in the first compartment. The central conveying/kneading compartment ($z = 2$) is permitted to have different collision, breakage and compaction rates, relative to the pure conveying zones. The penetration rate is assumed to be a material constant and is enforced to be the same in each compartment. It is assumed that transformation

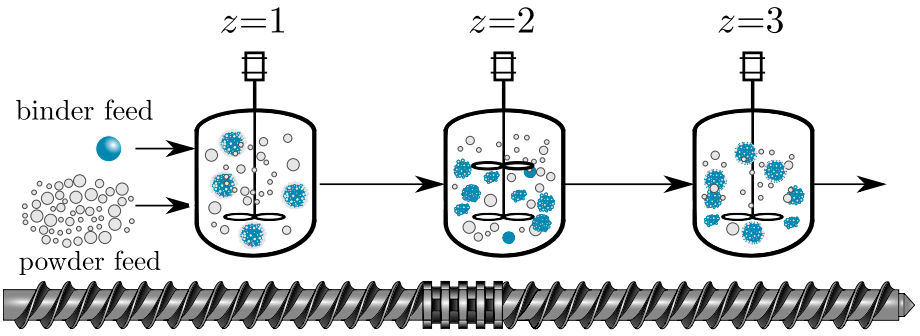

Fig. 5.1 Compartmental representation of the twin-screw.

of the feed material is limited prior to the binder feed location of the twin-screw system. For this reason, the twin-screw system is modelled from the liquid injection point onwards. The PSD of primary particles of the Impalpable Lactose grade used by El Hagrasy et al. [46] and simulated in this chapter is presented in Figure 5.2.

5.2 Simulation conditions

The model parameters used in the simulations within this chapter are presented in Table 5.1. All simulations were performed with $N_{\max} = 1024$ and each compartment is initialised with $N(z,0) = 0.75N_{\max}$. The initial particle distribution on the space $\mathbb{X} \times \mathbb{W}$ follows the inception distribution $q^{\mathrm{SWA}}_{0,\mathbb{X}}(x)$. The statistical weights of incepted particles is described by the variable weighted inception algorithm that is presented in detail in Chapter 6. This method recovers the

Table 5.1 Summary of simulation parameters.

Parameter	Type	Value	Unit	Source
d_{nozzle}	Operating parameter	2×10^{-3}	m	[46]
$\dot{m}_{\text{feed}}$	Operating parameter	4.0	kg hr^{-1}	[46]
n_{screw}	Operating parameter	6.67	rev s^{-1}	[46]
V_{real}	Equipment geometry	1.35×10^{-5}	m^3	Estimated from [146]
e_{coag}	Material property	0.2	-	[111]
ρ_{l}	Material property	998	kg m^{-3}	[66]
ρ_{s}	Material property	1545	kg m^{-3}	[176]
μ	Material property	10^{-3}	Pa s	[66]
d_{max}	Model parameter	3.31×10^{-6}	m	Estimated from [46]
d_{min}	Model parameter	8.26×10^{-4}	m	Estimated from [46]
h_{a}	Model parameter	5×10^{-6}	m	Estimated
n_{comp}	Model parameter	3	-	Selected
N_{real}	Model parameter	8.80×10^{7}	-	Estimated
U_{col}	Model parameter	0.3	m s^{-1}	Estimated
$v_{\text{frag}}^{\text{min}}$	Model parameter	8.18×10^{-12}	m^{-3}	Estimated
$v_{\text{parent}}^{\text{min}}$	Model parameter	1.80×10^{-11}	m^{-3}	Estimated
$v_{\text{nuc}}^{\text{max}}$	Model parameter	v_{drop}	m^3	Estimated
α_{daughter}	Model parameter	5.0	-	Estimated
β_{daughter}	Model parameter	2.0	-	Estimated
ε_{min}	Model parameter	0.5	-	Estimated
ν_{max}	Model parameter	0.5	-	Estimated
τ	Model parameter	2.76	s	[7]
ϕ_{max}	Model parameter	1.08	-	Estimated

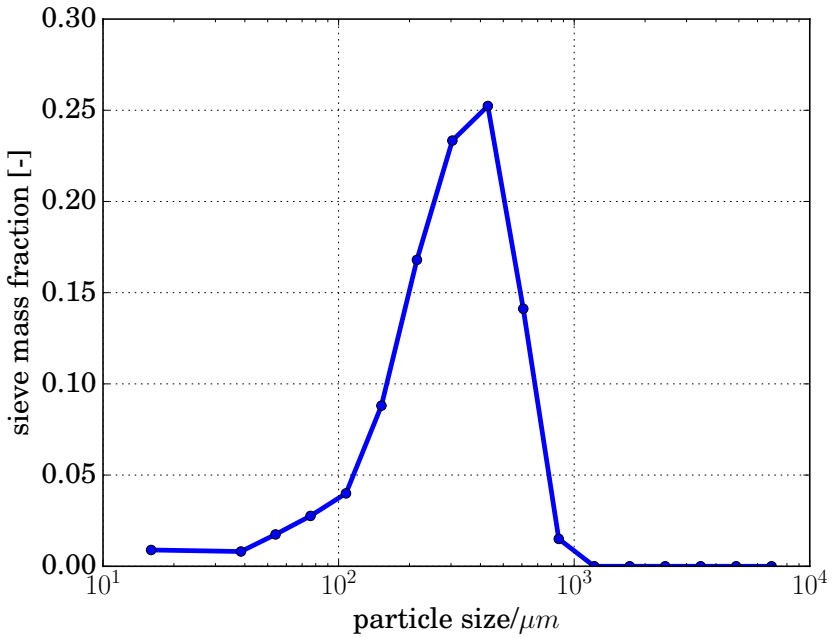

Fig. 5.2 Initial particle size distribution for the Lactose Impalpable grade simulated [46].

physical primary particle size distribution used for the Lactose Impalpable grade used in El Hagrasy et al. [46]. For the droplet inception and nucleation processes, all simulations were carried out with w_{drop} =0.001. Since the twin-screw granulation system is a continuous system, one is generally interested in the steady state solution of the twin-screw PBM. As such, dynamic results are not assessed in this work. Visual analysis of the responses showed that the time at which simulation responses ceased to drift with t was controlled by the total system residence time. The final simulation time $t_{\text{stop}} = 5\sum_{z\in\mathbb{Z}} \tau(z) \approx 40$s proved to be an acceptable choice and is used across all numerical studies in this paper.

Each simulation is carried out until $t \geq t_{\text{stop}}$ and this process is repeated n_{runs} times, each time with a different seed to the pseudo-random number generator. Henceforth, each simulation repetition will be referred to as a run.

5.3 Quantification of errors

For the stochastic simulations in this work, temporal functionals $M(t)$ (such as sieve mass fraction) are reported as averages taken over all runs as

$$\eta(t) = \frac{1}{n_{\text{runs}}} \sum_{i=1}^{n_{\text{runs}}} M_i(t), \tag{5.1}$$

where the functional may be a particle ensemble property, such as the mass fraction of particles in a particular sieve class.

The half-width of the confidence internals are

$$c(t) = 1.64 \sqrt{\frac{\sum_{i=1}^{n_{\text{runs}}} (M_i(t) - \eta(t))^2}{n_{\text{runs}}^2}}, \tag{5.2}$$

which corresponds to a confidence interval $P = 0.9$ [96].

5.4 Parameter estimation

The unknown rate constants (seven in total) are estimated using experimental PSDs from El Hagrasy et al. [46] at LSR values of 0.15, 0.25 and 0.35. The quality of the model fit against the experimental data is quantitatively measured using a weighted sum-of-squares objective function OF over all N_{exp} experimental conditions and N_{response} model (and experimental) responses as:

$$OF = \sum_{i=1}^{N_{\text{exp}}} \sum_{j=1}^{N_{\text{response}}} \left(\frac{y_{j,i}^{\text{model}} - y_{j,i}^{\text{exp}}}{\sigma_j} \right)^2. \tag{5.3}$$

Here, $y_{i,j}^{\text{model}}$ is the j^{th} model response for the i^{th} LSR value used and $y_{j,i}^{\text{exp}}$ is the associated experimental response. Mass based percentiles diameters d25, d50, d75 and d95 of the granular product are used as the model and experimental responses. These are weighted, respectively, using weighting factors σ of 25μm, 50μm, 75μm and 95μm.

The geometry of the objective function is highly complex, containing multiple ridges and local minima. For this reason, a quasi-random search is performed over the parameter space, followed by a (more local) Hooke-Jeeves optimisation [67]. The initial search is carried out by generating a quasi-random sequence of rate

constant vectors known as Sobol sequences [18]. Sobol sequences are used in order to spread the model evaluation points more evenly across the parameter space. The Hooke-Jeeves algorithm is selected for the local optimisation since it is a 'derivative-free' optimisation technique. This characteristic is highly desirable in the context of this thesis, since derivative approximation by finite differences is problematic with models whose response is subject to stochastic noise. Five Hooke-Jeeves optimisations are carried out, starting from each of the five best Sobol points (i.e. those with the lowest OF value).

Preliminary parameter estimation showed that very similar product PSDs could be obtained for very different sets of rates constants. For example, using the same wide search space for the breakage rate constant k_{att} in both the pure conveying and partial kneading section may result in a situation in which most of the breakage occurred in the conveying sections and very little in the partial kneading section and vice-versa, both giving relatively similar product PSDs. Since only the final PSD is used in the fitting process (mid-barrel experimental PSD data was not available), unphysical PSD evolutions along the network are not penalised by the objective function. Hence, such PSD evolutions must be eliminated through careful selection of the search space for each rate constant, reflecting what is known from experimental investigation. As previously discussed, the body of experimental TSG literature would suggest that the breakage and compaction rates in the kneading elements are significantly higher than those present in pure conveying sections (though conveying sections are known to break large agglomerates using a cutting action [106]). Thus, the parameter limits for k_{comp} and k_{att} in the central, partial kneading compartment ($z = 2$) are chosen such that they are higher than those of the pure conveying compartments ($z = 1,3$). To assess the predictive power of the model, the optimised rate constants are then used to model two additional experimental cases with intermediate LSR values of 0.2 and 0.3.

Table 5.2 Rate constant bounds used in the parameter estimation process.

Compartment index z	1,3			2			1-3
Parameter	k_{col}	k_{att}	k_{comp}	k_{col}	k_{att}	k_{comp}	k_{pen}
Unit	m^3	m^{-1}s	-	m^3	m^{-1}s	-	$\text{kg}^{\frac{1}{2}}\text{m}^{-\frac{7}{2}}\text{s}^{-\frac{3}{2}}$
Lower bound	10^{-12}	1.68×10^{4}	0.01	10^{-12}	1.68×10^{6}	0.6	10
Upper bound	10^{-9}	1.68×10^{7}	0.6	10^{-9}	1.68×10^{10}	1.0	10^{6}
Scaling	Log	Log	Linear	Log	Log	Linear	Log

The parameter estimation steps are carried out using the Model Development Suite (MoDS) [120]. MoDS is an advanced software package capable of analysing 'black-box' models. MoDS has been successfully used in numerous applications, from the global sensitivity analysis of a silica nanoparticle model [117], to the experimental design and parameter estimation of a combustion engine model [121] and more [25, 108, 122, 128].

5.5 Model results and discussion

5.5.1 The effect of liquid flowrate on particle size distribution

A comparison between the model and experimental product PSD is presented in Figure 5.3. The product ensembles of each simulation are sieved using a sieve set starting from 32μm to 8064μm with a $\sqrt{2}$ geometric progression. Sieve mass fractions are plotted against the mid-point of the corresponding sieve intervals. There is an obvious trend in the results whereby the intensity of the primary particle mode is reduced with increasing LSR, leading to a reduction in the fines and a larger mean granule size, as observed in TSG experiments [37, 39, 152]. The main disparities occur at higher LSR values where the largest particles size classes produced in the experiment are not captured by the model. The model PSD is bimodal in all cases, consisting of a primary particle mode and an additional mode composed of nuclei fragments which have gone through breakage, coagulation and compaction processes. Such bimodality is generally a feature of TSG product PSD. El Hagrasy et al. [46] hypothesised that the inherently bimodal nature of the twin-screw device was a result of the liquid addition method, resulting in a non-uniform liquid distribution. El Hagrasy and Litster [47] also observed that the liquid distribution becomes more uniform with the addition of more kneading blocks. The experimental PSD for low to moderate LSR in Figure 5.3 may well be evolved from a more pronounced bimodal distribution, with a degree of overlap between the modes. Such a distribution would be subjected to reduction in intensity along the barrel length. The current model appears to fail in capturing some of the more subtle processes that lead to the mitigation of this bimodality, even in the presence of relative few kneading elements.

There is a clear over-prediction of fines by the model at high LSR values (Figure 5.3(c) and 5.3(e)). This may indicate the need for a layering mechanism in the

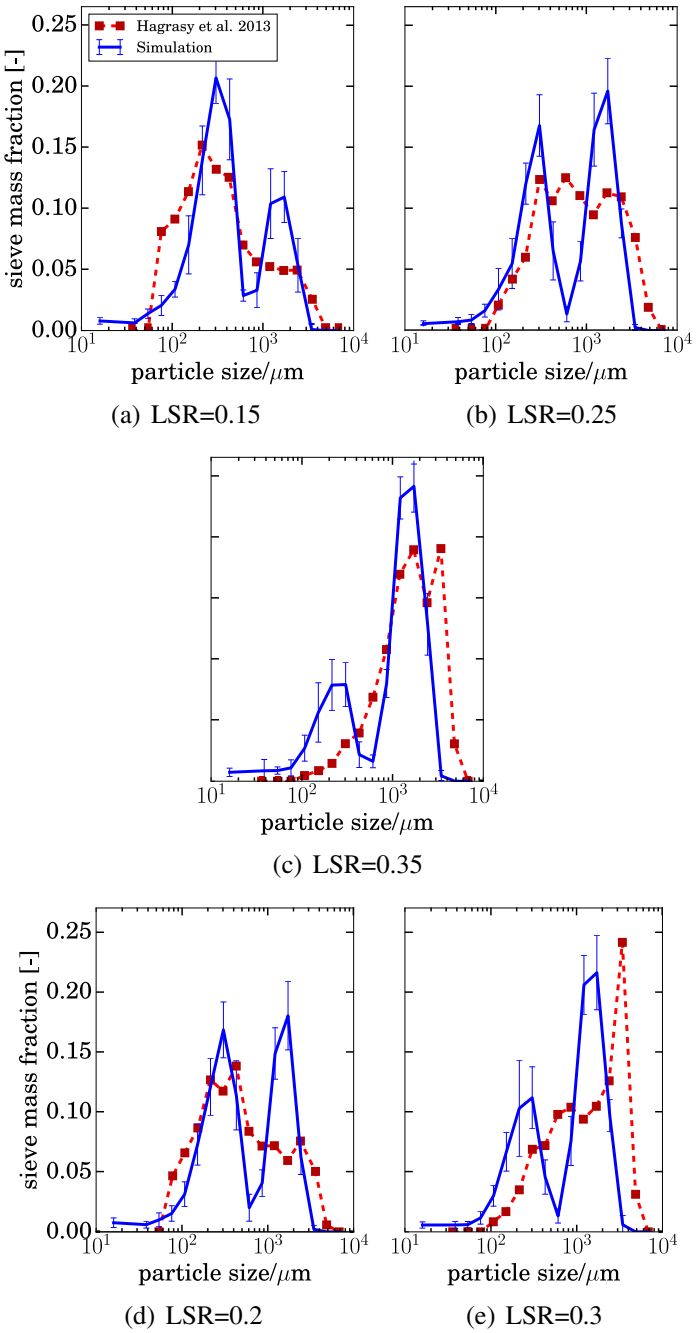

(a) LSR=0.15 (b) LSR=0.25

(c) LSR=0.35

(d) LSR=0.2 (e) LSR=0.3

Fig. 5.3 Simulation PSDs compared with the experimental results of El Hagrasy et al. [46] for the Lactose Impalpable system. LSR values which were used in the fitting of the rate constants are presented in (a)-(c) and 'blind tested' intermediate LSR values in (d) and (e). The lines have been added to guide the eye.

model. This would allow primary particles to become attached to the surface of larger, surface wet agglomerates as a rapid continuous process or additional particle jump process. This would ultimately lead to the separate treatment of the rates and particle transforms associated with agglomerate-primary and agglomerate-agglomerate collisions. Such layering mechanisms have been implemented in the context of a sectional TSG model by Barrasso and Ramachandran [12] and a stochastic model for a high-shear batch mixer by Oullion et al. [126]. The introduction of a layering mechanism is left to Chapter 7.The failure to produce the pronounced peak at 4000μm in the case where LSR=0.3 may also indicate that a less aggressive and/or more versatile breakage kernel (possibly with a variable volume exponent) may be required in the future. This peak may also correspond to particles which have become strengthened through compaction in the kneading elements. Again, such structural changes may need to introduced into the breakage functional to capture the resistance of such particles to further breakage.

Moving to the lower LSR operating range, the disparity between model and experiment in the lowest sieve classes (Figures 5.3(a) and 5.3(d)) indicates that, in the real system, large primary particles and/or agglomerates may undergo attrition along the barrel length, therefore acting as a source of 'fines'. Another possible explanation for this discrepancy is that the preferential incorporation of larger primary particles in the nucleation mechanism of the model is more pronounced that it is in the real system. Dhenge et al. [38] showed that the material in the barrel became less cohesive with decreasing LSR, resulting in a material that was less resistant to flow and subject to shorter residence times (though this was only tested to LSR values as low as 0.25). This reduction in residence time indicates a lower degree of barrel filling at lower LSR values and may, as suggested by Thompson and Sun [165], result in the material not being protected from the high shear zone at the barrel wall, causing subsequent attrition of the largest primary particles in the low LSR regime. Since the breakage of dry primary particles is distinct from the breakage of wet agglomerates, (which may be able to deform and elongate) it is likely that distinct breakage models are required to accurately capture the breakage process for each phase. Later, in Chapter 7, more complex breakage mechanisms are considered.

Across the complete LSR operating range, the discrepancies between the model and experimental PSD in Figure 5.3 may have been affected, to some degree, by the varying aspect ratio of particles produced experimentally. It is known that the aspect ratio of particles generally decreases with increasing LSR, producing more

rounded particles [38, 39, 86], however, as demonstrated by El Hagrasy et al. [46], this breaks down at very high LSR. At this high LSR operating range, long extrudate-like particles are produced as the mixture becomes more of a paste, making the geometrical variations particularly hard to capture from a modelling perspective. Ultimately, the presence of particles with high aspect ratios may skew the sieve analysis, depending on the particle orientation. It will also affect the nature of subsequent particle breakage and growth. In the current model, particles are considered to be spherical. More complex particle descriptions with element-specific shape transformations may need to be taken into account in future modelling works. Due to the highly extensible nature of stochastic models, it is possible to track such additional features without significantly affecting the computational cost of the solution process. Nevertheless, work would be required to elucidate the effects of each type of element and how these effects depend on the properties of the particles involved.

Another potential source of error in the model is the assumption of equal residence times across all compartments. As TSG Positron Emission Particle Tracking (PEPT) studies have shown [97, 151], the material fill ratio before and in the kneading block is generally greater than that in the final conveying zone. This would extend the residence time of the kneading block and thereby reduce the time spent by particles in conveying sections. The fill level is known to play an important role in determining the shape and size of the particles since this determines the degree of compaction [86] and, again, may also protect particles from contacting the high shear boundary between the wall and the screw, thereby mitigating breakage [165]. This variation in mass distribution could be incorporated into the model by way of a flow model (such as that done for hot melt extrusion by Eitzlmayr et al. [45]) or, alternatively, by coupling the population balance to simulations using the Discrete Element Method (DEM), though such DEM couplings come at a high computational cost.

5.5.2 Evolution of the particle size distribution along the barrel

In this section the evolution of the model PSD is assessed along the length of the network (or equivalently, the length of the barrel) for an operating LSR of 0.25. Figure 5.4 shows the PSD in each compartment along the network and Table 5.3 details the optimised rate constants for each compartment.

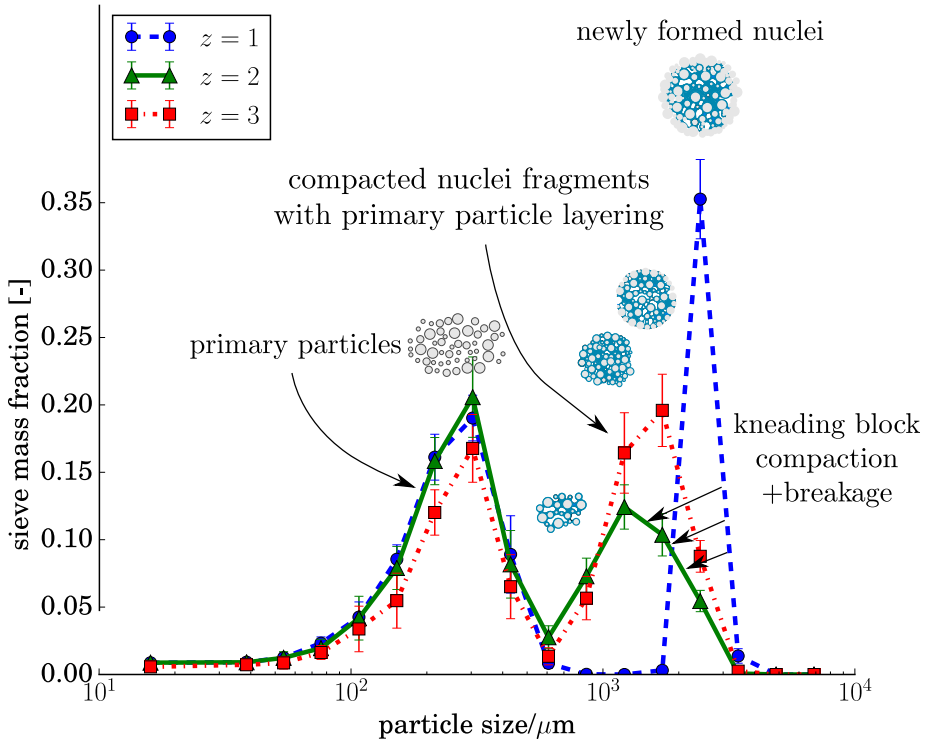

Fig. 5.4 Spatial PSD evolution for simulation with LSR=0.25.

It is observed that the dominant mechanism in the first compartment ($z = 1$) is nucleation, which causes a pronounced peak in the PSD around 2500μm. As a result of the bounds used for parameter estimation, in Table 5.3 we see that conveying-only compartments ($z = 1,3$) are subject to a lower degree of breakage (k_{att}) relative to the compartment containing the kneading elements ($z = 2$). The reduced breakage rate allowed the oversized nucleates to co-exist with the remaining primary powder in a highly bimodal distribution, alluding to the inherent bimodality-by-liquid-inception suggested by El Hagrasy et al. [46]. The position of the nuclei peak relative to the droplet size of 2000μm indicates that nuclei have been subjected to a moderate degree of compaction in the first compartment following their formation.

Table 5.3 Optimised rate constants.

Compartment index z	1,3			2			1-3
Parameter	k_{col}	k_{att}	k_{comp}	k_{col}	k_{att}	k_{comp}	k_{pen}
Unit	m^3	m^{-1}s	-	m^3	m^{-1}s	-	$\text{kg}^{\frac{1}{2}}\text{m}^{-\frac{7}{2}}\text{s}^{-\frac{3}{2}}$
Lower bound	10^{-12}	1.68×10^{4}	0.01	10^{-12}	1.68×10^{6}	0.6	10.0
Upper bound	10^{-9}	1.68×10^{7}	0.6	10^{-9}	1.68×10^{10}	1.0	10^{6}
Value	1.21×10^{-10}	9.42×10^{6}	0.395	9.99×10^{-13}	1.09×10^{9}	0.954	10.0

Moving from $z = 1$ to $z = 2$ in Figure 5.4, one sees that a high degree of compaction and breakage has broken down the large nuclei into smaller, more dense fractions, consistent with the findings of Djuric and Kleinebudde [41]. It is also noted that the penetration rate constant has reached its lower bound and this process has effectively turned of. This is likely a reflection of the competition between the compaction and penetration processes in. These processes compete to move liquid to and from the surface of the particles, respectively. Thus, the amount of surface liquid available during coagulation events is not sensitive to the absolute the value of k_{comp} and k_{pen} but rather their relative magnitudes. This coupling is undesired and is an area which will be addressed in Chapter 7. The squeezing effects of the compaction processes are further evident from the average particle composition statistics (Figure 5.5), in which a slight reduction in internal liquid (and resulting increase in external liquid) is evident in the transition between $z = 1$ and $z = 2$. This replicates the squeezing process within kneading blocks observed in numerous experimental studies [38, 47, 152, 167, 168].

It is also noted that breakage is the dominant process in the second compartment (kneading zone) and that the coagulation rate constant has reached its lower bound, indicating very limited coagulation within this compartment. It is likely that similar ratios of k_{att} to k_{col} could feasibly generate similar size distributions within $z = 2$ due to the competing nature of the coagulation and breakage processes.

As the particles transition from the kneading zone to the final conveying zone, a degree of coalescence between primary particles and compacted (i.e. surface wet) agglomerates is observed. At this stage, the combination of moderate breakage and low compaction rate allows particles to grow whilst increasing in porosity (the reader is reminded that successful coalescence events result in an increase in particle pore volume in the model). This is in line with the production of large friable agglomerates from conveying only section observed in TSG and twin-screw extrusion systems [41].

5.6 Chapter conclusions

This chapter has assessed the predictive abilities of the twin-screw model. The model performed reasonably well against experiment at low LSR values but showed an over-prediction of fines at higher LSR values. A consistently bi-modal PSD was predicted by the model for all LSR tested. This bi-modality

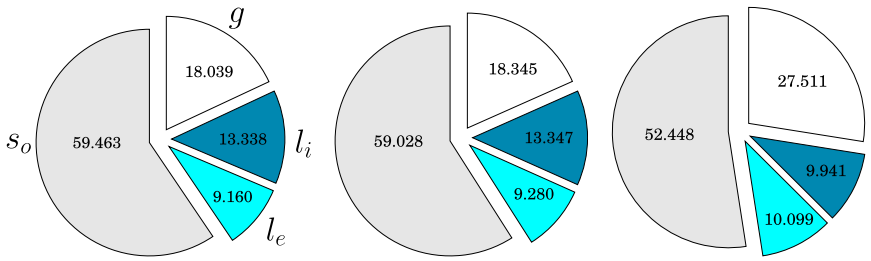

(a) $z = 1$ (b) $z = 2$ (c) $z = 3$

Fig. 5.5 Number averaged particle composition along the length of the compartment network with an operating LSR=0.25.

has primarily resulted from lack of interaction between the primary particle and agglomerates phases, leading to a 'dip' in the PSD at the point of cross over of the modes.

Based on the results of this study a number of recommendations for model improvements and future analysis can be made. Firstly, the introduction of a layering mechanism may mitigate the over-prediction of fines by the current model. This may also better reflect the difference between collision events involving a mixture of primary particles and agglomerates and those between agglomerates alone. Consideration of variable particle aspect ratios may be required to reflect the experimentally observed particle elongation. This is important both in the sieving process and in determining the likelihood of particle breakage and the resulting daughter distribution. It is also suggested that the population balance be coupled to a method for prediction of the mass distribution along the barrel from which compaction rates and residence times may be estimated. Finally, in order for optimised rates to be 're-used' across varying screw configurations the fitting methodology itself must be improved upon. In the future more advanced parameter optimisation could be carried out by fitting each compartmental PSD of the model against the experimental PSD at each associated barrel position, as carried out experimentally by Kumar et al. [86]. However, non-destructive extraction of a representative sample mid-barrel can be challenging. Alternatively, the model could be optimised against a large number of experiments with varying screw configuration (such as that carried out by Vercruysse et al. [167]), in order to isolate the individual contributions of each group of elements. Another option is to perform optimisation of element specific rate constants based on experimental studies such as that by Sayin et al. [147]. Here the role of each element type is assessed by only supplying liquid at the very end of the barrel, such that only a short section of the twin-screw is active and the compounded

effects of different elements in sequence are mitigated. However, it is likely that the role of specific screw elements is inherently coupled to the complete screw configuration and other processing conditions. It is more likely that a combination of these approaches will be required to build and refine future TSG models, gather element specific rate constants and move towards a truly modular TSG modelling framework.

Nevertheless, the stochastic method employed in the solution of this model, unlike traditional sectional methods, allows the dimensionality of the particle description to be readily extended to include many of the features that have been described above. These additional properties may then be incorporated into the particle transformations associated with TSG mechanisms.

Chapter 6

Numerical investigations of the model

In this chapter, the influence of key numerical factors of the simulation algorithm, presented in Chapter 4, is investigated. The investigation starts by looking at a number of particle weighting schemes for the inception of solid particles into the compartmental network. This is followed by an evaluation of the sensitivity of simulation performance measures to the statistical weights and weight transfer function associated with the nucleation process. The chapter concludes with an analysis of the general convergence properties of the complete stochastic weighting algorithm, in the context of the twin-screw model, followed by a number of recommendations regarding optimum numerical performance.

6.1 Simulation conditions

To ensure that the results of this analysis are relevant to typical model operating conditions (equipment operating conditions and rate constant values), all numerical tests are carried out using the equipment operating conditions and optimised model rate constants presented in Chapter 5, Tables 5.1 and 5.3, respectively . As in Chapter 4, all simulations were performed with $t_{\text{stop}} = 5\sum_{z\in\mathbb{Z}} \tau(z) \approx 40\text{s}$. The number of runs varied between tests and is stated for each results set. All test simulations were are carried out using a single core of an Intel® Sandy Bridge™ E5-2670 3.30GHz Processor with 4GB of RAM per core.

6.2 Quantification of errors

Mean values and confidence intervals for measured properties are constructed as described in Section 5.3. In cases where the statistical error of a distribution is to be measured, the mean confidence interval $\bar{c}$ is used. This is computed as

$$\bar{c} = \frac{1}{n_{\text{points}}} \sum_{j=1}^{n_{\text{points}}} c_j, \tag{6.1}$$

where n_{points} is the number of discrete points in the response's distribution of interest. For example, if $\bar{c}$ was the mean confidence interval of a sieved PSD, then n_{points} would simply be the number of sieve intervals.

When a high precision solution (HPS) is used as a reference point, the sum of squared errors of prediction (SSE) is used to represent the systematic error and is given by[1]

$$\text{SSE} = \sum_{j=1}^{n_{\text{points}}} (\eta_{\text{HPS},j} - \eta_j)^2. \tag{6.2}$$

All HPSs were generated from simulations with $N_{\max} = 65536$, $n_{\text{runs}} = 10$ and $w_{\text{drop}} = 0.001$.

[1] Note that (6.2) does not have any weighting factors, since all η of interest are of the same physical dimension and order of magnitude.

6.3 Inception sampling methods

In this section, we investigate various forms of the inception particle distribution $q_0^{\mathrm{SWA}}(d)$ and the resulting weight transfer functions $w_{\mathrm{incept}}(d)$ in the context of the SWA twin-screw granulation algorithm of Chapter 3 and 4. As a reminder to the reader, $q_0^{\mathrm{SWA}}(d)$ represents the frequency at which stochastic particles (representing solid primary particles with x given by (3.42)) of the form $(z, x_{\mathrm{incept}}(d), w_{\mathrm{incept}}(d))$, $x = (0, \pi d^3/6, 0, 0)$ are selected within an inception jump. In Chapter 4, it was demonstrated that the ability to weight incepted particles based on some key property, such as their diameter d, permitted an arbitrary $q_0^{\mathrm{SWA}}(d)$ to be used, provided that

$$w_{\mathrm{incept}}(d) = \left\langle w_{\mathrm{incept}} \right\rangle \frac{q_0(d)}{q_0^{\mathrm{SWA}}(d)}, \tag{6.3}$$

in order to recover the unweighted form of the PBE for this process (and hence effectively sample some physical inception particle size distribution $q_0(d)$).

In previous SWA studies [94, 96], the authors have employed

$$q_0^{\mathrm{SWA}}(d) = q_0(d), \;\; \left\langle w_{\mathrm{incept}} \right\rangle = 1, \;\; w_{\mathrm{incept}}(d) = 1. \tag{6.4}$$

It can be easily observed that the conditions (6.4) satisfy Equation (6.3). This inception scheme shall henceforth be referred to as the equi-weighted inception scheme for SWA (EWI-SWA).

EWI-SWA is attractive due to it ease of implementation, however, in some cases, it has been observed that significant reduction in computational cost can be attained using alternative forms of $q_0^{\mathrm{SWA}}(d)$, depending upon the ensemble property of interest.

As an example, consider the case where one is interested in measuring the mass distribution (as a function of d) within the steady state ensemble of the twin-screw granulation simulation. It is often the case that the real density distribution of particles $q_0(d)$ covers a $d \in \mathbb{D}_{\mathrm{incept}}$ range ($\mathbb{D}_{\mathrm{incept}} = [d_{\min}, d_{\max}]$) which is several orders of magnitude in size (such is the case of that presented for Lactose Impalpable in El Hagrasy et al. [46]). Given such a situation, one sees from Figure 6.1(a) (blue trace) that the particles which occur with the greatest frequency are those with d much smaller than $d_{\max}$. Consequently, most 'real' particles that are incepted into the physical system will have a volume (and thus mass) which is several orders of magnitude less than that held by particles with d

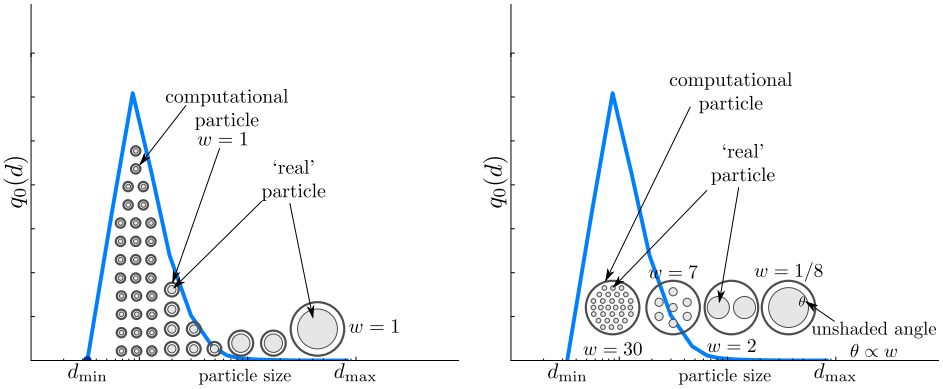

(a) equi-weighted inception scheme for SWA (EWI-SWA)

(b) variable weighted inception scheme for SWA (VWI-SWA)

Fig. 6.1 An illustrative example of the various sampling methods studied. In VWI-SWA, many small particles are grouped in a few computational particles, reducing the total number required to accurately sample 'mass-rich' regions of the distribution closer to d_{max}.

close to the upper limit of the inception range. Now, if one were to employ the EWI-SWA scheme in such a situation (i.e. $q_0^{\text{SWA}}(d) = q_0(d)$), then it follows that most of the stochastic particles that are incepted will also carry very little volume (and hence very low mass). As such, most particles will have very limited effect on the compartment mass distribution. However, occasionally stochastic particles with large d will be incepted into compartment $z = 1$, causing a temporary but significant change in the system mass distribution. This results in a high degree of stochastic noise within the measured product mass distribution. In order to mitigate this noise, it is required that the maximum number of computational particles N_{max} and/or n_{runs} be increased, both of which increase the computational cost of simulation.

From the thought experiment above, one sees that it would be advantageous to spread the incepted mass over the incepted computational particles in a more uniform manner, while still recovering $q_0(d)$. This is not only true of the inception process, but also the initialisation of the ensemble at $t = 0$. Furthermore, note that the transport processes also have the ability to induce a high degree of noise in the mass distribution when the compartment particle mass is poorly distributed across the ensemble of stochastic particles.

Methods to control the distribution of selected quantities, analogous to that described above, have been employed by Zhao and co-workers [178, 180, 181] and DeVille et al. [35] in the context of alternative particle models. Within

the numerical framework of Chapter 4, the size dependent particle weighting approach of Zhao and Zheng [180] is adapted to support the inception jump process (4.11) of the twin-screw model and also, to the initialisation of the ensemble. Specifically, the case where q_0^{SWA} is a uniform distribution over d with normalised form

$$q_0^{\mathrm{SWA}}(d) = (d_{\max} - d_{\min})^{-1}, \tag{6.5}$$

is employed and its numerical properties investigated within this chapter. Here, $d_{\max}$ and $d_{\min}$ are the maximum and minimum particle diameters of the distribution $q_0(d)$, respectively.

It follows from (6.3) that

$$w_{\mathrm{incept}}(d) = \left\langle w_{\mathrm{incept}} \right\rangle (d_{\max} - d_{\min}) q_0(d). \tag{6.6}$$

The use of (6.5) and (6.6) for inception will be referred to as the variable weighted inception scheme for SWA (VWI-SWA). The use of VWI-SWA results in a stochastic particle distribution analogous to that illustrated in Figure 6.1(b). Numerical tests were carried out to assess the performance of the EWI-SWA and VWI-SWA inception algorithms described above. To ensure that the rates of each process were matched between compared sets of simulations at $t = 0$, the values of w_{drop} were modified in the EWI-SWA case. For VWI-SWA, $\left\langle w_{\mathrm{drop}} \right\rangle$ was set to 16.38 in all simulations. This value ensured that the sample volumes of the EWI-SWA and VWI-SWA simulations were approximately the same, with $\left\langle w_{\mathrm{incept}} \right\rangle = 1$ for EWI-SWA.

The resulting sieved exit mass fraction distributions using both EWI-SWA and VWI-SWA with $N_{\max} = 8192$ are presented in Figure 6.2. It is noted that, for the EWI-SWA scheme, most of the computational feed particles have been utilised to form the lower end of the distribution between 10-100μm. As a result, sampling of the primary particle distribution is much poorer for larger particle diameters (where most of the ensemble mass resides). The error in these larger sieve classes for the EWI-SWA scheme has carried over into the steady state solution. By contrast, the VWI-SWA scheme has sampled the initial distribution with much higher precision in the larger sieve classes, resulting in a steady state distribution with relatively small confidence intervals across the complete diameter range. Since both simulations operated with the same bounds on the number of computational particles permitted, it is expected that both EWI and VWI-SWA schemes should result in CPU times which are if the same order of

magnitude. This is confirmed by the inset CPU plot in Figure 6.2, where the weighted inception algorithm has showed a similar but slightly reduced CPU time over the EWI-SWA scheme. The variations in CPU time likely reflect the interaction between the particle selection procedure of the nucleation algorithm and the ensemble weight distribution. This interaction may change the rate at which particles are fully depleted (deleted from the ensemble) by the mechanism, altering the equilibrium computational particle count and, hence, the CPU time.

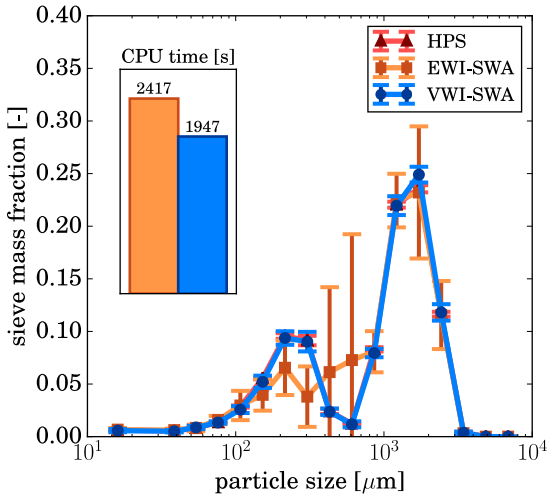

Fig. 6.2 A comparison of the product mass fraction distributions (z=3) and CPU times using the VWI-SWA and EWI-SWA algorithms with $N_{\max}$=8192. A high precision solution using VWI-SWA is included but sits directly behind the blue trace.

The scaling performance of each inception (and initialisation) algorithm was assessed by running a series of simulations with varying $N_{\max}$ (and therefore the minimum number of computational particles, as $N_{\min} = 3N_{\max}/8$). Simulations were run with $N_{\max}$=1024 and increased by a factor of two to a final $N_{\max}$=65536. Simulations using the EWI-SWA scheme proved to be numerically unstable for $N_{\max} \in \{1024, 2048\}$, and thus results for these operating points are not reported here. The resulting set of mean confidence interval half-widths $\bar{c}$ across the resulting sieve exit mass fraction distribution and their associated CPU times are presented in Figure 6.3. Here, $1/\bar{c}$ is used to quantify the precision of each response.

It is clear from Figure 6.3 that the VWI-SWA scheme offers a much higher precision solution than the equivalent EWI-SWA (same CPU time). Specifically, the VWI-SWA scheme can be seen to yield solutions in CPU times almost two orders of magnitude lower than the EWI-SWA for the same level of precision.

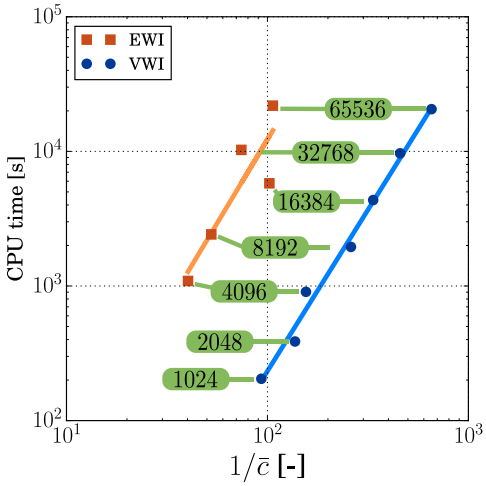

Fig. 6.3 A comparison of the total CPU time vs. associated inverse average confidence interval half-width in the sieved exit mass fraction distribution for 40s of simulation with $n_{\text{runs}} = 10$. The number of computational particles (attached green blocks) is varied to yield different CPU times and $1/\bar{c}$ values.

6.4 Immersion nucleation parameters

As previously described in Chapter 4, immersion nucleation is the combination of droplet addition and nucleation processes into a unified jump process. In this section, the importance of the selection of the key parameter w_{drop}, the selection of ensemble particles x_i and simplification of the iteration process within the nucleation jump process (4.27) for the twin-screw granulation test case are investigated.

Selection of the droplet weight

As described in Chapter 4, the statistical weight of incepted droplet particles w_{drop} is a free parameter within the context of the immersion nucleation jump process. Furthermore, one observes from Equation (4.26) that the rate of nucleation jumps in compartment $z = 1$ has the characteristic

$$R_{\text{drop}}^{\text{SWA}}(1,t) \propto (v_{\text{drop}} w_{\text{drop}})^{-1}, \tag{6.7}$$

where v_{drop} is the average volume of a droplet particle (droplets are considered to be mono-disperse within the context of this thesis).

In previous SWA efforts that modelled high shear batch granulation [94, 95], alternative droplet particle inception jump processes with jump rates given by equations of the form (4.26) have been implemented with $w_{\text{drop}} = 1$. In these examples, the value of v_{drop} was very small (on the order of 10^{-13}m^3) to reflect the operation of the equipment being modelled. As a result, the rate of this process was significant (relative to the total jump rate) allowing it to be sampled with a high degree of accuracy.

However, in the case of twin-screw granulation, operating values of v_{drop} can be much larger (on the order of 10^{-8}m^3). Hence, if $w_{\text{drop}} = 1$, then the immersion nucleation jump rate can be exceptionally low relative to the total jump rate, resulting in poor sampling of this jump process. In addition to this, it is noted that a single immersion nucleation jump can have a significant impact on the particle mass distribution within the ensemble (particularly when w_{drop} is on the order of $\langle w_{\text{incept}} \rangle$), and hence, poor immersion nucleation sampling results in a high degree of stochastic noise in the product mass distribution. This ultimately places a limit on the size of v_{drop} that can be modelled with an acceptable degree of error (with w_{drop}=1). Again, like the case of poor solid particle inception sampling, this noise can be mitigated by increasing N_{max} and n_{runs} at an additional computational cost. In this thesis, the need to increase N_{max} and/or n_{runs} is avoided by dynamically selecting w_{drop} according to the operating conditions to be modelled. It will be demonstrated that, in doing so, one can ensure the effective sampling of this important jump process within the context of the twin-screw granulation model.

Simplification of the jump

As mentioned in Chapter 4, Section 4.3.5, the nucleation particle addition jump (4.27) has the drawback of potentially creating more than a single partially formed nucleus in the jump products (when $w_{\text{nuc}} < w_i$). This additional, partially formed nuclei must also then be separately and repeatedly passed through jump (4.27) until the condition (4.40) is satisfied. This is undesirable as these additional nuclei have the potential to create yet more nuclei, so on and so forth, before stopping condition (4.40) is satisfied. Hence, it is possible that this process may become computationally taxing and flood the ensemble with particles which are physically very similar, and possesses very low statistical weights. To avoid these issues, note that, in the context of the twin-screw model, ensemble particles x_i that are able to attached to the partially formed (i.e. those for which

$K_{\text{nuc}}(x_{\text{nuc}}, x_i) \neq 0$) are generally much smaller in volume than the corresponding nucleus x_{nuc}. Hence, the addition of a single x_i to x_{nuc} has relatively little effect on the state of x_{nuc} i.e.

$$T_{\text{nuc}}(x_{\text{nuc}}, x_i) \approx x_{\text{nuc}}. \tag{6.8}$$

It is also noted that the statistical weight of the first partially formed nucleus (in the case where two nuclei are formed) is $\min(w_{\text{nuc}}, w_i) = w_i$, which is generally much greater than the weight of the secondary nucleus ($w_{\text{nuc}} - w_i$). As such, the product particles may be combined into a single representative particle using a weighted average of the particles of $(T_{\text{nuc}}(x_{\text{nuc}}, x_i), w_i)$, $(x_{\text{nuc}}, \min(w_{\text{nuc}} - w_i))$ with the form:

$$(w_{\text{nuc}}^{-1}\left[w_i T_{\text{nuc}}(x_{\text{nuc}}, x_i) + (w_{\text{nuc}} - w_i)x_{\text{nuc}}\right], w_{\text{nuc}}). \tag{6.9}$$

It was observed that, for the systems modelled in Chapter 5 and this chapter, this simplification had no discernible effect on the model solution but offered modest reduction in simulation times (5-10%) and code complexity, therefore this simplification is employed in all simulations within this study. An illustrative example of the resulting immersion nucleation jump process if presented in Figure 6.4.

Selection of ensemble particles

As alluded to in Chapter 4, the selection of computational particles (x_i, w_i) for addition to partially formed nuclei by way of jump (4.27) can be simplified based on the model nucleation kernel K_{nuc} employed. Combining Equations (3.14) and (4.34), one sees that the majorant form of the nucleation kernel for the twin-screw model is

$$\tilde{K}_{\text{nuc}}(x_{\text{nuc}}, w_{\text{nuc}}, x_i, w_i, z, t) = k_{\text{nuc}}(z)v(x_i)(w_{\text{nuc}} + w_i)\mathbb{1}_{\{x|v(x_i)<v_{\text{drop}}\}}(x_i). \tag{6.10}$$

Since only a single nuclei particle is considered at a time, the total rate of this process is

$$\sum_{i=1}^{N(z,t)} \tilde{K}_{\text{nuc}}(x_{\text{nuc}}, w_{\text{nuc}}, x_i, w_i, z, t) = \sum_{i=1}^{N(z,t)} k_{\text{nuc}}(z) v(x_i)(w_{\text{nuc}} + w_i) \mathbb{1}_{\{x|v(x_i)<v_{\text{drop}}\}}(x_i) \tag{6.11}$$

$$= k_{\text{nuc}}(z)(z,t) w_{\text{nuc}} \sum_{i=1}^{N(z,t)} v(x_i) \mathbb{1}_{\{x|v(x_i)<v_{\text{drop}}\}}(x_i) + k_{\text{nuc}}(z) \sum_{i=1}^{N(z,t)} v(x_i) w_i \mathbb{1}_{\{x|v(x_i)<v_{\text{drop}}\}}(x_i). \tag{6.12}$$

Thus, particle (x_i, w_i) is selected to take part in the jump (4.27) based on the selection property $v(x_i)$ with probability

$$\mathbb{P}_{v(x_i)} = \frac{w_{\text{nuc}} \sum_{i=1}^{N(z,t)} v(x_i) \mathbb{1}_{\{x|v(x_i)<v_{\text{drop}}\}}(x_i)}{w_{\text{nuc}} \sum_{i=1}^{N(z,t)} v(x_i) \mathbb{1}_{\{x|v(x_i)<v_{\text{drop}}\}}(x_i) + \sum_{i=1}^{N(z,t)} v(x_i) w_i \mathbb{1}_{\{x|v(x_i)<v_{\text{drop}}\}}(x_i)}. \tag{6.13}$$

It follows that particle (x_i, w_i) is selected to take part in the jump (4.27) based on the selection property $v(x_i)w_i$ with probability

$$\mathbb{P}_{v(x_i)w_i} = 1 - \mathbb{P}_{v(x_i)}. \tag{6.14}$$

Using a binary tree to store properties $v(x_i)\mathbb{1}_{\{x|v(x_i)<v_{\text{drop}}\}}(x_i)$ and $v(x_i)w_i\mathbb{1}_{\{x|v(x_i)<v_{\text{drop}}\}}(x_i)$ for each computational particle allows for rapid evaluation of the summations in (6.13) and hence the evaluation of $\mathbb{P}_{v(x_i)}$ and the selection of particle x_i with the desired probability measure.

The complete nucleation algorithm (including the particle selection procedure described above) is described in Algorithm 1 on page 98.

Nucleation performance

To assess the affect of w_{drop} on the performance of twin-screw simulations, several simulations were carried out using the VWI-SWA algorithm and $N_{\max} = 1024$ for various values of w_{drop} in the range 5×10^{-5} - 5×10^{-2}. All errors were constructed from the sieved mass fraction distribution in the final reactor ($z = 3$).

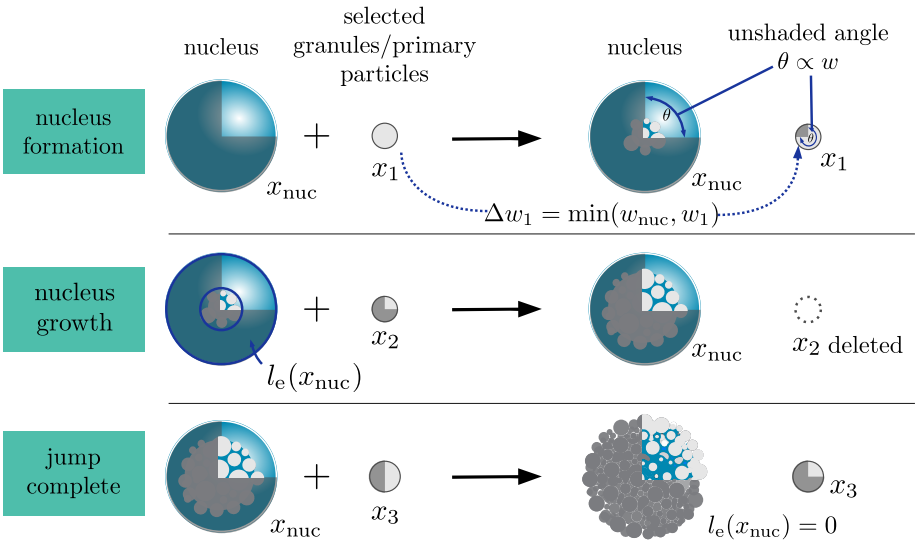

Fig. 6.4 An illustration of the SWA immersion nucleation scheme. Each particle represents a single computational particle. The angle of the unshaded region of each particle is constructed such that it is proportional to the associated statistical weight of the particle. Each pathway corresponds, respectively, to the first, intermediate (with particle removal) and final iteration of the particle selection loop of Algorithm 1 (steps 3-12). Note that the reduction in weight of the primary particle (i.e. a reduction in its unshaded area) is generally equal to the weight (unshaded area) of the nucleus particle. This weight reduction coincides with the nucleus acquiring a degree of mass, to account for the mass loss from the primary particle (in the form of a reduction in its statistical weight). Particles with a resulting $w = 0$ are deleted from the ensemble. Further note that the immersion processes ceases when $l_e(x_{\text{nuc}}) = 0$.

From Figure 6.5(a), it is noted that the mean confidence interval half-width $\bar{c}$ varies relatively smoothly with w_{drop} and $\bar{c}$ exhibits an increase towards the limits of the w_{drop} range investigated. The picture painted by the SSE in the same figure is less clear towards low w_{drop}, however, from the PSDs in Figure 6.5(b) we see that all simulation solutions lie in close proximity to the HPS, regardless of w_{drop} and thus the SSE values are subject to a high degree of noise in this operating range. The increase in $\bar{c}$ and SSE towards the upper ranges of the tested w_{drop} is indicative of the poor sampling of the nucleation jump, as discussed in Section 6.4. Towards the lower range of w_{drop}, the nucleation jump rate is very high and the absolute liquid mass carried by the stochastic nuclei particles at the start of the jump is relatively low. Since the amount of solid particles that interact with the nuclei is roughly proportional to the absolute liquid mass of the stochastic nuclei particle, the number of solid particles acted on by each nuclei jump becomes much lower. Hence, greater fluctuations in the primary particle

mode at low w_{drop} are expected, as observed in the left-most peak in the PSD of Figure 6.5(b).

As expected, in Figure 6.5(c) it is observed that, in general, the CPU time is reduced with increasing w_{drop} as the total jump rate in reduced. This trend diminishes towards large w_{drop} as nucleation ceases to be the dominant jump process. For $w_{\text{drop}} > 0.007$, coagulation becomes the dominant jump process (in

Algorithm 1: The SWA immersion nucleation algorithm.

1 Set the droplet volume v_{drop} and initial nucleus particle state $(x_{\text{nuc}}, w_{\text{nuc}})$ to that of a droplet particle:

$$\begin{aligned} v_{\text{drop}} &\leftarrow \pi d_{\text{drop}}^3/6, \\ x_{\text{nuc}} &\leftarrow x_{\text{drop}} = (0, v_{\text{drop}}, 0, 0), \\ w_{\text{nuc}} &\leftarrow w_{\text{drop}}. \end{aligned}$$

2 **while** $\underline{l_{\text{e}}(x_{\text{nuc}}) > 0}$ **do**
3 Choose particle selection procedure according to (6.13) and (6.14).
4 Choose particle x_i from compartment z according to selection procedure.
5 Generate a uniform random number $\mathcal{U}(0,1)$.
if $\underline{\mathcal{U} < \max(w_i, w_{\text{nuc}})/(w_i + w_{\text{nuc}})}$ **then**
6 Set $\gamma_{nuc} \leftarrow \min(w_i, w_{\text{nuc}})$.
7 Create particle $(z, T_{\text{nuc}}(x_{\text{nuc}}, x_i), \gamma_{\text{nuc}})$.
8 Set $w_i \leftarrow w_i - \gamma_{nuc}$.
9 Set $w_{\text{nuc}} \leftarrow w_{\text{nuc}} - \gamma_{\text{nuc}}$.
if $\underline{w_i = 0}$ **then**
10 Remove particle x_i from the ensemble
if $\underline{w_{\text{nuc}} > 0}$ **then**
11 Product nuclei are to be combined

$$\begin{aligned} x_{\text{nuc}} &\leftarrow (w_{\text{nuc}}^{-1}(w_i T_{\text{nuc}}(x_{\text{nuc}}, x_i) + (w_{\text{nuc}} - w_i)x_{\text{nuc}}, w_{\text{nuc}}) \\ w_{\text{nuc}} &\leftarrow w_{\text{nuc}} + \gamma_{nuc} \end{aligned}$$

else
Jump is fictitious. Go to Step 3

12 Add newly formed nucleus $(x_{\text{nuc}}, w_{\text{nuc}})$ into compartment z.
13 Move forward in time and select next jump event.

terms of CPU-time) and so the computation time becomes independent of w_{drop}. In Figure 6.5(d), the combination of error and CPU time data for various values of w_{drop} shows that there exists a favourable range of w_{drop} approximately between 10^{-2} - 5×10^{-4} where both the error and computation time are minimised.

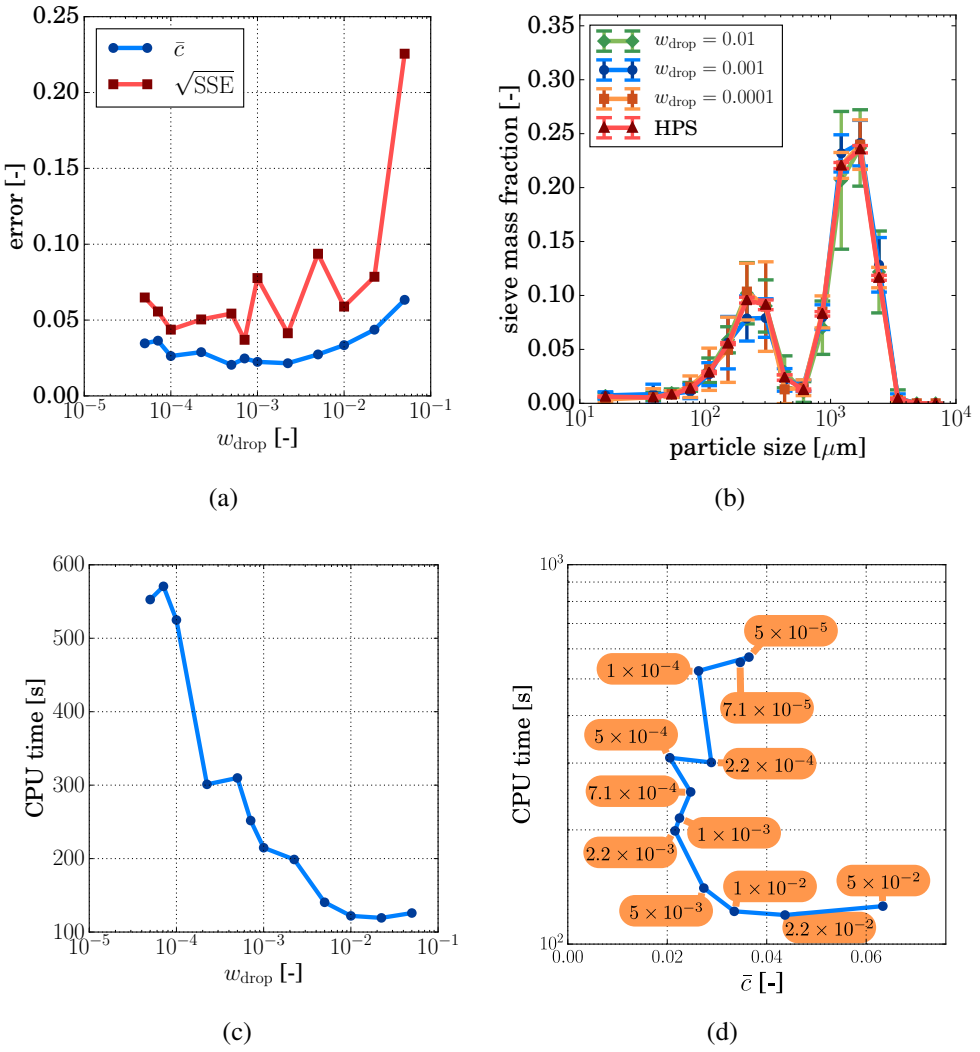

Fig. 6.5 The effect of varying w_{drop} on simulation performance. All results correspond to the steady state sieved mass fraction distribution in $z = 3$. In (d) the value of w_{drop} corresponding to each point is indicated within the attached blocks.

6.5 Convergence properties

It is useful to consider the convergence properties of the complete stochastic algorithm for the twin-screw test case. This is done by assessing how the systematic and statistical error in the final mass distribution depends on N_{max} and n_{runs}. All convergence tests are carried out with the VWI-SWA algorithm and $w_{\text{drop}} = 0.001$.

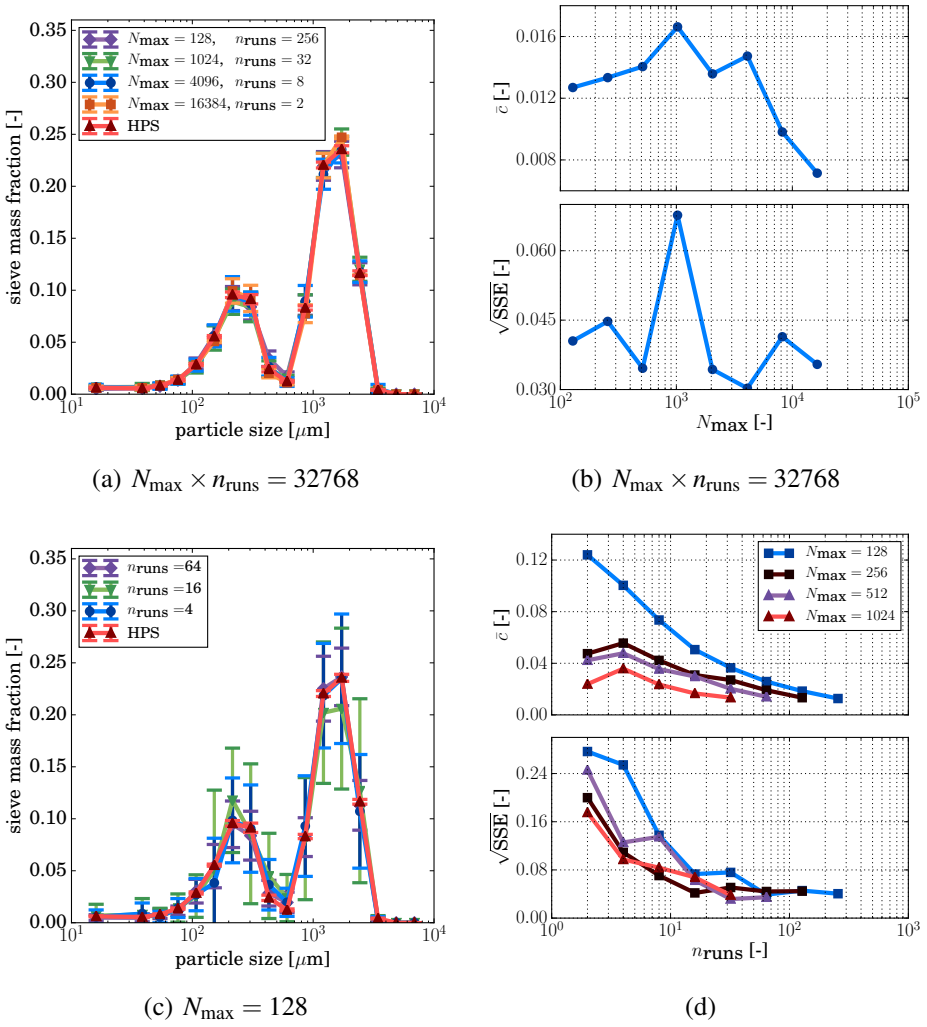

(a) $N_{\text{max}} \times n_{\text{runs}} = 32768$

(b) $N_{\text{max}} \times n_{\text{runs}} = 32768$

(c) $N_{\text{max}} = 128$

(d)

Fig. 6.6 Convergence properties of the twin-screw SWA framework using VWI-SWA.

Figures 6.6(a) and 6.6(b) show the dependence of the final mass distribution and its associated error on N_{max} for an approximately fixed computational budget by holding $N_{\text{max}} \times n_{\text{runs}}$ constant at 32768. In this region of operating space, there is no observed correlation between N_{max} and the statistical or systematic

error measures and that all measured mass distributions lie on top of the HPS. Both of these observations indicate that the simulation algorithm is extremely robust against changes in N_{max}, provided that the n_{runs} is scaled appropriately. Lower values of N_{max} could not be explored as the algorithm became numerically unstable for $N_{\text{max}} < 128$. These instabilities are induced by the fact that the incepted nuclei particles can no longer gather sufficient solid mass to complete the nucleation jump process.

Thus, in order to access regions of operating space where the systematic and statistical error is more significant, it is required that lower values of $N_{\text{max}} \times n_{\text{runs}}$ are used. Figure 6.6(c) shows the variation in the final mass distribution and the associated confidence intervals with fixed N_{max}=128 for varying values of n_{runs}. This figure shows that $N_{\text{max}} \times n_{\text{runs}}$ can be lowered to 8192 before the mass distribution begins to significantly deviate from the HPS. It is also clear that, even with n_{runs}=4, the solution still lies in close proximity to the HPS, though the confidence intervals have dramatically increased in size, as expected.

This region of operating space is further explored in Figure 6.6(d), which shows how the statistical and systematic error varies with n_{runs} for low values of N_{max}. Here, if ones compares simulations of equal $N_{\text{max}} \times n_{\text{runs}}$ (i.e. comparable CPU times) then it is observed that, in general, there is no clear dependence between N_{max} and statistical or systematic error for low values of N_{max}. From this analysis we may conclude that, for a twin-screw test case investigated, if a desired level of error in the final mass distribution is desired (either systematic or statistical), then there is no significant benefit of increasing N_{max} provided that N_{max} exceeds the value required for computational stability (128 in this case).

6.6 Chapter conclusions

In this Chapter, a number of numerical parameters within the weighted population balance framework for TSG in Chapter 5 were investigated. A variable weighting particle inception and initialisation algorithm was constructed to aid the efficient sampling of wide primary particle size distributions. This inception algorithm was shown to deliver performance increases of between one and two orders of magnitude over the traditional equi-weighted inception scheme. The numerical properties of the new nucleation jump process were explored and its implementation discussed. It was observed that there exists a specific range of nuclei statistical weight that minimises both the error in the final mass fraction

distribution and the computational cost of simulation. The convergence properties of the complete algorithm were assessed using the twin-screw test case and it was shown that the algorithm is extremely robust against changes in the number of computational particles used.

Chapter 7

Advancement of the model

In this chapter, some of the areas for model improvement identified in Chapter 5 are addressed. This includes the addition of new mechanisms for primary particle layering, particle breakage and a method for estimating compartment residence times for different screw configurations. A number of changes are made to the numerical treatment of the primary particle species that enables the realisation of the new layering mechanism. The mechanism set is validated using the new numerical framework for a range of different screw configurations for which experimental data exists.

7.1 Background

A number of potential sources of discrepancy between model and experiment were proposed in Chapter 5. The most important of these were: the absence of a layering mechanisms (distinct from general particle collision and coagulation), the simplicity of the breakage kernel employed and, finally, the assumption of equal residence times in all compartments.

Layering is the process by which primary particles adhere to the surface of agglomerate particles, provided that there is a critical amount of binder available to facilitate a bond between the two phases. From a numerical perspective, this requires an explicit distinction between primary particles and all other particles in the granular system. This could be implemented by some indicator function that communicates whether a computational particle represents a primary particle or not, based on some criterion. This approach permits one to keep the primary particles in the same ensemble as the aggregate phase, making it attractive from an implementation perspective. However, this approach has a number of drawbacks, first of which is the continual need to evaluate the indicator function in order to compute the jump rates and select particles to take part in jump events. The second and most significant drawback of this approach is the extremely high rate of this process, which is computationally expensive, due to the need to recompute the jump rates of all processes after each layering event. Preliminary simulations of the layering process using a number of weight transfer functions showed that, due to the physical difference in concentration of small primary particles (relative to those simulated in Chapter 5), the jump rates required to move an appreciable amount of mass between the primary particle phase and the aggregate phase were in excess of 10^6 s^{-1} (even with VWI-SWA), which is computationally infeasible.

An alternative method of separating the primary and agglomerate phases is the use of distinct population balances for each of the two phases. Barrasso and Ramachandran [12] successfully used this approach to incorporate a primary particle layering mechanism into a twin-screw model which was solved using the sectional method. The use of two population balances permits each phase to be simulated using different numerical methods, which can then be coupled in an appropriate manner. This avoids the need for repeated indicator function evaluations and, with suitable choice of numerical method for the primary particle phase, has the potential to avoid the large computational expense of species interaction. The implementation of such a phase separation approach will be investigated within this chapter.

To aid the construction of a more complex aggregate breakage model, a number of experimental studies may be leveraged. Experimental investigations into particle breakage in twin-screw devices [47, 86, 106, 138, 167] have highlighted the role of screw element geometry on the breakage dynamics along the barrel. For example, several studies [106, 138] have shown that the large agglomerates in conveying elements undergo size reduction through cutting or edge chipping, where small fragments are continually taken from the edge of the agglomerates. The particle size distribution transformation induced by DME in Pradhan et al. [138] suggests that breakage in these elements occurs through a combination of crushing and chipping [138]. This would indicate that the fragment volume distribution should depend closely on the type of screw element being represented by a particular model compartment. Furthermore, this would also seem to indicate that particle breakage frequency g_{break} should not only vary between element types for a fixed particle type, but also that the relationship between g_{break} and the particle volume (or some other derived property) should also be element specific.

Moving onto the issue of residence time prediction, it is noted that, because of the combinatorial nature of the twin-screw operating space, it is desirable to develop a process model wherein the screw sections can be treated in a modular manner. Such constructions may permit the performance of new screw configurations to be quickly assessed, without the usage of excipient or API, or the need to set up the device etc. This requires a method of assigning residence times that can be readily applied to new screw configurations. In order to create a framework for the prediction of residence times, information from a number of existing twin-screw material flow studies must be considered. A number of experimental studies have examined the mass distribution over the twin-screw system, through the use of Positron Emission Particle Tracking (PEPT) [97, 151]. Recently, it has also been proposed [63] that barrel fill level be used as way to define the design space in TSG. This has been motivated by the observation that very similar PSDs can be obtained for very different screw speed and mass feed rates, provided the fill level is the same across these experiments. From a screw element perspective, it is noted that kneading elements will generally be completely or almost completely filled with material at steady state. This is because the kneading element geometry affords low conveying capacity, which allows for the accumulation of material. In contrast, conveying elements generally have a much lower fill level that is dependent on the operating speed of the screw [151] and the feed material [145]. This non-uniformity in the mass distribution ultimately leads to varying residence times across different sections of the screw, which must be captured within a

model, if model rates are to be applied to various screw configurations. Attempts have been made to predict such mass distributions in the context of twin-screw extrusion systems [45]. Though the resulting models showed good performance, the flowing material consisted of a polymer melt, which has quite different flow characteristics compared to the partially wet powder mass in the TSG system. This limits its applicability to TSG. In this chapter, a novel method for assigning these residence times is presented and applied to a number of test systems.

To summarise the above, **the main aims of this chapter are:**

1. Improve the stochastic TSG model presented and explored in previous chapters, based on the areas identified for improvement.
2. Construct a modelling framework that allows for the compartmental representation of complex screw configurations by way of a residence time model.
3. Validate the new model framework using existing experimental data for a variety of screw configurations.

The remainder of this chapter is structured as follows: firstly, the new TSG PBM is presented, including details of the new and augmented mechanisms. This is followed by the presentation of a methodology for estimating compartment residence times for screw configurations consisting of arbitrary combinations of kneading and conveying elements. The associated changes to the stochastic weighted particle method used to simulate the PBM are then presented in detail in Section 7.3. The experimental systems used for the optimisation step and the simulation conditions are described in Section 7.4. The chapter finishes with a discussion of the model results in Section 7.5 and concluding remarks in Section 7.6.

7.2 Twin-screw population balance model

7.2.1 Overview of changes to the model

As an overview, the following changes to the twin-screw model described in Chapter 3 have been made:

1. Primary particles have been modelled as a separate phase from aggregate particles. For simplicity, the primary particle phase is treated as monodisperse with diameter 27.3μm[1].
2. A primary particle layering mechanism has been formulated to promote the consumption of fines upon contact with surface wet agglomerates. This is distinct from the particle collision and coagulation mechanisms of Chapter 3.
3. The droplet-nucleation mechanisms have been unified within the model (these mechanisms were formally unified only in the context of the numerical method) due to the degree of simplifications that become available with the new primary particle representation.
4. A size dependent collision kernel is used in place of the simple size-independent kernel of Chapter 3. The new kernel is for both the aggregate-aggregate collisions and the aggregate-primary layering processes.
5. The breakage mechanism of Chapter 3 has been replaced with a more complex model and the daughter distribution parameters have been selected to reflect the different breakage modes in kneading and conveying elements.
6. The consolidation mechanism has been removed from the particle collision and coagulation mechanisms and recast as a separate, continuous process.
7. The liquid penetration mechanism has been changed from a distinct continuous processes to a processes that only occurs as part of the layering and coagulation mechanisms.

The new mechanism set is depicted in Figure 7.1.

7.2.2 Particle type-space and population balance equation

In the new TSG model, particles are described using the same type-space $\mathbb{X}$ as Chapter 3 and the derived properties such as volume, porosity etc. remain unchanged. 'Free' primary particles (i.e. those that are not part of an agglomerate) are comprised purely of original solid. Since the width of the primary particle size distributions that is to be used for validation is significantly smaller than that of the aggregate distribution of interest (and the span of that primary particle

[1]Note: this value was taken from the d_{50} of the full primary PSD provided by [Meggle] and is slightly lower than the d_{50} of 35μm reported for the experiments of Vercruysse et al. [167], used for model validation later in this chapter.

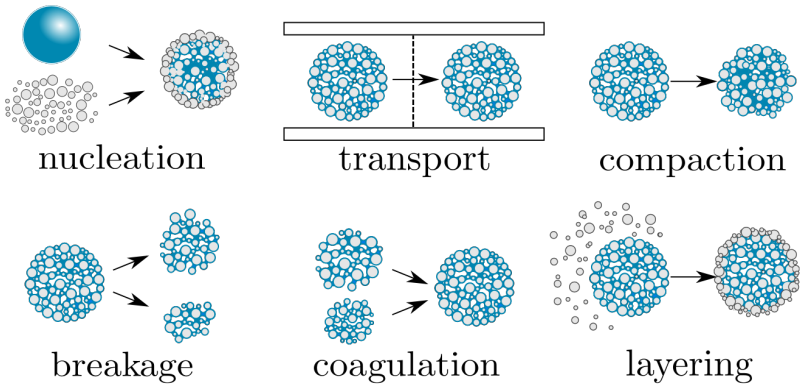

Fig. 7.1 Twin-screw particle mechanisms

PSD in Chapter 5-6) these particles are modelled as a mono-disperse phase with representative particle diameter d_{pp} and volume v_{pp}. Furthermore, since the set of all primary particles $\mathbb{X}_{\text{pp}} \subset \mathbb{X}$ is only permitted to occupy a very limited region of the type-space ($\mathbb{X}_{\text{pp}} = \{x_{\text{pp}}\}, x_{\text{pp}} = (v_{\text{pp}}, 0, 0, 0)$) it is sufficient to characterise this phase by the number concentration of primary particles $c_{\text{pp}} \in \mathbb{R}^+$ or, equivalently, the number of primary particles $N_{\text{pp}} \in \mathbb{R}^+$ that exist within a given volume of the system to be modelled. The aggregate type space may then be defined as $\mathbb{X}_{\text{agg}} = \mathbb{X} \setminus \mathbb{X}_{\text{pp}}$.

Elements of $\mathbb{X}_{\text{agg}}$ take positions in a bounded domain of compartments. Similarly, each compartment has an associated number of primary particles N_{pp}. Each compartment is again denoted by its index $z \in \mathbb{L}$. Particles (both primaries and aggregates) are permitted to move between compartments according to the connections defined by the compartmentalisation of the system (discussed further in Section 7.2.5). Only particles within the same compartment are permitted to interact with each other.

The Linear Process Deferment Algorithm [133] is again utilised to defer the applications of linear process operators that are particularly computationally intensive. In this chapter, this includes layering of primary particles onto the surface of large aggregates and aggregate consolidation.

The new population balance model is again to be solved using the stochastic particle method, however, the division of the primary and aggregate phases results in a slight change in the domain of certain operators. In the context of this chapter, let

1. $\lambda(z,t,\mathrm{d}x)$ be a concentration measure on $\mathbb{X}_{\text{agg}}$ at time t in compartment z,

2. addition and subtraction on $\mathbb{X}$ correspond to particle coagulation and breakage, respectively,
3. $\varphi(z,x) : \mathbb{X} \mapsto \mathbb{R}$ be a suitable test function which is smooth with compact support,
4. $D_t : (\mathbb{L}, \mathbb{X}_{\text{agg}}, \mathbb{R}^+) \mapsto \mathbb{X}_{\text{agg}}$ be the aggregate deferment function that carries out the deferred aggregate processes. For any particle x, compartment z and primary particle concentration c_{pp}, $D_t(z,x,c_{\text{pp}})$ is distributed as the value at time t of the Markov chain defined by the undeferred jump processes and their associated rates.

The weak form of the aggregate PBE to be solved is then

$$\begin{aligned}
\frac{\mathrm{d}}{\mathrm{d}t}\int_{x\in\mathbb{X}_{\text{agg}}} \varphi(z,x)\lambda(z,t,\mathrm{d}x) = \qquad & (7.1)\\
&\int_{x\in\mathbb{X}_{\text{agg}}} \varphi(z,x) I_{\text{nuc}}(z,t,c_{\text{pp}},\mathrm{d}x)\\
&+\frac{1}{2}\int_{x,y,\xi,\zeta\in\mathbb{X}_{\text{agg}}} [\varphi(z,\xi+\zeta)-\varphi(z,x)-\varphi(z,y)]K_{\text{coag}}(z,\xi,\zeta)\\
&\qquad \mathbb{P}(D_t(z,x,c_{\text{pp}})=\mathrm{d}\xi)\mathbb{P}(D_t(z,y,c_{\text{pp}})=\mathrm{d}\zeta)\\
&\qquad \lambda(z,t,\mathrm{d}x)\lambda(z,t,\mathrm{d}y)\\
&+\frac{1}{2}\int_{x,y,\xi\in\mathbb{X}_{\text{agg}}} [\varphi(z,\xi)+\varphi(z,\xi-y)-\varphi(z,x)]F(z,\xi,\mathrm{d}y)\\
&\qquad \mathbb{P}(D_t(z,x,c_{\text{pp}})=\mathrm{d}\xi)\lambda(z,t,\mathrm{d}x)\\
&+\int_{x,\xi\in\mathbb{X}_{\text{agg}}} \varphi(z,\xi) r_{\text{inflow}}(z)\mathbb{P}(D_t(z-1,x,c_{\text{pp}})=\mathrm{d}\xi)\lambda(z-1,t,\mathrm{d}x)\\
&-\int_{x,\xi\in\mathbb{X}_{\text{agg}}} \varphi(z,\xi)\frac{1}{\tau(z)}\mathbb{P}(D_t(z,x,c_{\text{pp}})=\mathrm{d}\xi)\lambda(z,t,\mathrm{d}x) \quad \forall z\in\mathbb{L},
\end{aligned}$$

and corresponding primary particle PBE can be written as

$$\frac{\mathrm{d}}{\mathrm{d}t}c_{\text{pp}}(z,t) = I_{\text{trans,pp}}(z,t) - I_{\text{nuc,pp}}(z,t) - \int_{x\in\mathbb{X}_{\text{agg}}} r_{\text{layer}}(z,t,x,c_{\text{pp}})\lambda(z,t,\mathrm{d}x). \tag{7.2}$$

Each integral on the RHS of Equation (7.1) represents an aggregate particle processes within the new model. In order of appearance, these are: nucleation, collision (which may lead to coagulation), breakage, inflow and outflow (illustrated in Figure 7.1). In the primary particle PBE (Equation (7.2)), the terms, in

order of their appearance on the RHS, represent transport processes, nucleation and layering (onto aggregates). Each of the terms in Equation (7.1) and (7.2) will be fully defined for the new TSG model in the section to follow. Details of the implementation of these mechanisms including the jump transforms are presented later in Section 7.3.

7.2.3 Aggregate particle processes

Nucleation

The first term in Equation (7.1) represents the nucleation (formation) of aggregate particles. The nucleation process involves the addition of a liquid droplet to the first compartment and rapid addition of primary particles to the droplet, producing a nucleus particle with form $x_{\text{nuc}} \in \mathbb{X}_{\text{agg}}$.

In Chapter 3, the nucleation process was the rapid and sequential addition of particles (both primaries and aggregates) to an existing droplet. In this chapter, nucleation is recast as the formation of a nucleus particle with form $x_{\text{nuc}} \in \mathbb{X}_{\text{agg}}$ through the rapid and simultaneous addition of a number of primary particles to a droplet particle, at the exact point of droplet inception. Hence, this is something of a unification of the liquid addition and the existing nucleation mechanism, with the caveat that only primaries may now join the droplets. The unified nucleation process is still based on the immersion nucleation phenomenon. In the new nucleation mechanism, a nucleus incepted into compartment z takes the form

$$x_{\text{nuc}}(z, c_{\text{pp}}, t) = \begin{cases} \left(\dfrac{v_{\text{drop}}}{\phi_{\max}}, 0, v_{\text{drop}}, \dfrac{v_{\text{drop}}}{s^*} \right), & \text{if } \dfrac{v_{\text{drop}}}{\phi_{\max}} \leq c_{\text{pp}}(z) V_{\text{real}}(z) v_{\text{pp}}, \\ \left(c_{\text{pp}}(z) V_{\text{real}}(z) v_{\text{pp}},\ v_{\text{drop}} - c_{\text{pp}}(z) V_{\text{real}}(z) v_{\text{pp}} \phi_{\max}, \right. & \\ \quad \left. c_{\text{pp}}(z) V_{\text{real}}(z) v_{\text{pp}} \phi_{\max},\ \dfrac{c_{\text{pp}}(z) V_{\text{real}}(z) v_{\text{pp}} \phi_{\max}}{s^*} \right), & \text{otherwise.} \end{cases}$$

Here, $c_{\text{pp}}(z)$ is the number concentration of primary particles in compartment z, s^* is the pore liquid saturation limit, $\phi_{\max}$ is maximum liquid saturation of solid material during nucleation and V_{real} is the physical volume of the compartment occupied by the granular mass (including the bed voidage), which sets the scale of the 'physical' system. v_{drop} is the number average volume of a droplet, which, in this study, takes the volume of a sphere with the same diameter as the liquid addition nozzle d_{nozzle}.

The two cases in equation above cover the situations in which:

1. there is sufficient primary particle mass in the droplet zone to permit formation of a complete nucleus particle
2. there is insufficient primary particle mass in the droplet zone and a partially formed nucleus is created, which has a non-zero amount of external liquid

A single droplet creates a single nucleus particle, hence the nucleation rate $R_{\text{nuc}}(z,t)$ is equal to the rate of droplet addition $R_{\text{drop}}(z,t)$, which is defined as

$$R_{\text{drop}}(z,t) = \begin{cases} \dfrac{(\text{LSR})\dot{m}_{\text{feed}}}{v_{\text{drop}}\rho_{\text{l}}}, & \text{if } z = 1, \\ 0, & \text{otherwise.} \end{cases} \tag{7.3}$$

In the context of the aggregate PBE (7.1), the nucleation rate is

$$I_{\text{nuc}}(z,t,c_{\text{pp}},\mathrm{d}x) = \frac{R_{\text{nuc}}(z,t)\delta_{x_{\text{nuc}}(z,c_{\text{pp}},t)}(x)\mathrm{d}x}{V_{\text{real}}(z)}. \tag{7.4}$$

Collision and coagulation

The second term in the PBE (7.1) represents binary collisions and coagulation between aggregate particles. This mechanism is the same as the particle coagulation mechanism described in Chapter 3, except that the consolidation transformation T_{comp} has been removed and a new kernel has been utilised. Like the particle collision mechanisms of Chapter 3, aggregate particle collision results in coalescence if the Stokes criterion is satisfied.

Particles collide according to the size-dependent collision kernel K_{col}, which takes the form

$$K_{\text{col}}(z,x_i,x_j) = k_{\text{col}}(z)n_{\text{screw}}C(d(x_i),d(x_j)) \tag{7.5}$$

Here, $C(d_1,d_2)$ is the collision rate function which defines the collision frequency between particles with diameter d_1 and d_2, respectively. In this chapter, the Equipartition of kinetic energy collision rate function [162] is used, which takes the form

$$C(d_i,d_j) = (d_i+d_j)^2\sqrt{\frac{1}{d_i^3}+\frac{1}{d_j^3}}. \tag{7.6}$$

Studies using the Discrete Element Method (DEM) [32] have shown that the form of the collision function in (7.6) adequately describes the collision dynamics within batch granulation systems [94]. Furthermore, preliminary twin-screw simulations with this form of collision rate function showed that it promoted collisions between large agglomerates and primary particles over those between particles which were similar in size. Thus, in the absence of an existing twin-screw specific collision kernel, the kernel in Equation (7.6) was deemed acceptable for the purposes of aggregate collisions and layering (to be introduced in Section 7.2.3).

The coagulation kernel K_{coag} of PBE (7.1) remains as

$$K_{\text{coag}}(z,x_i,x_j) = K_{\text{col}}(z,x_i,x_j)\mathbb{1}_{\{x_i,x_j|\text{St}_\text{v}(x_i,x_j)\leq\text{St}_\text{v}^*(x_i,x_j)\}}(x_i,x_j). \tag{7.7}$$

Breakage

The breakage particle transformation remains unchanged, however, the breakage frequency function of Chapter 3 has been adapted to include a variable breakage rate exponent ω_{att}. The new breakage frequency function takes the form

$$g_{\text{break}}(z,x) = \begin{cases} k_{\text{att}}(z)n_{\text{screw}}^2\left(\dfrac{v(x)}{\hat{v}_{\text{break}}}\right)^{\omega_{\text{att}}(z)}, & \text{if } v(x) \geq v_{\text{parent}}^{\text{min}} \text{ and} \\ & l_\text{e}(x)+l_\text{i}(x)+p(x)\neq 0, \\ 0 & \text{otherwise,} \end{cases} \tag{7.8}$$

where $v_{\text{parent}}^{\text{min}}$ is the minimum agglomerate size that can undergo breakage and $\hat{v}_{\text{break}}$ is a normalisation parameter. In this work $v_{\text{parent}}^{\text{min}} = v_{\text{pp}}$. The breakage of primary particles is not permitted in the current model.

The breakage kernel F is the same as that in Chapter 3. Again, the daughter distribution is characterised using χ_{frag}, which controls the size of abraded particles. In this chapter, the volume of the abraded particle is given by

$$v_y(z,x,\chi_{\text{frag}}) = v_{\text{parent}}^{\text{min}} + \chi_{\text{frag}}\left[v(x) - v_{\text{parent}}^{\text{min}}\right], \tag{7.9}$$

where χ_{frag} is a random measure with beta distribution $f(z,\chi_{\text{frag}})$ with skewness parameters $\alpha_{\text{daughter}}(z)$ and $\beta_{\text{daughter}}(z)$.

As mentioned in Section 7.1, conveying elements have been observed to break particles through cutting and edge chipping. No daughter distribution breakage data is currently available for kneading elements. However, based on their

somewhat similar geometry, it is expected that the primary breakage mechanism in these elements will be similar to that in so called distributive mixing elements (DME) [147]. In this work, it is hypothesised that the primary breakage mechanisms in kneading elements will be the crushing behaviour observed in DME, with less emphasis on the chipping mechanism, due to the absence of the pronounced blades that are present in DME. To incorporate this information into the model, breakage exponent and daughter distribution parameters differ between different types of compartment (or, equivalently, screw element). The probability density distribution for the χ_{frag} used for each element in this study are illustrated in Figure 7.2.

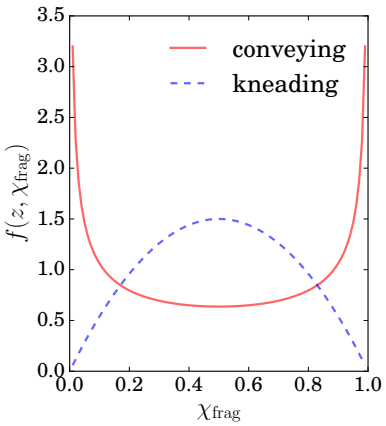

Fig. 7.2 Element specific probability density functions for agglomerate breakage. In compartments that represent pure conveying zones $\alpha_{\text{daughter}} = \beta_{\text{daughter}} = 0.5$ and those representing pure kneading zones $\alpha_{\text{daughter}} = \beta_{\text{daughter}} = 2$.

Aggregate transport

The fourth and fifth terms in the PBE (7.1) represent aggregate inflow and outflow processes on compartment z, respectively. Agglomerates and primary particles are permitted to flow uni-directionally along the network of compartments from the feed zone to the exit zone. Each compartment is modelled as a perfectly stirred tank such that each particle flows out of compartment z with rate $1/\tau(z)$, where $\tau(z)$ is the compartment residence time. Similarly, aggregate particles flow into compartment z from compartment $z-1$ at rate r_{inflow} where

$$r_{\text{inflow}}(z) = \begin{cases} 1/\tau(z-1) & \text{if } z > 1, \\ 0 & \text{otherwise.} \end{cases} \tag{7.10}$$

Continuous, deferred aggregate processes

A number of particle mechanisms are modelled as continuous processes that act on the agglomerates (and indirectly on the primary particles) in the system according to the deferment function $D_t : (\mathbb{L}, \mathbb{X}_{\text{agg}}, \mathbb{R}^+) \mapsto \mathbb{X}_{\text{agg}}$ introduced in Section 7.2.2.

These processes are:

1. Layering

   Layering is the processes by which primary particles attach to the surface of the agglomerates. This process is modelled as a collision between agglomerates and primary particles using the same size-dependent collision kernel used for aggregate coagulation (Equation (7.5)).

   Layering is only permitted on agglomerates which have a volume of external liquid with height h_{l} exceeding the fixed height of asperities of the agglomerate particles h_{a}. The height of the external liquid on particle x is defined as

   $$h_{\text{l}}(x) = \frac{1}{2}\sqrt[3]{\frac{6}{\pi}}\left[\sqrt[3]{v(x)} - \sqrt[3]{v(x) - l_{\text{e}}(x)}\right]. \tag{7.11}$$

   In the current model, a successful layering event is theorised to 'dry out' the surface of the agglomerate particle. This drying is captured by the transformation of external liquid to internal liquid. For the addition of a single primary particle onto the surface of an agglomerate, the amount of liquid moved from the exterior to the interior is modelled as

   $$l_{\text{e}\to\text{i}}(x) = \min(v_{\text{pp}}, \pi d_{\text{pp}}^2 h_{\text{l}}(x)). \tag{7.12}$$

   The form of (7.12) was constructed to cover the situations where the agglomerate surface is liquid rich and liquid poor. In the liquid rich case, a small primary may become fully immersed in the thick binder layer. In liquid poor situation, the primary particle is more likely to simply stick to the surface, hence the amount of internalisation is hypothesised to be proportional to the projected area of the primary.

It follows from the definitions above that the agglomerate particle x undergoes layering with rate

$$r_{\text{layer}}(z,t,c_{\text{pp}},x) = \begin{cases} c_{\text{pp}}(z,t)K_{\text{col}}(z,d(x),d_{\text{pp}}), & \text{if } h_{\text{l}}(x) > h_{\text{a}}, \\ 0, & \text{otherwise}, \end{cases} \tag{7.13}$$

$$\hat{K}_{\text{col}}(z,d(x),d_{\text{pp}}) = k_{\text{col}}(z)n_{\text{screw}}C(d(x),d_{\text{pp}}), \tag{7.14}$$

and the rates of change of each particle property induced by the layering process are

$$\left.\frac{\mathrm{d}s_{\text{o}}(x)}{\mathrm{d}t}\right|_{\text{layer}} = r_{\text{layer}}(z,x,c_{\text{pp}},t)v_{\text{pp}}, \tag{7.15}$$

$$\left.\frac{\mathrm{d}l_{\text{e}}(x)}{\mathrm{d}t}\right|_{\text{layer}} = -r_{\text{layer}}(z,x,c_{\text{pp}},t)l_{\text{e}\to\text{i}}(x), \tag{7.16}$$

$$\left.\frac{\mathrm{d}l_{\text{i}}(x)}{\mathrm{d}t}\right|_{\text{layer}} = r_{\text{layer}}(z,x,c_{\text{pp}},t)l_{\text{e}\to\text{i}}(x), \tag{7.17}$$

$$\left.\frac{\mathrm{d}p(x)}{\mathrm{d}t}\right|_{\text{layer}} = r_{\text{layer}}(z,x,c_{\text{pp}},t)l_{\text{e}\to\text{i}}(x). \tag{7.18}$$

2. Consolidation

Consolidation of particles within the twin-screw system is presumed to occur primarily due to impacts between the particles and screw and walls of the barrel. The consolidation processe is modelled as the reduction in particle porosity and subsequent squeezing of the internal liquid to the surface. It is presumed that the rate of consolidation is dependent on the screw speed and the geometry of the screw element in which the process is taking place. Since the effect of screw speed is not being investigated in this study, a simple consolidation model is employed. This takes the form:

$$\left.\frac{\mathrm{d}\varepsilon(x)}{\mathrm{d}t}\right|_{\text{consol}} = -k_{\text{comp}}(z)n_{\text{screw}}[\varepsilon(x) - \varepsilon_{\text{min}}], \tag{7.19}$$

where $k_{\text{comp}}(z)$ is the compaction rate constant in compartment z and ε_{min} is the minimum porosity permitted for agglomerate particles.

The associated changes in the tracked particle properties due to consolidation are

$$\left.\frac{\mathrm{d}s_\mathrm{o}(x)}{\mathrm{d}t}\right|_\mathrm{consol} = 0, \tag{7.20}$$

$$\left.\frac{\mathrm{d}l_\mathrm{e}(x)}{\mathrm{d}t}\right|_\mathrm{consol} = -\frac{l_\mathrm{i}(x)}{p(x)}\frac{\mathrm{d}p(x)}{\mathrm{d}t}, \tag{7.21}$$

$$\left.\frac{\mathrm{d}l_\mathrm{i}(x)}{\mathrm{d}t}\right|_\mathrm{consol} = -\frac{\mathrm{d}l_\mathrm{e}(x)}{\mathrm{d}t}, \tag{7.22}$$

$$\left.\frac{\mathrm{d}p(x)}{\mathrm{d}t}\right|_\mathrm{consol} = v(x)\frac{\mathrm{d}\varepsilon(x)}{\mathrm{d}t}. \tag{7.23}$$

Note that this has no effect on the primary particles since they have an $\varepsilon = 0$.

The aggregate deferment function D_t maps a particle x and primary particle concentration measure $c_\mathrm{pp}(z)$ in z at time t_p to a particle $D_t(z,x,c_\mathrm{pp})$ with time t (where t_p is the current time of particle x, $t_p \leq t$). This is done by evolving x in time according to the rates

$$\left.\frac{\mathrm{d}s_\mathrm{o}(x)}{\mathrm{d}t}\right|_\mathrm{defer} = \left.\frac{\mathrm{d}s_\mathrm{o}(x)}{\mathrm{d}t}\right|_\mathrm{layer} + \left.\frac{\mathrm{d}s_\mathrm{o}(x)}{\mathrm{d}t}\right|_\mathrm{consol}, \tag{7.24}$$

$$\left.\frac{\mathrm{d}l_\mathrm{e}(x)}{\mathrm{d}t}\right|_\mathrm{defer} = \left.\frac{\mathrm{d}l_\mathrm{e}(x)}{\mathrm{d}t}\right|_\mathrm{layer} + \left.\frac{\mathrm{d}l_\mathrm{e}(x)}{\mathrm{d}t}\right|_\mathrm{consol}, \tag{7.25}$$

$$\left.\frac{\mathrm{d}l_\mathrm{i}(x)}{\mathrm{d}t}\right|_\mathrm{defer} = \left.\frac{\mathrm{d}l_\mathrm{i}(x)}{\mathrm{d}t}\right|_\mathrm{layer} + \left.\frac{\mathrm{d}l_\mathrm{i}(x)}{\mathrm{d}t}\right|_\mathrm{consol}, \tag{7.26}$$

$$\left.\frac{\mathrm{d}p(x)}{\mathrm{d}t}\right|_\mathrm{defer} = \left.\frac{\mathrm{d}p(x)}{\mathrm{d}t}\right|_\mathrm{layer} + \left.\frac{\mathrm{d}p(x)}{\mathrm{d}t}\right|_\mathrm{consol}. \tag{7.27}$$

Hence, if

$$\left.\frac{\mathrm{d}x}{\mathrm{d}t}\right|_\mathrm{defer} = \left(\left.\frac{\mathrm{d}s_\mathrm{o}(x)}{\mathrm{d}t}\right|_\mathrm{defer}, \left.\frac{\mathrm{d}l_\mathrm{e}(x)}{\mathrm{d}t}\right|_\mathrm{defer}, \left.\frac{\mathrm{d}l_\mathrm{i}(x)}{\mathrm{d}t}\right|_\mathrm{defer}, \left.\frac{\mathrm{d}p(x)}{\mathrm{d}t}\right|_\mathrm{defer}\right)^\top, \tag{7.28}$$

then

$$D_t(z,x,c_\mathrm{pp}) = x + \int_{t_p}^{t} \left.\frac{\mathrm{d}x}{\mathrm{d}t}\right|_\mathrm{defer} \mathrm{d}t. \tag{7.29}$$

7.2.4 Primary particle processes

In this section the operators in the primary particle PBE (Equation (7.2)) are described.

The first term in Equation (7.2) represents the transport operator (inflow and outflow) acting on the primary particles phase in compartment z. This is characterised by

$$I_{\text{trans,pp}}(z,t) = \begin{cases} \left[\dfrac{\dot{m}_{\text{feed}}}{v_{\text{pp}}\rho_{\text{s}}} - \dfrac{N_{\text{pp}}(z)}{\tau(z)}\right]\dfrac{1}{V_{\text{real}}(z)}, & \text{if } z = 1, \\ \left[\dfrac{N_{\text{pp}}(z-1)}{\tau(z-1)} - \dfrac{N_{\text{pp}}(z)}{\tau(z)}\right]\dfrac{1}{V_{\text{real}}(z)} & \text{otherwise.} \end{cases} \tag{7.30}$$

The second term in Equation (7.2) represents the nucleation sink term, which complements the aggregate nucleation model by taking the form

$$I_{\text{nuc,pp}}(t,z) = \begin{cases} \dfrac{\dot{m}_{\text{feed}}\text{LSR}}{v_{\text{pp}}\rho_{\text{l}}\phi_{\text{max}}V_{\text{real}}(z)}, & \text{if } z = 1, \\ 0, & \text{otherwise.} \end{cases} \tag{7.31}$$

The final term in (7.2) accounts for the depletion of primary particles through the deferred aggregate layering process (Equations (7.13)-(7.18)).

7.2.5 Compartmentalisation

In the model used in this chapter, each compartment represents exactly one type of screw element. However, a screw element may be represented by more or less than one compartment (as demonstrated in Figure 7.3). As such, the total number of compartments employed may vary depending on the screw configuration being modelled. This allows increased resolution in areas where the changes in particle characteristics along the screw length are expected to be significant, such as the region around the liquid inception port. This is also the case in regions where the material flow is expected to more closely resemble a plug-flow, with limited back mixing, such as kneading elements.

As in existing twin-screw modelling efforts, its is assumed that the material undergoes very little change prior to the point of liquid inception (termed the "metering" zone), hence the screw configuration is modelled from the liquid inlet port onward (termed the "variation" zone). This liquid inception zone (droplet

zone) in modelled as a conveying compartment with length 0.33D (where D is the diameter of the screw) which serves as the first compartment in all screw configurations investigated. An example of the compartmentalisation of a screw configuration used in this study is presented in Figure 7.3.

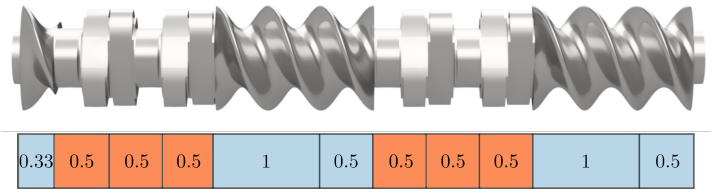

Fig. 7.3 Example screw configuration (variation zone only) and the associated compartmental representation. The number in the centre of each compartment represents the compartment length (normalised by the screw diameter). Compartments representing conveying zones are in blue and compartments representing kneading zones are shown in orange.

7.2.6 Residence time estimation

The compartment residence times $\tau(z)$ that control the aggregate and primary particle flow rates are dependent on the compartmentalisation of the screw and the operating conditions. In previous TSG modelling studies, compartmental residence times have been estimated through the use of DEM [12] and chemical imaging techniques [7, 88, 89]. In the case where DEM has been used, the PBM and DEM solvers are coupled, allowing collision statistics [8] and residence time estimation to be made, however, the significant computational cost of the DEM step negatively impacts the overall time required to solve the model. Hence, it is advantageous to have the ability to estimate the residence time of individual compartments simply from the screw configuration and device operation (mass and liquid flow rates). It is worth noting that, in studies of alternative granulation devices, such as Barrasso et al. [14], the costly DEM step has been replaced by an Artificial Neural Net (ANN) with promising results, though a sizeable amount of DEM data must be gathered to train such networks.

As discussed in Section 7.1, it is known that the screw configuration strongly influences the mass distribution across the screw barrel and can therefore affect the amount of time that particles spend in particular regions of the screw. In order to be able to produce reasonable estimates of particle residence times of screw sections and model compartments for arbitrary screw configurations, a novel but

simplistic approach was developed in this work. The approach involves two key stages: firstly, the mean residence time of the complete device τ_{screw} is linearly interpolated from existing experimental data based on the screw configuration, screw speed and mass feed rate. In the second stage, this total device residence time is distributed over the compartmental network by estimating the mass distribution profile across the compartments. In this work, data from the residence time analysis experiments performed by Kumar et al. [88] is used. In that study, the authors used a chemical imaging approach where a dye-impulse was introduced into the powder feed zone in order to extract residence time distributions. These residence time estimates consider the full screw (i.e. both metering and variation zones) and the metering zone consisted purely of conveying elements.

The total mean screw residence time is split into the contribution from the metering zone and the variation zone as

$$\tau_{\text{screw}} \approx \tau_{\text{metering}} + \tau_{\text{variation}}. \tag{7.32}$$

Assuming that each section behaves as perfect plug-flow with no back-mixing then,

$$\tau_{\text{screw}} \approx \frac{M_{\text{metering}}}{\dot{m}_{\text{feed}}} + \frac{M_{\text{variation}}}{\dot{m}_{\text{feed}}(1+\text{LSR})}, \tag{7.33}$$

where M_{metering} and $M_{\text{variation}}$ are dynamic mass hold-up (i.e. the mass of material that is not 'stuck' to the barrel wall and screws) within the metering and variation zones, respectively. These are given as

$$M_{\text{metering}} = \sum_{i=1}^{N_{\text{m,convey}}} L_{\text{m,convey}}(i)\, v_{\text{convey}}\, \varepsilon_{\text{bed}}\, \rho_{\text{s}}\, f_{\text{m,convey}}(i), \tag{7.34}$$

$$\begin{aligned} M_{\text{variation}} = &\sum_{i=1}^{N_{\text{v,convey}}} L_{\text{v,convey}}(i)\, v_{\text{convey}}\, \varepsilon_{\text{bed}}\, \rho_{\text{eff}}\, f_{\text{v,convey}}(i) \\ &+ \sum_{i=1}^{N_{\text{v,knead}}} L_{\text{v,knead}}(i)\, v_{\text{knead}}\, \varepsilon_{\text{bed}}\, \rho_{\text{eff}}\, f_{\text{v,knead}}(i) \end{aligned} \tag{7.35}$$

where the subscripts *m* and *v* refer to the metering and variation zones respectively and

- $N_{\text{j,convey}}$ is the number of conveying elements in zone j;
- $N_{\text{j,knead}}$ is the number of kneading elements in zone j;

- $L_{\mathrm{j,e}}(i)$ is the length of the i^{th}; screw section consisting of element type e in zone j (measured in screw diameters D);
- v_{e} is the specific volume available in a screw section with element type e (measured in unit volume/length in screw diameters D);
- $f_{\mathrm{j,e}}(i)$ is the volumetric fill fraction of the i^{th} screw section consisting of element type e in zone j;
- ρ_{eff} is the effective density of the solid material being held up in the variation zone;

For simplicity it is assumed that ρ_{eff} is constant along the length of the variation zone. The effective density is computed as the weighted averaged density of the solid and liquid feed such that:

$$\rho_{\mathrm{eff}} = \frac{(\mathrm{LSR}+1)\rho_s\rho_l}{\rho_l + \rho_s \mathrm{LSR}}. \tag{7.36}$$

Again, ρ_s is the density of solid feed material and ρ_l is the density of the liquid binder.

It is imposed that kneading elements are filled to capacity with material (i.e. $f_{\mathrm{v,knead}}(i) = f_{\mathrm{v,knead}} = 1 \; \forall \, i \in \{1,\ldots,N_{\mathrm{v,knead}}\}$). Though PEPT studies [151] have shown that conveying elements that precede a kneading element will generally have a higher fill fraction, for the purposes of the residence time estimation in this work it is assumed that each compartment of element type e has the same fill fraction, such that $f_{\mathrm{m,convey}}(i) = f_{\mathrm{v,convey}}(k) = f_{\mathrm{convey}} \; \forall \, i \in \{1,\ldots,N_{\mathrm{m,convey}}\}, k \in \{1,\ldots,N_{\mathrm{v,convey}}\}$. This assumption permits f_{convey} to be solved by substitution of (7.34) and (7.35) into (7.33) and re-arranging to yield

$$f_{\mathrm{convey}} = \frac{\tau_{\mathrm{screw}}\dot{m}_{\mathrm{feed}}(1+\mathrm{LSR}) - f_{\mathrm{v,knead}}\varepsilon_{\mathrm{bed}}v_{\mathrm{knead}}\sum_{i=1}^{N_{\mathrm{v,knead}}} L_{\mathrm{v,knead}}(i)}{\varepsilon_{\mathrm{bed}}v_{\mathrm{convey}}\left[\rho_s(1+\mathrm{LSR})\sum_{i=1}^{N_{\mathrm{m,convey}}} L_{\mathrm{m,convey}}(i) + \rho_{\mathrm{eff}}\sum_{i=1}^{N_{\mathrm{v,convey}}} L_{\mathrm{v,convey}}(i)\right]}. \tag{7.37}$$

Assuming that kneading elements are filled to capacity, knowledge of f_{convey} specifies the mass distribution across the full screw.

Given that compartment z represents a section of the screw composed of elements of type e, with length $L(z)$ and steady state mass hold-up $M(z)$, then the

compartment residence time is approximated as

$$\tau(z) := \frac{M(z)}{\dot{m}_{\text{feed}}} \tag{7.38}$$

$$= \frac{L(z)\nu_{\text{e}}\varepsilon_{\text{bed}}\rho_{\text{eff}}f_{\text{v,e}}}{\dot{m}_{\text{feed}}}. \tag{7.39}$$

Since no residence time data was presented for pure conveying screws in Kumar et al. [88], residence times for such screw configurations were estimated using the derived steady state fill fraction predicted using the above flow model, applied to a configuration with two kneading blocks (13.3%).

Derived fill fractions for conveying elements ranged from 10 - 13.3%, and overall derived fill levels between 13.3 - 24.1% with $\varepsilon_{\text{bed}} = 0.3$, depending on the screw configuration. This gives the fraction of screw bed occupied by material (i.e. discounting the packing fraction) as 4-7.23%. These values are lower than the ranges observed in alternative twin-screw devices (10-30%) [113], however, the method presented in this work does not account for non-dynamic mass (i.e. material that is stuck to the walls), which could be significant as demonstrated in other experimental studies [145].

Given a fill fraction for each element type, the real volume of material (including the bed voidage) modelled in each compartment $V_{\text{real}}(z)$ is computed as

$$V_{\text{real}}(z) = L(z)\nu_{\text{e}}f_{\text{v,e}}. \tag{7.40}$$

Note that the use of this residence time model inherently relaxes the equal-compartment volume assumption made in previous chapters.

7.3 Numerical implementation

7.3.1 Stochastic particle methods for twin-screw granulation

The general stochastic weighted particle methodology described in Chapter 4 and further investigated in Chapter 6 is again used to simulate aggregate particle phase of the new model. Some jump processes are altered to reflect changes in the process description.

The aggregate phase of each compartment z is simulated with a discrete list of computational particles

$$(z, x_i, w_i), \quad i = 1, \ldots, N_{\text{agg}}(z,t), \tag{7.41}$$

which describes the population dynamics in (7.1). In (7.41), $x \in \mathbb{X}_{\text{agg}}$, $w_i \in (0, w_{\max}]$ is the statistical weight of the particle with index i and $N_{\text{agg}}(z,t)$ is the total number of aggregate stochastic particles in compartment z at time t.

7.3.2 Splitting scheme

Due to the small size of primary particles relative to large agglomerates within twin-screw devices, the number concentration of these species may differ by several orders of magnitude. In such situations it is unfeasible to solve the primary particle part of the twin-screw population balance problem using a stochastic particle method (unless the primary particle size is significant relative to the mean aggregate size, or in cases where the physical collision rates to be simulated are relatively low). This is due to the fact that the collision jump rates required for significant transfer of mass between the two species becomes too computationally intensive to simulate within reasonable time-scales. For this reason, the primary particle population balance equation (7.2) is solved using an implicit ODE solution technique (discussed further in Section 7.3.4). The use of both stochastic particle and ODE methods to solve different parts of the coupled population balance equations (7.1) and (7.2) closely follows the operator splitting technique presented by Celnik et al. [27]. The nature and implementation of the splitting are discussed further in the following sections.

Due to the interaction between individual stochastic particles and the primary particle phase, it is often more convenient to work in terms of the absolute number of primary particles within a given sample volume (as opposed to the number concentration.) Hence, for the remainder of this chapter will work in terms of primary particle number and $N_{\text{pp}}(z,t)$ is to be understood as the number of primary particles that exist within the sample volume $V_{\text{samp}}(z,t)$ corresponding to physical compartment z at time t.

7.3.3 Jump processes

The stochastic jump processes associated with the new twin-screw population balance model are presented in this section. Since all of the weight transfer functions employed within these jump processes have been shown to converge to the appropriate forms in the un-weighted aggregate PBE (7.2), the associated weighted population balance equation is not presented here. For details of the various convergence proofs the reader is directed to works [94, 96, 132, 135].

Nucleation

The nucleation jump involves the inception of particles of the form

$$(z, x_{\text{nuc}}, w_{\text{nuc}}) \tag{7.42}$$

at rate

$$R_{\text{nuc}}^{\text{SWA}}(z,t) = \begin{cases} \dfrac{R_{\text{drop}}(z,t)V_{\text{samp}}(z,t)}{V_{\text{real}}(z)w_{\text{nuc}}}, & \text{if } z = 1, \\ 0 & \text{otherwise,} \end{cases} \tag{7.43}$$

where w_{nuc} is the statistical weight of the nucleus particle to be added. Since the nucleation is the only jump process in this work which increases the number of computational particles in the droplet zone ($z = 1$) and transport is the only process which reduces the number of stochastic particle in this zone, the number of particle in $z = 1$ can be held approximately constant by enforcing

$$R_{\text{nuc}}^{\text{SWA}}(z,t) \approx R_{\text{trans}}^{\text{SWA}}(z,t), \tag{7.44}$$

where $R_{\text{trans}}^{\text{SWA}}(z,t)$ is the transport jump rate in compartment z (detailed in Section 7.3.3).

From (7.3), (7.43) and (7.44) it follows that

$$w_{\text{nuc}}(z,t) = \frac{(\text{LSR})\dot{m}_{\text{feed}}V_{\text{samp}}(z,t)}{v_{\text{drop}}\rho_{\text{l}}V_{\text{real}}(z)R_{\text{trans}}^{\text{SWA}}(z,t)}. \tag{7.45}$$

Coagulation

Aggregate collision jumps take the following number-conserving form

Coagulating collision:

$$(z,x_i,w_i),(z,x_j,w_j) \mapsto (z,T_{\text{coag}}(x_i,x_j),\gamma_{\text{coag}}(x_i,w_i,x_j,w_j)),(z,x_j,w_j), \quad (7.46)$$

Non-coagulating collision:

$$(z,x_i,w_i),(z,x_j,w_j) \mapsto (z,x_i,w_i),(z,x_j,w_j), \quad (7.47)$$

where γ_{coag} is the same coagulation weight transfer function employed introduced in Chapter 4, Section 4.3.5. Again, the SWA collision kernel associated with γ_{coag} is [135]

$$K_{\text{col}}^{\text{SWA}}(z,x_i,w_i,x_i,w_j) = K_{\text{col}}(z,x_i,x_j)w_j \quad (7.48)$$

$$= k_{\text{col}}(z)n_{\text{screw}}(d_i+d_j)^2\sqrt{\frac{1}{d_i^3}+\frac{1}{d_j^3}}w_j \quad (7.49)$$

and the SWA coagulation kernel is

$$K_{\text{coag}}^{\text{SWA}}(z,x_i,w_i,x_i,w_j) = K_{\text{col}}^{\text{SWA}}(z,x_i,w_i,x_i,w_j)\mathbb{1}_{\{x_i,x_j|\text{St}_{\text{v}}(x_i,x_j)\leq\text{St}_{\text{v}}^*(x_i,x_j)\}}(x_i,x_j). \quad (7.50)$$

Due to the complex form of (7.49), the repeated evaluation of the associated total collision rate in each compartment is very computationally intensive, since it requires looping through each pair of aggregates within the ensemble. For this reason, a majorant kernel is employed. An in-depth treatment of majorant techniques and their application to the solution of population balance problems can be found in [43, 61, 64, 118, 135]. The majorant form of (7.49) used is

$$\hat{K}_{\text{col}}^{\text{SWA}}(z,x_i,w_i,x_i,w_j) = k_{\text{maj}}k_{\text{col}}(z)n_{\text{screw}}(d_i^2+d_j^2)\left(\frac{1}{d_i^{1.5}}+\frac{1}{d_j^{1.5}}\right)w_j, \quad (7.51)$$

where k_{maj} is the majorant scaling factor. As in Lee et al. [94], k_{maj} was set to 1.42 in order to satisfy the inequality $K_{\text{col}}^{\text{SWA}} < \hat{K}_{\text{col}}^{\text{SWA}}$ throughout the simulation.

The majorant collision jump rate in compartment z at time t is (adapted to the current model from [94])

$$
\begin{aligned}
R^{\mathrm{SWA}}_{z,\,\mathrm{col}}(z,t) &= \frac{1}{V_{\mathrm{samp}}(z,t)} \sum_{i\neq j}^{N_{\mathrm{agg}}(z,t)} \hat{K}^{\mathrm{SWA}}_{\mathrm{col}}(z,x_i,w_i,x_j,w_j) \\
&= \frac{k_{\mathrm{maj}}\, k_{\mathrm{col}}(z) n_{\mathrm{screw}}}{V_{\mathrm{samp}}(z,t)} \Bigg\{ \left[\sum_{i=1}^{N_{\mathrm{agg}}(z,t)} {d_i}^{0.5} \sum_{j=1}^{N_{\mathrm{agg}}(z,t)} w_j - \sum_{i=1}^{N_{\mathrm{agg}}(z,t)} {d_i}^{0.5} w_i \right] \\
&+ \left[\sum_{i=1}^{N_{\mathrm{agg}}(z,t)} {d_i}^{2} \sum_{j=1}^{N_{\mathrm{agg}}(z,t)} {d_j}^{-1.5} w_j - \sum_{i=1}^{N_{\mathrm{agg}}(z,t)} {d_i}^{0.5} w_i \right] \\
&+ \left[\sum_{i=1}^{N_{\mathrm{agg}}(z,t)} {d_i}^{-1.5} \sum_{j=1}^{N_{\mathrm{agg}}(z,t)} {d_j}^{2} w_j - \sum_{i=1}^{N_{\mathrm{agg}}(z,t)} {d_i}^{0.5} w_i \right] \\
&+ \left[\sum_{i=1}^{N_{\mathrm{agg}}(z,t)} 1 \sum_{j=1}^{N_{\mathrm{agg}}(z,t)} {d_j}^{0.5} w_j - \sum_{i=1}^{N_{\mathrm{agg}}(z,t)} {d_i}^{0.5} w_i \right] \Bigg\}. \qquad (7.52)
\end{aligned}
$$

Using the majorant rate expression in (7.52), jumps are accepted with probability

$$
\mathbb{P}_{\mathrm{accept}}(z,x_i,w_i,x_j,w_j) = \frac{K^{\mathrm{SWA}}_{\mathrm{col}}(z,x_i,w_i,x_i,w_j)}{\hat{K}^{\mathrm{SWA}}_{\mathrm{col}}(z,x_i,w_i,x_i,w_j)}, \qquad (7.53)
$$

otherwise the jump is fictitious, in which case the ensemble remains unchanged and time moves forward according to (4.5). The cost reduction gained through the majorant technique here comes from the fact that one no longer has to compute expression (7.49) for every particle pair in the ensemble. Instead, if a particle state is altered through any jump process (be it breakage, collision or nucleation) only a single term in sum (7.52) needs to be changed to reflect the new state of the system. Furthermore, since sum terms in (7.52) are held in a binary tree structure, recomputation of the full sum (7.52) comes at a much lower average computational cost than if one were to simply sum a list, as described earlier in Chapter 4. Note that the expression (7.53) need only be evaluated once for the collision pair selected to take part in the jump (i.e. not between every pair in the ensemble) in order to maintain the correct jump rate. This is because the majorant jump takes the following undeferred form within the context of the

weighted PBE:

$$\int_{(\mathbb{X}_{\text{agg}}\times\mathbb{W})} \Big[\psi(z, T_{\text{nuc}}(x_i,x_j), \gamma_{\text{coag}}(x_i,w_i,x_j,w_j)) + \psi(z,x_j,w_j) \\ -\psi(z,x_i,w_i) - \psi(z,x_j,w_j)\Big]\, \hat{K}_{\text{col}}^{\text{SWA}}(z,x_i,w_i,x_i,w_j)\mathbb{P}_{\text{accept}}(z,x_i,w_i,x_j,w_j) \\ Q(z,t,\mathrm{d}x_i,\mathrm{d}w_i)Q(z,t,\mathrm{d}x_j,\mathrm{d}w_j), \tag{7.54}$$

which, upon substitution of (7.53), yields:

$$\int_{(\mathbb{X}_{\text{agg}}\times\mathbb{W})^2} \Big[\psi(z, T_{\text{nuc}}(x_i,x_j), \gamma_{\text{coag}}(x_i,w_i,x_j,w_j)) + \psi(z,x_j,w_j) \\ -\psi(z,x_i,w_j) - \psi(z,x_j,w_j)\Big]\, K_{\text{col}}^{\text{SWA}}(z,x_i,w_i,x_i,w_j) \\ Q(z,t,\mathrm{d}x_i,\mathrm{d}w_i)Q(z,t,\mathrm{d}x_j,\mathrm{d}w_j). \tag{7.55}$$

One sees that this is equivalent to the jump process (7.46) occurring with the with rate based on the 'true' SWA collision kernel $K_{\text{col}}^{\text{SWA}}$.

Again, the collision pair must satisfy the Stokes criterion in order for the jump to proceed, otherwise the collision is non-coagulating and the system remains unchanged, since the jump (7.47) has no effect on the system state.

For a full derivation of the majorant rate expression in (7.52) and the associated particle selection measures, the reader is referred to Lee et al. [94].

Breakage

This jump process follows exactly, the breakage jump process described in Chapter 4, Section 4.3.5. The only change being that the new breakage frequency function g_{break} (Equation (7.8)) is used.

Transport

Aggregate particle inflow and outflow processes are grouped and carried out under an overarching 'transport' jump process. The transport jump takes the following spatially-dependent forms

1. Droplet zone ($z = 1$)
   Due to the absence of aggregate inflow in to the first reactor, the transport

jump only captures outflow through the deletion of a stochastic particle as

$$(z,x,w) \mapsto \text{deleted}. \tag{7.56}$$

2. Non-droplet zone ($z > 1$)

$$(z,x_i,w_i) \mapsto \text{deleted}, \tag{7.57}$$
$$(z-1,x_j,w_j) \mapsto (z,x_j,F_{\text{c}}(z,t)w_j). \tag{7.58}$$

Here, F_{c} is the transport scaling factor required to maintain continuity, which, for a series of compartments with varying physical volumes, takes the form

$$F_{\text{c}}(z,t) = \frac{V_{\text{samp}}(z,t)N_{\text{agg}}(z-1,t)}{V_{\text{samp}}(z-1,t)N_{\text{agg}}(z,t)}. \tag{7.59}$$

A complete derivation of (7.59) is provided in Appendix A.1.

In all zones, the transport jump is carried out with total rate

$$R^{\text{SWA}}_{\text{trans}}(z,t) = \frac{N_{\text{agg}}(z,t)}{\tau(z)}. \tag{7.60}$$

7.3.4 Continuous Processes

Primary particle transport, primary particle depletion through nucleation, layering of primary particles onto stochastic particles (aggregates) and aggregate consolidation are carried out as continuous processes using the Linear Process Deferment Algorithm (LPDA) [133]. In the LPDA, deferred processes are carried out at two specific stages during the simulation:

1. Local Application

   Here, stochastic particles that are selected to take part in one of the jump processes described in Section 7.3.3 are brought up to the current simulation time t by applying the aggregate deferment function D_t to each of the selected particles in turn (see Section 7.2.3). This is done just before the jump transforms are applied (i.e."just in time").

2. Global Application

In these instances, the continuous processes are periodically applied to the full ensemble of stochastic particles between jump processes. This global deferment is carried out with rate $1/\Delta t_{\text{defer}}$, where Δt_{defer} is the deferment time step. The global deferment procedure is described in detail in Algorithm 2. Primary particle transport processes are also carried out after each global deferment step (this is discussed further in 7.3.4). The global deferment step ensures that the time over which a particle is integrated is small, such that any linearisations have minimal effect on the solution. This also ensures that the computed jump rates remain close to that of the 'true' undeferred system.

Layering as a deferred process

Since layering is not strictly a linear process (the layering rate for each stochastic aggregate is a function of primary particle concentration), application of the LPDA to the layering processes described in (7.15)-(7.18) requires linearisation of the these equations. This is done by assuming that N_{pp} is approximately constant over the deferment time step. In the context of local deferment, this requires one to hold $N_{\text{pp}}(z)$ constant while all selected particles are integrated to the target time. In the context of global deferment steps, the assumption requires one to hold the $N_{\text{pp}}(z)$ constant across each integration interval Δt_{defer} (i.e. all particles are integrated using the same value of $N_{\text{pp}}(z)$ for each global deferment step and $N_{\text{pp}}(z)$ is updated between deferment steps). Such assumptions have been employed using LPDA to describe the surface growth of stochastic particles within the context of soot models [27]. Preliminary simulations with the twin-screw model confirmed that this assumption was appropriate, provided that a small enough deferment time step Δt_{defer} was enforced.

Primary particle update

As mentioned in the previous section, N_{pp} is assumed constant over the course of the deferment step and only updated at the end of each deferment step. These updates take different forms depending on the context in which the deferment is being applied. Let t_{target} denote the time at the end of the deferment step, then the possible forms of primary particle update are

1. Local Application

$$N_{\mathrm{pp}}(z,t_{\mathrm{target}}) \leftarrow N_{\mathrm{pp}}(z,t) - \frac{1}{v_{\mathrm{pp}}} \sum_{i=1}^{N_{\mathrm{p,jump}}} \left[s_{\mathrm{o}}(x_i)_{t_{\mathrm{target}}} - s_{\mathrm{o}}(x_i)_{t_{\mathrm{p}}} \right] w_i, \quad (7.61)$$

where $N_{\mathrm{p,jump}}$ is the number of particles involved in the selected jump process and the second term on the RHS represents the linearised SWA form of the final (layering) term in (7.2), taken over only the particle(s) involved in the local deferment. The derivation of this term is provided in Appendix A.2.

2. Global Application

$$\begin{aligned} N_{\mathrm{pp}}(z,t_{\mathrm{target}}) \leftarrow & N_{\mathrm{pp}}(z,t) \\ & - \frac{1}{v_{\mathrm{pp}}} \sum_{i=1}^{N_{\mathrm{agg}}(z,t)} \left[s_{\mathrm{o}}(x_i)_{t_{\mathrm{target}}} - s_{\mathrm{o}}(x_i)_{t} \right] w_i \\ & + (t - t_{\mathrm{target}}) \left. \frac{\mathrm{d}N_{\mathrm{pp}}(z,t)}{\mathrm{d}t} \right|_{\mathrm{transport}} \\ & + (t - t_{\mathrm{target}}) I^{\mathrm{nuc}}_{t,\mathrm{pp}}(z) V_{\mathrm{samp}}(z,t). \end{aligned} \quad (7.62)$$

The second term on the RHS of (7.62) is the same as the local case (7.61), except that the layering term has been integrated across the full ensemble of stochastic particles in compartment z. The third term on the RHS of (7.62) represents the integral of the linearised primary particle transport rate (Equation (7.30)), which, applied to the network of sample volumes, takes the form

$$\left. \frac{\mathrm{d}N_{\mathrm{pp}}(z,t)}{\mathrm{d}t} \right|_{\mathrm{transport}} = \begin{cases} \dfrac{\dot{m}_{\mathrm{feed}} V_{\mathrm{samp}}(z,t)}{V_{\mathrm{real}}(z) \rho_s v_{\mathrm{pp}}} - \dfrac{N_{\mathrm{pp}}(z,t)}{\tau(z)}, & \text{if } z = 1, \\ \dfrac{V_{\mathrm{real}}(z-1)}{V_{\mathrm{real}}(z)} \dfrac{V_{\mathrm{samp}}(z)}{V_{\mathrm{samp}}(z-1)} \dfrac{N_{\mathrm{pp}}(z-1,t)}{\tau(z-1)} & \\ \quad - \dfrac{N_{\mathrm{pp}}(z,t)}{\tau(z)}, & \text{otherwise.} \end{cases} \quad (7.63)$$

A full derivation of (7.63) is provided in Appendix A.3.

Finally, the last term in (7.62) is the integral of the nucleation depletion term (7.30), scaled according to the sample volume.

7.3.5 Solver implementation

One is primarily interested in the steady state solution of the twin-screw population balance problem described by Equations (7.1)-(7.2). As such, this permits one to solve the compartment network in a sequential manner, starting from $z = 1$ and moving along the network in a linear fashion until the final reactor with $z = \max \mathbb{L}$ is reached. This dramatically reduces the computational effort required to achieve converged solutions, to the extent that large-scale parameter estimation procedures become possible. Since the networks studied here are strictly linear (i.e. no back-flow or recycle loops), a single pass of the network is sufficient to fully converge the compartmental network. Algorithm 3 is a simplified account of the sequential solver algorithm used to solve the twin-screw population balance problem in this study. Preliminary twin-screw simulations using the model presented in this chapter showed that, if the initial state of each compartment (i.e. at $t = 0$) has an overall particle concentration that is sufficiently close to the solution of the population balance problem, then the simulation time required to reach steady state is determined by the residence time of the compartment in question. Again, the steady state solution of the population balance problem is defined as the state of the ensemble which does not exhibit any dynamic drift in the key measures (particle moments, overall mass density, mean porosity, liquid

Algorithm 2: The global deferment algorithm used to carry out continuous processes, applied to compartment z.

START
if $t == 0$ **then**
    Set $t_{\text{next-defer}} \leftarrow \Delta t_{\text{defer}}$.
while $t_{\text{next-defer}} < t$ **do**
    Integrate all aggregate particles to required time in stages.
    Set $t_{\text{target}} \leftarrow \min\{t_{\text{next-defer}}, t\}$.
    for $i = 1, N_{\text{agg}}(z,t)$ **do**
        Numerically integrate particle (x_i, w_i) to t_{target} according to Equation (7.29).
    Update $N_{\text{pp}}(z)$ to t_{target} according to (7.62).
    Set $t_{\text{next-defer}} \leftarrow t_{\text{next-defer}} + \Delta t_{\text{defer}}$.
STOP

content, etc.). Thus each compartment is solved to time

$$t_{\text{stop}}(z) = n_\tau \tau(z), \tag{7.64}$$

where $n_\tau \in \mathbb{R}^+$. The choice $n_\tau = 8$ was observed to yield simulation stop times that were long enough to reach steady state. Since the reactors are solved in sequence, the transport terms that have a dependence on the previous reactor (such as $N_{\text{agg}}(z-1,t)$) should be replaced with the equivalent steady state value (in this example $N_{\text{agg}}(z-1,t_{\text{stop}}(z-1))$).

Algorithm 3 is applied numerous times (each time with a different seed to the random number generator) in order to generate multiple independent measures of the steady state solution to the twin-screw population balance problem.

The first compartment is initialised such that 50% of the steady state mass hold-up is allocated to aggregate phase in the form of particles with $x = (v_{\text{drop}}, 0, 0, 0), w = 1$. The remaining mass specifies $N_{\text{pp}}(1,0)$. In each realisation, the first compartment is initialised with $N_{\text{agg}}(1,0) = 0.75 N_{\text{agg}}^{\max}$, where $N_{\text{agg}}^{\max}$ is the maximum number of computational particles permitted (per compartment). In all subsequent compartments, the particle ensemble and $N_{\text{pp}}(z,0)$ are initialised with the

Algorithm 3: The SWA sequential solver algorithm for a single realisation.

START
Set $z = 1$.
while $z \leq \max \mathbb{L}$ **do**
  Set $t \leftarrow 0$.
  Compute $t_{\text{stop}}(z)$ from (7.64).
  Initialise particle ensemble and $N_{\text{pp}}(z,0)$.
  while $t < t_{\text{stop}}(z)$ **do**
    Apply global deferment Algorithm (2).
    Compute $R_{\text{total}}^{\text{SWA}}(z,t)$ according to (4.6).
    Compute Δt_{wait} according to (4.5).
    Set $t \leftarrow t + \Delta t_{\text{wait}}$.
    Select jump process according to (4.7).
    Apply local deferment transformation D_t to the selected particle(s).
    Update the particle ensemble according to the selected jump process.
  Set $z \leftarrow z + 1$.
STOP

final state of particle ensemble and N_{pp} in the previous compartment $(z-1)$. The particle doubling and reduction procedures described in Lee et al. [96] are employed to control the number of computational particles in each compartment. Note that this is only important in the case of $z = 1$, since it is the only compartment where inflow and outflow processes are not directly coupled (the coagulation, breakage and non-droplet zone transport jump processes presented in Section 7.3.3 are all constant number).

7.4 Application of the new model

7.4.1 Twin-screw operating conditions

The predictive abilities of the twin-screw model are assessed using a two-step process. Firstly, unknown model parameters are estimated using data from selected experiments carried out by Vercruysse et al. [167]. In the second stage, these parameter estimates are used in the simulation of additional experiments by Vercruysse et al. [167], that were not featured in the estimation stage. In this experimental work, the authors investigated the effect of the screw configuration on the product particle size distribution (PSD) using a ConsiGma^{TM} twin-screw granulator (length-to-diameter ratio of 20:1) with α-lactose mono-hydrate as the feed material and distilled water as the binding liquid. The authors tested a large number of screw configurations with slight permutations in the number of specific element types, number of blocks (i.e groups of the same element type) of certain element types, with all other controllable operating conditions fixed. In order to better understand the role of the most common element types (conveying and kneading), only screw configurations that consisted of a combination of kneading and conveying elements (and for which product PSD were presented) were simulated. The simulated screw configurations and their corresponding compartmental representations are outlined in Figure 7.4. Details of the model parameters corresponding to the experimental conditions in Vercruysse et al. [167] are presented in Table 7.1.

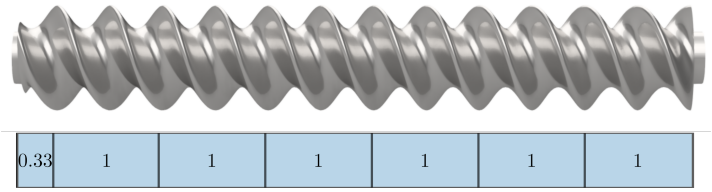

(a) CE

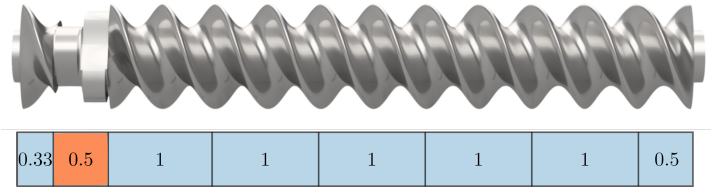

(b) 2KE

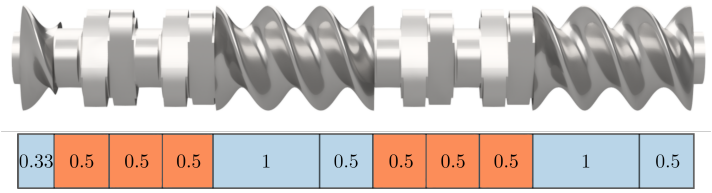

(c) 2x6KE

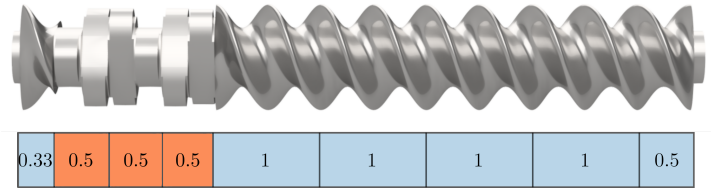

(d) 6KE

Fig. 7.4 Screw configurations modelled in this work and their respective compartmental representations. The number in the centre of each compartment represents the compartment length (normalised by the screw diameter). Compartments representing conveying zones are in blue and compartments representing kneading zones are shown in orange. These correspond to configurations A, B, D and E in Vercruysse et al. [167]

Table 7.1 Un-optimised model inputs.

Parameter (symbol)	Type	Value	Unit
Liquid:solid mass feed ratio (LSR)	Operating parameter	0.09	-
Mass feed rate ($\dot{m}_{\text{feed}}$)	Operating parameter	20.0	kg hr^{-1}
Screw speed (n_{screw})	Operating parameter	13.33	rev s^{-1}
Screw residence time (τ_{screw}) (CE,2KE,6KE,2x6KE) [88]	Operating parameter (interpolated)	0.753, 3.02, 3.09, 4.52	s
Liquid addition nozzle diameter (d_{nozzle})	Equipment geometry	1.6	mm
Screw diameter (D)	Equipment geometry	25	mm
Specific available volume CE (v_{convey})	Equipment geometry	1.218×10^{-5}	m^3/D
Specific available volume KE (v_{knead})	Equipment geometry	1.284×10^{-5}	m^3/D
Coefficient of restitution (e_{coag}) [111]	Material property	0.2	-
Liquid binder viscosity (μ)	Material property	10^{-3}	Pa s
Liquid binder density (ρ_{l})	Material property	998	kg m^{-3}
Solid original density (ρ_{s})[176]	Material property	1545	kg m^{-3}
Height of surface asperities (h_{a})	Material property (estimated)	5×10^{-6}	m
Representative volume mean primary particle diameter d_{pp}	Material property	27.3	μm
Droplet diameter (d_{drop})	Model parameter	1.6	mm
Minimum particle size for breakage ($v^{\text{min}}_{\text{parent}}$)	Model parameter	27.3	μm
Daughter distribution parameter 1 (α_{daughter}) (CE,KE)	Model parameter	0.5, 2.0	-
Daughter distribution parameter 2 (β_{daughter}) (CE,KE)	Model parameter	0.5, 2.0	-
Minimum particle porosity (ε_{min})	Model parameter	0.3	-
Particle bed packing fraction (ε_{bed})	Model parameter	0.3	-
Pore saturation limit for nucleation (s^*)	Model parameter	0.12	-

7.4.2 Simulation conditions

All simulations were carried out using the numerical inputs given in Table 7.2 on a single core of an Intel® Sandy Bridge™ E5-2670 3.30GHz Processor with 4GB of RAM per core. Temporal function averages and confidence intervals are computed in the same manner as that described in Chapter 5, Section 5.3.

Table 7.2 Numerical input parameters.

Parameter	Value	Unit
$N_{\text{agg}}^{\text{max}}$	512	-
Δt_{defer}	10^{-4}	s
n_{run}	10	-
n_{τ}	8	-
k_{maj}	1.42	-

7.4.3 Parameter estimation

In this work, compartments with the same element type (conveying, kneading) are asserted to have the same process rate constants (4 for each element type, 8 in total), regardless of position. In this way, a central screw element library can be used to store element specific rate constants. This library can then be accessed to retrieve and define the rate constants for each compartment in an representation of arbitrary screw configurations. Using this framework, the model can be calibrated against experimental data through the optimisation of the relevant variables in the screw element library. The procedure for optimising each of the variables within the screw element library follows that described in Chapter 5, Section 5.4. The rate constants are fitted against experimental mass-based percentile data [167] corresponding to screw configurations CE, 2KE and 2x6KE (see Figure 7.4) using the parameter bounds in Table 7.3. Screw configuration 6KE is then used to measure the predictive power of the model.

7.5 Model results

The set of model parameters with the lowest objective function value (found through the optimisation procedure) are presented in Table 7.4. The associated mass fraction distributions for this parameter set are displayed, firstly, for screw

Table 7.3 Bounds used for optimisation of model parameters.

	Conveying		Kneading			
Parameter	Lower	Upper	Lower	Upper	Scaling	Unit
k_{col}	10^{-10}	5×10^{-8}	10^{-10}	2×10^{-8}	Logarithmic	$\text{m}^{\frac{5}{2}}$
k_{comp}	10^{-2}	2.0	10^{-2}	2.0	Logarithmic	-
k_{att}	1.68×10^{-2}	8.4	1.68×10^{-3}	0.0168	Logarithmic	s
ω_{att}	10^{-2}	0.2	5×10^{-2}	0.6	Linear	-

Table 7.4 Optimised model rate constants.

Parameter	Conveying	Kneading	Unit
k_{col}	10^{-10}	2.0×10^{-8}	$\text{m}^{\frac{5}{2}}$
k_{comp}	0.01	0.475	-
k_{att}	0.0168	9.358×10^{-3}	s
ω_{att}	0.1095	0.387	-

configurations used in the optimisation procedure in Figure 7.5, and secondly, for the 'new' 6KE screw configuration (depicted in Figure 7.4(c)) in Figure 7.6.

Note that the model has qualitatively captured the experimental trend in which the amount of fines (defined here as particles in the smallest sieve class) reduces with an increasing number of kneading elements. This is expected, since the kneading elements serve to distribute the binding liquid across the body of solid material passing through the element, thereby promoting particle growth. Though the model has captured this trend, the degree of primary particle consumption is under-predicted for all screw configuration tested - though this is minimal in the 2x6KE case. This not surprising, since a very simplistic layering mechanism was employed in this work. Within the model, the degree of layering is strongly controlled by the amount of surface liquid present on agglomerates, however, the amount of surface liquid that should be consumed by layering is unclear and hence a very basic model has been used. Implementation of more complex models in the future would require experimental data on the layering dynamics in isolation from other twin-screw processes.

In terms of breakage processes, the model has under-predicted the production of particles in the size range 200-1000μm in screw elements with a high number of conveying elements. This is an indication that the breakage parameters that generate this distribution (daughter distribution shape parameters α_{daughter}, β_{daughter} and breakage exponent ω_{att}) may need to be revisited. As previously discussed,

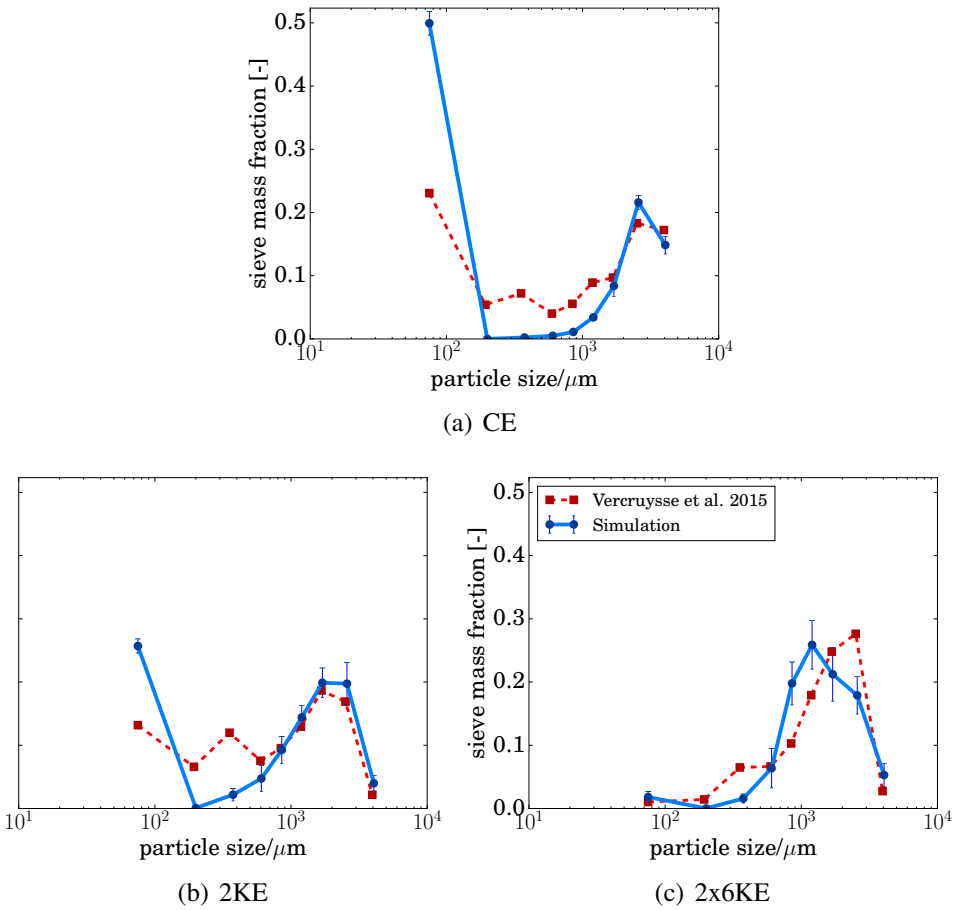

(a) CE

(b) 2KE

(c) 2x6KE

Fig. 7.5 A comparison of the optimised model particle size distributions in the final compartment against the experimental results from Vercruysse et al. [167] for different screw configurations.

the daughter distribution parameters used for conveying elements in this work were selected to qualitatively capture the cutting and edge chipping effects that were experimentally observed in such elements. Since these parameters were not fitted within this study, it is likely that these parameters would benefit from further investigation. This would merit a modelling investigation in its own right and is not pursued further here.

It is noted that the compaction, breakage and coagulation processes have all been pushed to their lower bound as a result of the optimisation process. This indicates that the majority of the model particle processes occurred in the kneading elements. The bounds of these conveying parameters were not reduced further, since the effect on the results was deemed to be minimal. Note that the kneading element collision rate has also been pushed to its upper bound in the parameter estimation process, bringing the total number parameters at their bounds to four.

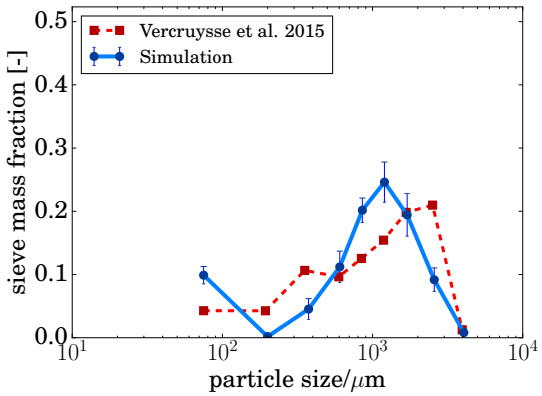

Fig. 7.6 A comparison of simulated and experimental results (Vercruysse et al. [167]) using optimised model rate constants for a 6KE screw configuration (not used in the optimisation stage).

This result is likely a combination of a number of factors. Firstly, even though the 'best' Sobol point identified in the first stage of the parameter estimation may be well within the bounds of the space, the additional Hooke-Jeeves local optimisation stage on these points often pushes one or more parameters to their bounds. Due to the high computational cost of the combined stages, it is computationally prohibitive to iterate this process any significant number of times to ensure that the bounds yield both particle evolutions that both plausible and that all optimised parameters lie within their bounds. All of the parameters that have hit their lower limit are associated with the conveying zone. This is likely due to the lower residence time in the conveying zone associated with the conveying zone relative the kneading elements. It should also be noted that the configuration of kneading elements in the screw configuration modelled (Figure 7.4) are not angled at 90^o to each other. This means that they will have some conveying capacity and hence will not be completely filled with material as assumed in the residence time model. Taking this in account would reduce the kneading element residence time estimates and thereby increase the residence times estimates for the conveying zones. Alternatively, to ensure parameters in the conveying zone carry more weight in the optimisation process, mid-barrel PSD data would need to be measured and integrated into the objective function of the optimisation process. At the moment, only the final distribution is in this process, which can lead to un-physical particle evolutions or concentration of particle processes in distinct sections, as observed here.

The evolution of the particle size distribution along the compartmental networks is shown for the 2x6KE screw configuration in Figure 7.7. The nucleation zone consists of a mixture of over-sized agglomerates and primary particle mass.

Upon entering the first kneading compartment ($z = 2$) these large agglomerates are broken down and consolidated. The consolidation process has resulted in the squeezing of internal liquid to the particle surface which has promoted consumption of fines through layering. This trend continues through the second and third kneading compartment. It is clear from the results there is little change in the granular mass as it passes through the central conveying section ($z = \{6,7\}$). Only a minimal degree of breakage is observed in this zone, and, as discussed in the previous paragraph, the absence of the expected increase in intermediate size classes (200-400μm) for the 2x6KE simulation indicates that the daughter distribution of these elements requires further investigation. Almost all of the remaining fines are consumed within the second kneading section of the compartment network.

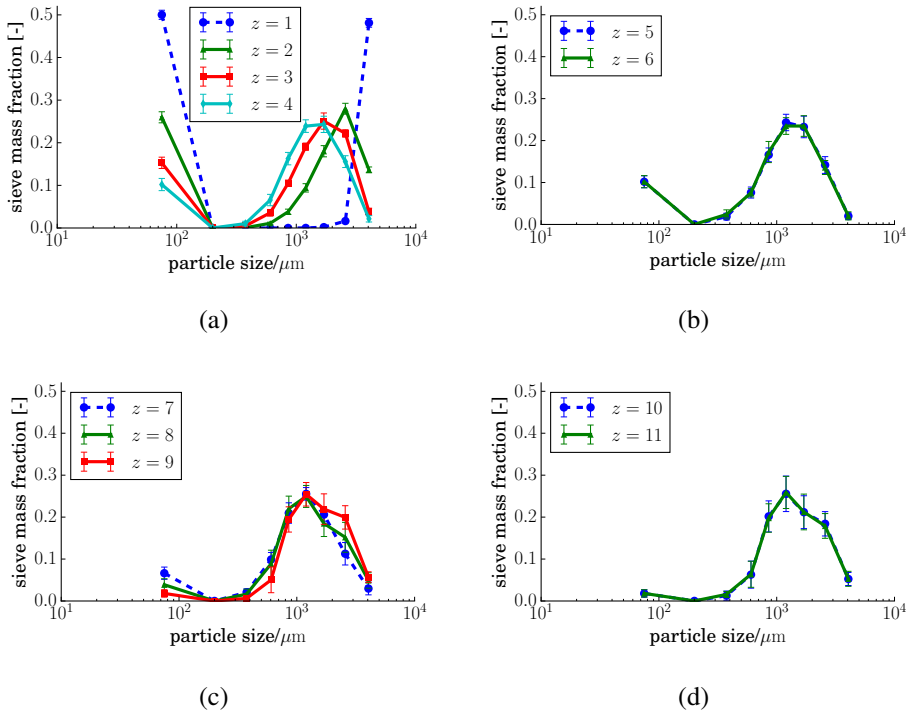

Fig. 7.7 Particle size distribution evolution along the compartment network for the 2x6KE screw configuration. Element types by compartment index: conveying $z = \{1,5,6,10,11\}$, kneading $z = \{2,3,4,7,8,9\}$.

In order to further assess the quality of the model, the evolution of the agglomerate particle composition along the screw barrel for each simulated screw configuration is presented in Figure 7.8. The associated mass fraction of fines at each of the these barrel positions, in each screw configuration, is shown in Figure 7.9. From Figure 7.8 it is observed that, for the conveying elements, a

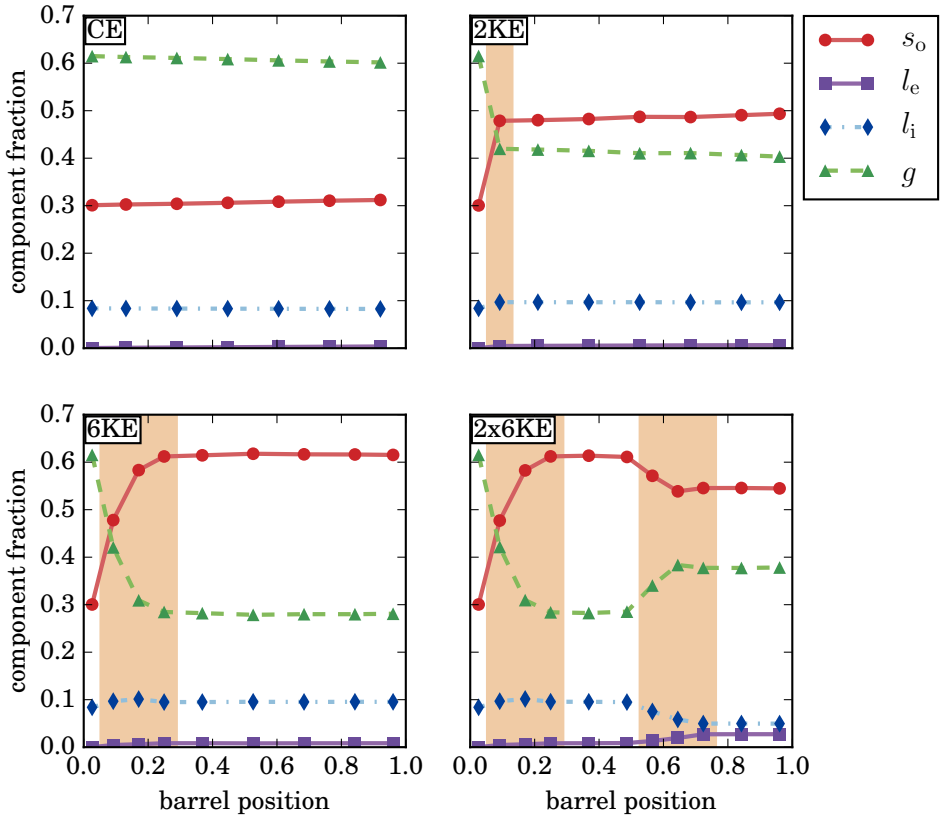

Fig. 7.8 Mass-averaged aggregate particle composition evolutions (by volume) along the barrel length for each screw configuration simulated. s_o represents original solid, l_e represents external liquid, l_i represents internal liquid and g is gas. Kneading zones are highlighted in orange. Data points are placed according to the centre of the associated compartment. Barrel positions correspond to the variation zone and are expressed as a normalised length.

slight degree of particle compaction has reduced the porosity of large agglomerate particles, which resulted in the complementary increase in solid volume fraction. Though the solid volume fraction increase could be attributed to particle growth through layering or coagulation, the minimal fines consumption for the CE configuration in Figure 7.9 and the abundance of surface liquid in Figure 7.8 (which should promote aggregate coagulation if the collision rate is sufficiently high) demonstrates that this is almost purely the result of aggregate compaction. In all configurations with a kneading zone, it is observed that, for the first kneading zone, aggregate particles acquire solid mass though the consolidation of highly porous agglomerates. This consolidation has replenished surface liquid levels, which promoted layering of primary particles and coalescence of surface wet agglomerates. This decrease in surface liquid observed in Figure 7.8 is a consequence of the internalisation of liquid present in both the aggregate

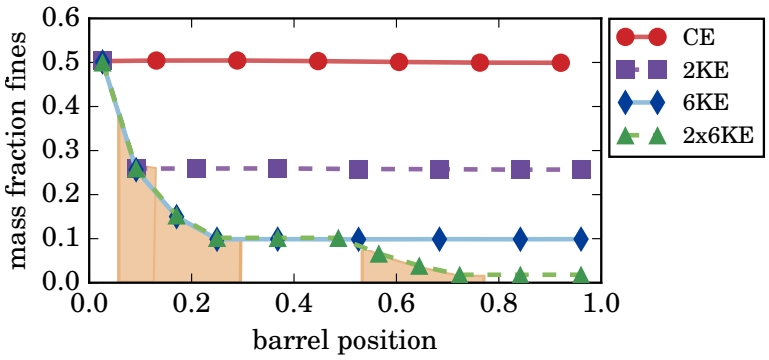

Fig. 7.9 Simulated evolution of the mass fraction of fines (d < 75μm) along the length of the barrel for all screw configurations tested. Data points are placed according to the centre of the associated compartment. Barrel positions correspond to the variation zone and are expressed as a normalised length. Kneading zones are highlighted in orange.

consolidation and primary particle layering mechanisms of the model. This raises an interesting point - though several experimental studies [38, 47, 152, 167, 168] have concluded that kneading elements squeeze liquid to the surface of large agglomerates, promoting further growth, it is generally not understood if this growth takes place within the kneading element, or further down the barrel in conveying zones. From Figure 7.9, the model in this work would seem to indicate that the majority of this growth and fines reduction occurs within the kneading blocks.

An interesting feature that is observed in particle evolution of the 2x6KE screw configuration is the increase in gas volume fraction within the second kneading block. This occurred as the result of aggregate coalescence - which, according to the coalescence model of Braumann et al. [19] used in this work, results in the generation of trapped pore volume as aggregates coalesce. Though trapping of such 'new' pore volume may occur, it is expected that a net reduction in porosity would be observed across this kneading block (as is the case in the first kneading block of all screw configurations tested). Thus, the competition between the consolidation forces and pore volume creation through coalescence would be an area of investigation in future modelling efforts.

7.6 Chapter conclusions

In this chapter, the twin-screw granulation model presented in Chapter 3 has been further developed through the enhancement and augmentation of the existing

particle process models and the addition of a new layering mechanism. In order to estimate compartmental residence times for use within this model, a novel procedure was developed to infer this parameter based on the type of screw element associated with each compartment. A stochastic particle framework for the simulation of the aggregate particle phase of the granulation system was presented and coupled to an ODE solver in order to simulate the dynamics of the primary particle population and carry out continuous aggregate particle processes. Model parameters specific to different types of screw element were calibrated through simulation of systems with a number of different screw configurations and comparison with an existing experimental data set. The model was observed to qualitatively capture the reduction in the mass fraction of fines in the granular product as the number of kneading elements was increased. The element specific breakage model and the drying dynamics of the layering process were identified as key areas for future model refinement.

Chapter 8

Conclusions of this thesis

8.1 Conclusions from the work done

This thesis concerned the development of a population balance model for twin-screw granulation and a numerical framework with which to simulate the model. The literature indicated that the prevalence and nature of particle mechanisms in the twin-screw device were a strong function of the local screw element geometry. This feature necessitated the use of a modular modelling approach. The literature also indicated that previous twin-screw modelling efforts were restricted in their complexity due to the sectional method employed in their solution. As such, a stochastic, compartmental population balance approach was selected as the most suitable modelling framework. Further to this, the presence of so called 'rare' events (such as large droplet inception) motivated the use of the more versatile SWA variant of the stochastic particle method.

A new twin-screw model with a four dimensional particle type-space was presented in Chapter 3. This model incorporated sub-models for immersion nucleation, coagulation, consolidation, fragmentation, liquid penetration and transport mechanisms, each of which was described in detail. In Chapter 5, the model was demonstrated to capture the promotion of particle growth with increasing liquid feed rates to the twin-screw device. Particle size evolutions along the compartmental network indicated the model's ability to capture the liquid distributing effect of kneading elements. The highly-bimodal distribution of all the results gathered showed that the size independent collision kernel employed did not promote sufficient interaction between large agglomerates and the mass of primary particles. This indicated the need for a layering mechanism and more

complex collision kernel. The persistent bimodality of the product distributions also indicated that the breakage kernel employed may need to be substituted with a more complex kernel.

In Chapter 4, a SWA framework for the simulation of the new twin-screw model was presented. This included a new interpretation of the twin-screw immersion nucleation process as a stochastic jump event. The numerical properties of this framework were investigated in Chapter 6. It was demonstrated that the statistical weight of droplet particles could be selected to ensure optimum sampling of this jump process. The uniform weighting of incepted particles was demonstrated to place an effective lower bound on the number of computational particles that were required for simulation with acceptable levels of variance in the simulated mass fraction distributions. To combat this, a variable weighted inception algorithm for SWA (VWI-SWA) was rigorously formulated for the first time. VWI-SWA was demonstrated to permit much lower numbers of computational particles and, in doing so, reduce the computational cost of simulation by almost two orders of magnitude for a fixed variance level.

To address the model deficiencies identified in Chapter 5, the model was extended in Chapter 7 to include a size-dependent collision kernel. To address the prohibitively expensive simulation of the interaction between primary particles and large aggregate, the primary particles were represented as a mono-disperse concentration phase with their own population balance. The resulting aggregate and primary particle population balances were coupled using the LPDA and a primary particle layering mechanism, new breakage model and compartmental residence time model were incorporated into the overall twin-screw model. The enhanced model was shown to mitigate the interaction issues observed in Chapter 5 and demonstrated the ability to capture changes in particle morphology associated with different screw element configurations.

8.2 Recommendations for future work

The extended twin-screw model of Chapter 7 leaves a number avenues for mechanism refinement and investigation. The most obvious of which is the breakage kernel. As discussed in Chapter 7, the daughter distribution parameters of each element type have been selected to quantitatively capture the varying breakage dynamics between screw element types. Note that the overall breakage dynamics are a function not only of the daughter distribution, but also of the

breakage rate constants k_{att} and exponent ω_{break}. As such, an investigation would need to be carried out on sets of these model parameters in order to establish reasonable bounds for each common screw element type, using experimental particle breakage data. These bounds could then be used to aid future model calibration.

Another avenue for model refinement is the formulation of a more detailed, physical layering model. Experimental and theoretical investigation of the drying dynamics of the primary particle layering process is of particular importance, since the availability of surface liquid strongly affects the rate of particle growth. It is noted that the primary particle representation of Chapter 7 was mono-disperse, however, the framework could be readily extended to support arbitrary primary particle size distributions. Such an extension would increase the number of potential use cases for the the model. This limitation currently prevents the model of Chapter 7 being used in the simulation of the El Hagrasy et al. [46] experiments used in previous chapters. In El Hagrasy et al. [46], the width of the primary particle size distribution for the Impalpable lactose grade is significantly larger than that of the α-lactose mono-hydrate 200M used in the experiments of Vercruysse et al. [167] (820μm vs. 120μm)[1], featured in Chapter 7. This means that the mono-disperse assumption currently made in the construction of the Chapter 7 model is likely invalid for the Impalpable grade. In addition to these model adaptions, the residence time prediction algorithm of Chapter 7 could be refined. At the moment, it is assumed that all elements of the same type have the same fill level, and hence the same residence time. As mentioned, in reality, this is not quite the case, since conveying elements that precede a non-conveying block (such as kneading block) tend to fill to a higher degree - generating the back pressure required to force material through the non-conveying elements. A simplistic model for this back pressure could be employed to account for this fill level and the associated residence time gradient.

The difficulties presented in the calibration of the models in Chapter 5 and 7 highlight the need to train the model on experimental data corresponding to several sampling points along the variation zone of twin-screw devices. This would ensure that generation of unphysical particle evolutions could be avoided. The models of this work would also need to be verified against experimental porosity data where available.

[1]Note: the primary PSD width of α-lactose mono-hydrate 200M used by Vercruysse et al. [167] was assumed to be similar to that provided [Meggle] for GranuLac 200 (also lactose mono-hydrate) as the equivalent data was not available from the supplier stated by Vercruysse et al. [167] (Caldic, Hemiksem, Belgium) at the time of writing.

In addition to the areas for model refinement discussed above, a number of directions remain for the refinement of the numerical framework presented, and its associated algorithmic implementation. The following adaptions have the potential to reduce the computational cost of simulation for a fixed level of systematic and statistical error in the solution. First of these is the reformulation of the deferment process of Chapter 7, which is currently the most time-consuming process in the solver. This is a direct consequence of the need to assume that the primary particle concentration is constant over the deferment step. This is currently ensured by using very small deferment time steps, which comes at significant computational cost. In practice, the need for this assumption could be eliminated by adapting and implementing the predictor corrector framework of Celnik et al. [28]. A second area where computational speed-up could be gained is the steady state solver implementation. Though the solver developed in Chapter 7 reduced the overall cost of simulation, it would benefit from further refinement in order to mitigate the increasing variance in the PSDs observed as the number of model compartments in increased.

Nomenclature[2]

Upper-case Roman

B	breakage fragment probability distribution	-
C	collision rate function	$\mathrm{m}^{\frac{1}{2}}$
D	screw diameter	mm
$\mathbb{D}$	set of all particle diameters	-
$\mathbb{D}_{\mathrm{incept}}$	set of all particle diameters for inception species	-
D_t	deferment function	-
$\tilde{D}_t$	weighted deferment function	-
F	particle breakage kernel	s^{-1}
F_{c}	transport scaling factor	-
I_{drop}	droplet particle inception rate	$\mathrm{s}^{-1}\mathrm{m}^{-3}$
$I_{\mathrm{drop}}^{\mathrm{SWA}}$	weighted droplet particle inception rate	$\mathrm{s}^{-1}\mathrm{m}^{-3}$
$I_{\mathrm{nuc,pp}}$	primary particle depletion sink term (nucleation)	$\mathrm{s}^{-1}\mathrm{m}^{-3}$
I_{solid}	particle inception rate	$\mathrm{s}^{-1}\mathrm{m}^{-3}$
$I_{\mathrm{solid}}^{\mathrm{SWA}}$	weighted particle inception rate	$\mathrm{s}^{-1}\mathrm{m}^{-3}$
$I_{\mathrm{trans,pp}}$	primary particle depletion source term (transport)	$\mathrm{s}^{-1}\mathrm{m}^{-3}$
K_{coag}	coagulation kernel	$\mathrm{m}^3\mathrm{s}^{-1}$
$K_{\mathrm{coag}}^{\mathrm{SWA}}$	SWA coagulation kernel	$\mathrm{m}^3\mathrm{s}^{-1}$
K_{col}	collision kernel	$\mathrm{m}^3\mathrm{s}^{-1}$
$K_{\mathrm{col}}^{\mathrm{SWA}}$	SWA collision kernel	$\mathrm{m}^3\mathrm{s}^{-1}$
$\hat{K}_{\mathrm{col}}^{\mathrm{SWA}}$	SWA majorant collision kernel	$\mathrm{m}^3\mathrm{s}^{-1}$
K_{nuc}	nucleation kernel	$\mathrm{m}^3\mathrm{s}^{-1}$
$\tilde{K}_{\mathrm{nuc}}^{\mathrm{SWA}}$	weighted majorant nucleation kernel	$\mathrm{m}^3\mathrm{s}^{-1}$
K_{w}	inception rate constant	-
$L_{\mathrm{j,e}}$	length of screws section consisting of element type e in zone j	D

[2]Note: for parameters which have more than a single associated unit, the first unit should be interpreted as that related to the model of Chapters 3 - 6. The second unit should be interpreted as that associated with the augmented model description in Chapter 7. A single unit indicates that the dimensions of the associated parameter is the same across all chapters of this thesis.

$\mathbb{L}$	set of all compartment indices	-
M_{metering}	dynamics mass hold up in screw metering zone	kg
$M_{\text{variation}}$	dynamics mass hold up in screw variation zone	kg
N	number of computational particles	-
N_{agg}	number of aggregate/computational particles	-
$N_{\text{agg}}^{\text{max}}$	maximum number of aggregate/computational particles	-
N_{max}	maximum number of computational particles	-
N_{pp}	Number of primary particles	-
OF	objective function	-
$\mathbb{P}_{\text{accept}}$	majorant acceptance probability	-
Q	extended particle concentration measure	m^{-3}
$\tilde{R}$	harmonic mean particle radius	m
$R_{\text{break}}^{\text{SWA}}$	total SWA breakage jump rate	s^{-1}
$R_{\text{coag}}^{\text{SWA}}$	total SWA coagulation jump rate	s^{-1}
R_{drop}	total droplet addition rate	s^{-1}
$R_{\text{incept}}^{\text{SWA}}$	total SWA inception jump rate	s^{-1}
R_{nuc}	total nucleation rate	s^{-1}
$R_{\text{nuc}}^{\text{SWA}}$	total SWA nucleation jump rate	s^{-1}
$R_{\text{outflow,agg}}$	total aggregate outflow rate	s^{-1}
R_{pore}	pore radius	m
$R_{\text{total}}^{\text{SWA}}$	total SWA total jump rate	s^{-1}
$R_{\text{trans}}^{\text{SWA}}$	total SWA transport jump rate	s^{-1}
St_{v}	viscous Stokes number	-
St_{v}^{*}	critical Stokes number	-
T_{break}	breakage operator	-
T_{coag}	coagulation type transformation	-
T_{comp}	compaction type transformation	-
T_{nuc}	nucleation type transformation	-
U_{col}	particle collision velocity	m
$\dot{V}_l$	liquid flowrate	m^3s^{-1}
V_{real}	physical volume of compartment occupied	m^3
V_{samp}	sample volume	m^3
$\mathbb{W}$	set of all particle weights	-
$\mathbb{X}$	particle type-space	-

$\mathbb{X}_{\text{agg}}$	aggregate type-space	-
$\mathbb{X}_{\text{incept}}$	inception particle type-space	-
$\mathbb{X}_{\text{nuc}}$	nuclei type-space	-
$\mathbb{X}_{\text{pp}}$	primary particle type-space	-

Lower-case Roman

a_{surf}	particle external surface area	m^2
c	particle concentration	m^{-3}
c	confidence interval width	-
c_{pp}	primary particle concentration measure	m^{-3}
d	particle diameter	m
d_{max}	maximum inception particle diameter	m
d_{min}	minimum inception particle diameter	m
d_{nozzle}	liquid injection nozzle diameter	m
d_{pp}	primary particle diameter	m
e_{coag}	material coefficient of restitution	-
f_{frag}	breakage fragment size parameter	-
$f_{\text{j,e}}$	volumetric fill fraction of screw section with element type e in zone j	-
f_{succ}	collision success indicator	-
g	particle internal gas volume	m^3
g_{break}	particle breakage frequency	s^{-1}
h_{a}	height of surface asperities	m
h_{l}	height of external liquid layer	m
$\tilde{h}_{\text{l}}$	harmonic mean height of external liquid layer	m
k_{att}	attrition rate constant	s m^{-3}, s
k_{col}	collision rate constant	m^3, $\text{m}^{\frac{5}{2}}$
k_{comp}	compaction rate constant	-
k_{maj}	majorant scaling factor	-
k_{nuc}	nucleation rate constant	s^{-1}
k_{pen}	liquid penetration rate constant	$\text{kg}^{\frac{1}{2}}\text{m}^{-\frac{7}{2}}\text{s}^{-\frac{3}{2}}$
l_{e}	external liquid volume	m^3
$l_{\text{e}\to\text{i}}$	amount of surface liquid internalised	m^3
l_{i}	internal liquid volume	m^3

m	particle mass	kg
$\tilde{m}$	harmonic mean particle mass	kg
$\dot{m}_{\text{feed}}$	operating mass feed rate	kg s^{-1}
n	particle number concentration	m^{-3}
n_{run}	number of simulation realisations	-
n_{screw}	screw speed	rev s^{-1}
n_τ	simulation stop time parameter	-
p	pore volume	m^3
q_0	inception particle distribution on $\mathbb{D}$	m^{-1}
q_0^{SWA}	weighted inception particle distribution on $\mathbb{D}$	m^{-1}
$q_{0,\mathbb{X}_{\text{incept}}}$	inception distribution on $\mathbb{X}_{\text{incept}}$	m^{-3}
$q_{0,\mathbb{X}_{\text{incept}}}^{\text{SWA}}$	weighted inception distribution on $\mathbb{X}_{\text{incept}}$	m^{-3}
r_{drop}	radius of droplet footprint	m
r_{inflow}	single particle inflow rate	s^{-1}
r_{layer}	rate of primary particle layering onto agglomerate particle	s^{-1}
s^*	pore saturation limit	-
s_{o}	original solid volume	m^3
s_{r}	Braumann model reacted solid volume	m^3
t	time	s
t_{p}	particle current time	s
t_{stop}	simulation stop time	s
t_{target}	deferment stop time	s
Δt_{defer}	deferment time step	s
Δt_{wait}	jump waiting time	s
v	particle volume	m^3
$\hat{v}_{\text{break}}$	breakage normalisation parameter	m^3
$v_{\text{max}}^{\text{nuc}}$	maximum particle size for nucleation	-
$v_{\text{parent}}^{\text{min}}$	minimum volume for breakage	m^3
v_{pp}	primary particle volume	m^3
v_y	breakage daughter volume function	m^3
w	particle statistical weight	-
w_{drop}	droplet statistical weight	-
w_{incept}	particle inception weight	-
w_{max}	maximum particle statistical weight	-

w_{nuc}	nuclei particle statistical weight	-
x	particle vector	m^3
x_{drop}	droplet particle vector	m^3
x_{nuc}	nuclei particle vector	m^3
x_{pp}	primary particle vector	m^3
y	breakage fragment particle vector	m^3
z	compartment index	-

Greek

α_{daughter}	breakage daughter distribution shape factor	-
β_{daughter}	breakage daughter distribution shape factor	-
γ_{coag}	coagulation weight transfer function	-
γ_{frag}	breakage weight transfer function	-
γ_{nuc}	nucleation weight transform	-
γ_{LV}	binder surface tension	N m^{-1}
δ_i	Dirac delta function centred on i	-
ε	particle porosity	-
ε_{bed}	particle bed packing fraction	-
$\varepsilon_{\text{surf}}$	surface porosity	-
θ	solid-liquid contact angle	rad
λ	aggregate particle concentration measure	m^{-3}
μ	binder viscosity	Pa s
v_{convey}	specific volume available in conveying elements	m^3/D
v_{knead}	specific volume available in kneading elements	m^3/D
ρ_{eff}	effective density of the solid material in the variation zone	kg m^{-3}
ρ_{l}	binder density	kg m^{-3}
ρ_{s}	solid density	kg m^{-3}
σ	objective function weighting factor	μm
τ	compartment residence time	s
τ_{metering}	metering zone screw residence time	s
τ_{pen}	droplet penetration time	s
τ_{screw}	total mean screw residence time	s
$\tau_{\text{variation}}$	variation zone screw residence time	s
φ	test function	-

ϕ_{max}	maximum liquid saturation	-
χ_{frag}	breakage fragment size parameter	-
ψ	test function for SWA	-
ω_{att}	breakage rate exponent	-

Abbreviations

ANN	artificial neural network
API	active pharmaceutical ingredient
CE	conveying element
CFD	computational fluid dynamics
DEM	discrete element method
DME	distributive mixing element
DSMC	direct simulation Monte Carlo
EWI-SWA	equi-weighted inception scheme for the stochastic weighted algorithm
HPC	hydroxypropylcellulose
HPS	high precision solution
KE	kneading element
LPDA	linear process deferment algorithm
LSR	liquid-solid mass feed ratio
MC	Monte Carlo
MC-PBM	Monte Carlo population balance model
ODE	ordinary differential equation
PBE	population balance equation
PBM	population balance model
PEPT	positron emission particle tracking
PSD	particle size distribution
QbD	quality by design
QbT	quality by testing
SPM	stochastic particle method
SSE	sum of square errors
SWA	stochastic weighted algorithm
TSG	twin-screw granulation
VWI-SWA	variable weighted inception scheme for the stochastic weighted algorithm

References

[1] Ai, Q., Dhenge, R. M., Hounslow, M. J., and Salman, A. D. (2016). Developing a miniaturized approach for formulation development using twin screw granulation. Powder Technology, 300:83 – 91.

[2] Allen, T. (2013). Particle size measurement. Springer.

[3] Alopaeus, V., Laakkonen, M., and Aittamaa, J. (2006). Numerical solution of moment-transformed population balance equation with fixed quadrature points. Chemical Engineering Science, 61(15):4919 – 4929.

[4] Austin, L. G. (2002). A treatment of impact breakage of particles. Powder technology, 126(1):85–90.

[5] Balthasar, M. and Kraft, M. (2003). A stochastic approach to calculate the particle size distribution function of soot particles in laminar premixed flames. Combustion and Flame, 133(3):289 – 298.

[6] Barrasso, D. (2015). Multi-scale modelling of wet granulation processes. PhD dissertation, Rutgers, The State University of New Jersey.

[7] Barrasso, D., El Hagrasy, A., Litster, J. D., and Ramachandran, R. (2015a). Multi-dimensional population balance model development and validation for a twin screw granulation process. Powder Technology, 270, Part B:612 – 621.

[8] Barrasso, D., Eppinger, T., Pereira, F. E., Aglave, R., Debus, K., Bermingham, S. K., and Ramachandran, R. (2015b). A multi-scale, mechanistic model of a wet granulation process using a novel bi-directional PBM–DEM coupling algorithm. Chemical Engineering Science, 123:500–513.

[9] Barrasso, D., Eppinger, T., Pereira, F. E., Aglave, R., Debus, K., Bermingham, S. K., and Ramachandran, R. (2015c). A multi-scale, mechanistic model of a wet granulation process using a novel bi-directional PBM-DEM coupling algorithm. Chemical Engineering Science, 123:500 – 513.

[10] Barrasso, D. and Ramachandran, R. (2012). A comparison of model order reduction techniques for a four-dimensional population balance model describing multi-component wet granulation processes. Chemical Engineering Science, 80:380 – 392.

[11] Barrasso, D. and Ramachandran, R. (2015). Multi-scale modeling of granulation processes: Bi-directional coupling of {PBM} with {DEM} via collision frequencies. Chemical Engineering Research and Design, 93:304 – 317.

[12] Barrasso, D. and Ramachandran, R. (2016). Qualitative assessment of a multi-scale, compartmental PBM-DEM model of a continuous twin-screw wet granulation process. Journal of Pharmaceutical Innovation, 11(3):231–249.

[13] Barrasso, D., Tamrakar, A., and Ramachandran, R. (2014). A reduced order PBM–ANN model of a multi-scale PBM–DEM description of a wet granulation process. Chemical Engineering Science, 119:319–329.

[14] Barrasso, D., Tamrakar, A., and Ramachandran, R. (2015d). Model order reduction of a multi-scale PBM-DEM description of a wet granulation process via ANN. Procedia Engineering, 102(Supplement C):1295 – 1304.

[15] Barrasso, D., Walia, S., and Ramachandran, R. (2013). Multi-component population balance modeling of continuous granulation processes: A parametric study and comparison with experimental trends. Powder Technology, 241:85 – 97.

[16] Boje, A., Akroyd, J., Sutcliffe, S., Edwards, J., and Kraft, M. (2017). Detailed population balance modelling of TiO2 synthesis in an industrial reactor. Chemical Engineering Science, 164:219 – 231.

[17] Bouffard, J., Bertrand, F., and Chaouki, J. (2012). A multiscale model for the simulation of granulation in rotor-based equipment. Chemical Engineering Science, 81:106 – 117.

[18] Bratley, P. and Fox, B. L. (1988). Algorithm 659: Implementing Sobol's quasirandom sequence generator. ACM Transactions on Mathematical Software, 14(1):88–100.

[19] Braumann, A., Goodson, M. J., Kraft, M., and Mort, P. R. (2007). Modelling and validation of granulation with heterogeneous binder dispersion and chemical reaction. Chemical Engineering Science, 62(17):4717 – 4728.

[20] Braumann, A. and Kraft, M. (2010). Incorporating experimental uncertainties into multivariate granulation modelling. Chemical Engineering Science, 65(3):1088 – 1100.

[21] Braumann, A., Kraft, M., and Mort, P. R. (2010a). Parameter estimation in a multidimensional granulation model. Powder Technology, 197(3):196 – 210.

[22] Braumann, A., Kraft, M., and Wagner, W. (2010b). Numerical study of a stochastic particle algorithm solving a multidimensional population balance model for high shear granulation. Journal of Computational Physics, 229(20):7672 – 7691.

[23] Braumann, A., Man, P. L. W., and Kraft, M. (2010c). Statistical approximation of the inverse problem in multivariate population balance modeling. Journal of Industrial and Engineering Chemistry, 49(1):428–438.

[24] Braumann, A., Man, P. L. W., and Kraft, M. (2011). The inverse problem in granulation modeling-two different statistical approaches. AIChE Journal, 57(11):3105–3121.

[25] Brownbridge, G. P. E., Smallbone, A., Phadungsukanan, W., Mosbach, S., Kraft, M., and Johansson, B. (2011). Automated IC engine model development with uncertainty propagation. In SAE Technical Paper. SAE International.

[26] Cao, L., Su, H., Mosbach, S., Kraft, M., Bhave, A., Kook, S., and Bae, C. (2008). Studying the influence of direct injection on PCCI combustion and emissions at engine idle condition using two dimensional CFD and stochastic reactor model. SAE Technical Paper No. 2008-01-0021. doi:10.4271/2008-01-0021.

[27] Celnik, M., Patterson, R. I. A., Kraft, M., and Wagner, W. (2007). Coupling a stochastic soot population balance to gas-phase chemistry using operator splitting. Combustion and Flame, 148(3):158 – 176.

[28] Celnik, M., Patterson, R. I. A., Kraft, M., and Wagner, W. (2009). A predictor-corrector algorithm for the coupling of stiff ODEs to a particle population balance. Journal of Computational Physics, 228(8):2758 – 2769.

[29] Chaturbedi, A., Bandi, C. K., Reddy, D., Pandey, P., Narang, A., Bindra, D., Tao, L., Zhao, J., Li, J., Hussain, M., et al. (2017). Compartment based population balance model development of a high shear wet granulation process via dry and wet binder addition. Chemical Engineering Research and Design, 123:187–200.

[30] Chaudhury, A., Armenante, M. E., and Ramachandran, R. (2015). Compartment based population balance modeling of a high shear wet granulation process using data analytics. Chemical Engineering Research and Design, 95:211 – 228.

[31] Chaudhury, A., Niziolek, A., and Ramachandran, R. (2013). Multidimensional mechanistic modeling of fluid bed granulation processes: An integrated approach. Advanced Powder Technology, 24(1):113 – 131.

[32] Cundall, P. A. and Strack, O. D. (1979). A discrete numerical model for granular assemblies. Geotechnique, 29(1):47–65.

[33] Deaconu, M., Fournier, N., and Tanré, E. (2002). A pure jump markov process associated with smoluchowski's coagulation equation. Ann. Probab., 30(4):1763–1796.

[34] Denesuk, M., Smith, G., Zelinski, B., Kreidl, N., and Uhlmann, D. (1993). Capillary penetration of liquid droplets into porous materials. Journal of Colloid and Interface Science, 158(1):114 – 120.

[35] DeVille, R., Riemer, N., and West, M. (2011). Weighted flow algorithms (WFA) for stochastic particle coagulation. Journal of Computational Physics, 230(23):8427 – 8451.

[36] Dhenge, R. M., Cartwright, J. J., Doughty, D. G., Hounslow, M. J., and Salman, A. D. (2011). Twin screw wet granulation: Effect of powder feed rate. Advanced Powder Technology, 22(2):162 – 166.

[37] Dhenge, R. M., Cartwright, J. J., Hounslow, M. J., and Salman, A. D. (2012a). Twin screw granulation: Steps in granule growth. International Journal of Pharmaceutics, 438(1-2):20 – 32.

[38] Dhenge, R. M., Cartwright, J. J., Hounslow, M. J., and Salman, A. D. (2012b). Twin screw wet granulation: Effects of properties of granulation liquid. Powder Technology, 229:126 – 136.

[39] Dhenge, R. M., Fyles, R. S., Cartwright, J. J., Doughty, D. G., Hounslow, M. J., and Salman, A. D. (2010). Twin screw wet granulation: Granule properties. Chemical Engineering Journal, 164(2-3):322 – 329.

[40] Dhenge, R. M., Washino, K., Cartwright, J. J., Hounslow, M. J., and Salman, A. D. (2013). Twin screw granulation using conveying screws: Effects of viscosity of granulation liquids and flow of powders. Powder Technology, 238(Supplement C):77 – 90.

[41] Djuric, D. and Kleinebudde, P. (2008). Impact of screw elements on continuous granulation with a twin-screw extruder. Journal of Pharmaceutical Sciences, 97(11):4934–4942.

[42] Dosta, M., Antonyuk, S., and Heinrich, S. (2013). Multiscale simulation of agglomerate breakage in fluidized beds. Industrial & Engineering Chemistry Research, 52(33):11275–11281.

[43] Eibeck, A. and Wagner, W. (2000). Approximative solution of the coagulation-fragmentation equation by stochastic particle systems. Stochastic Analysis and Applications, 18(6):921–948.

[44] Eibeck, A. and Wagner, W. (2001). Stochastic particle approximations for Smoluchoski's coagulation equation. The Annals of Applied Probability, 11(4):1137–1165.

[45] Eitzlmayr, A., Koscher, G., Reynolds, G., Huang, Z., Booth, J., Shering, P., and Khinast, J. (2014). Mechanistic modeling of modular co-rotating twin-screw extruders. International Journal of Pharmaceutics, 474(1-2):157 – 176.

[46] El Hagrasy, A., Hennenkamp, J., Burke, M., Cartwright, J., and Litster, J. (2013). Twin screw wet granulation: Influence of formulation parameters on granule properties and growth behavior. Powder Technology, 238:108 – 115.

[47] El Hagrasy, A. S. and Litster, J. D. (2013). Granulation rate processes in the kneading elements of a twin screw granulator. AIChE Journal, 59(11):4100–4115.

[48] Ennis, B. (1990). On the mechanics of granulation. PhD dissertation, The City College of the City University of New York.

[49] Ennis, B. (1997). Unto dust shalt thou return. Powders and Grains, 97:13–23.

[50] Ennis, B. J., Tardos, G., and Pfeffer, R. (1991). A special volume devoted to the second symposium on advances in particulate technology a microlevel-based characterization of granulation phenomena. Powder Technology, 65(1):257 – 272.

[51] FDA (2002). Guidance: Pharmaceutical cGMPs for the 21st century - a risk-based approach. Technical Report.

[52] FDA (2004). Guidance for industry: PAT, a framework for innovative pharmaceutical development, manufacturing, and quality assurance. Technical Report.

[53] FDA (2011). Guidance for industry: Process validation – general principles and practices. Technical Report.

[54] Gantt, J. A., Cameron, I. T., Litster, J. D., and Gatzke, E. P. (2006). Determination of coalescence kernels for high-shear granulation using DEM simulations. Powder Technology, 170(2):53 – 63.

[55] Gantt, J. A. and Gatzke, E. P. (2006). A stochastic technique for multidimensional granulation modeling. AIChE Journal, 52(9):3067–3077.

[56] Ge, W., Han, Y., Wang, J., Wang, L., Liu, X., Zhou, J., Li, J., Freeman, T., Birkmire, A., and Armstrong, B. (2015). A QbD approach to continuous tablet manufacture. Procedia Engineering, 102:443 – 449.

[57] GEA (2016). Successful Tableting Supplement. http://www.gea.com/en/binaries/Successful%20Tableting%20Supplement_tcm11-31710.pdf (accessed 19-12-2017).

[58] Ghebre-Sellassie, I., Mollan, M., Pathak, N., Lodaya, M., and Fessehaie, M. (2002). Continuous production of pharmaceutical granulation. US Patent 6,499,984.

[59] Gillespie, D. T. (1975). An exact method for numerically simulating the stochastic coalescence process in a cloud. Journal of the Atmospheric Sciences, 32(10):1977–1989.

[60] Glaser, T., Sanders, C., Wang, F., Cameron, I., Litster, J., Poon, J., Ramachandran, R., Immanuel, C., and Doyle, F. (2009). Model predictive control of continuous drum granulation. Journal of Process Control, 19(4):615–622.

[61] Goodson, M. and Kraft, M. (2004). Simulation of coalescence and breakage: an assessment of two stochastic methods suitable for simulating liquid-liquid extraction. Chemical Engineering Science, 59(18):3865 – 3881.

[62] Goodson, M., Kraft, M., Forrest, S., and Bridgwater, J. (2004). A multidimensional population balance model for agglomeration. In PARTEC 2004:International Congress for Particle Technology.

[63] Gorringe, L., Kee, G., Saleh, M., Fa, N., and Elkes, R. (2017). Use of the channel fill level in defining a design space for twin screw wet granulation. International Journal of Pharmaceutics, 519(1):165 – 177.

[64] Hao, X., Zhao, H., Xu, Z., and Zheng, C. (2013). Population balance-Monte Carlo simulation for gas-to-particle synthesis of nanoparticles. Aerosol science and technology, 47(10):1125–1133.

[65] Hapgood, K. P., Litster, J. D., and Smith, R. (2003). Nucleation regime map for liquid bound granules. AIChE Journal, 49(2):350–361.

[66] Hodgman, C. D. (1951). Handbook of chemistry and physics., volume 71. LWW.

[67] Hooke, R. and Jeeves, T. A. (1961). "Direct search" solution of numerical and statistical problems. Journal of the ACM, 8(2):212–229.

[68] Hulburt, H. and Katz, S. (1964). Some problems in particle technology: A statistical mechanical formulation. Chemical Engineering Science, 19(8):555 – 574.

[69] ICH (2005). Guideline Q9: Quality risk management. Technical Report.

[70] ICH (2008). Guideline Q10: Pharmaceutical quality system. Technical Report.

[71] ICH (2009). Guideline Q8R2: Pharmaceutical development. Technical Report.

[72] Irizarry, R. (2012). Fast compartmental Monte Carlo simulation of population balance models: Application to nanoparticle formation in nonhomogeneous conditions. Ind. Eng. Chem. Res., 51(47):15484–15496.

[73] Iveson, S. M. (2001). Granule coalescence modelling: including the effects of bond strengthening and distributed impact separation forces. Chemical Engineering Science, 56(6):2215 – 2220.

[74] Iveson, S. M. (2002). Limitations of one-dimensional population balance models of wet granulation processes. Powder Technology, 124(3):219 – 229.

[75] Iveson, S. M., Litster, J. D., Hapgood, K., and Ennis, B. J. (2001). Nucleation, growth and breakage phenomena in agitated wet granulation processes: a review. Powder Technology, 117(1-2):3 – 39.

[76] Jr., C. L. M., Rajniak, P., and Matsoukas, T. (2013). Multi-component population balance modeling of granulation with continuous addition of binder. Powder Technology, 236(0):211 – 220.

[77] Kastner, C. A., Brownbridge, G. P., Mosbach, S., and Kraft, M. (2013). Impact of powder characteristics on a particle granulation model. Chemical Engineering Science, 97:282 – 295.

[78] Keleb, E., Vermeire, A., C, and Remon, J. (2004). Twin screw granulation as a simple and efficient tool for continuous wet granulation. International Journal of Pharmaceutics, 273(1-2):183 – 194.

[79] Kleinebudde, P. (2004). Roll compaction/dry granulation: pharmaceutical applications. European Journal of Pharmaceutics and Biopharmaceutics, 58(2):317 – 326.

[80] Kockmann, N., Gottsponer, M., Zimmermann, B., and Roberge, D. (2008). Enabling continuous-flow chemistry in microstructured devices for pharmaceutical and fine-chemical production. Chemistry – A European Journal, 14(25):7470–7477.

[81] Kolodko, A. and Sabelfeld, K. (2003). Stochastic particle methods for smoluchowski coagulation equation: variance reduction and error estimations. Monte Carlo Methods and Applications, 9(4):315–339.

[82] Kotalczyk, G. and Kruis, F. (2017). A Monte Carlo method for the simulation of coagulation and nucleation based on weighted particles and the concepts of stochastic resolution and merging. Journal of Computational Physics, 340:276 – 296.

[83] Kozhar, S., Dosta, M., Antonyuk, S., Heinrich, S., and Bröckel, U. (2015). DEM simulations of amorphous irregular shaped micrometer-sized titania agglomerates at compression. Advanced Powder Technology, 26(3):767 – 777. Special issue of the 7th World Congress on Particle Technology.

[84] Kraft, M. (2005). Modelling of particulate processes. KONA Powder and Particle Journal, 23:18–35.

[85] Kumar, A., Gernaey, K. V., Beer, T. D., and Nopens, I. (2013). Model-based analysis of high shear wet granulation from batch to continuous processes in pharmaceutical production - A critical review. Eur. J. Pharm. Biopharm., 85(3, Part B):814 – 832.

[86] Kumar, A., Vercruysse, J., Bellandi, G., Gernaey, K. V., Vervaet, C., Remon, J. P., Beer, T. D., and Nopens, I. (2014a). Experimental investigation of granule size and shape dynamics in twin-screw granulation. International Journal of Pharmaceutics, 475(1-2):485 – 495.

[87] Kumar, A., Vercruysse, J., Mortier, S. T., Vervaet, C., Remon, J. P., Gernaey, K. V., Beer, T. D., and Nopens, I. (2016). Model-based analysis of a twin-screw wet granulation system for continuous solid dosage manufacturing. Computers & Chemical Engineering, 89:62 – 70.

[88] Kumar, A., Vercruysse, J., Toiviainen, M., Panouillot, P.-E., Juuti, M., Vanhoorne, V., Vervaet, C., Remon, J. P., Gernaey, K. V., Beer, T. D., and Nopens, I. (2014b). Mixing and transport during pharmaceutical twin-screw wet granulation: Experimental analysis via chemical imaging. European Journal of Pharmaceutics and Biopharmaceutics, 87(2):279 – 289.

[89] Kumar, A., Vercruysse, J., Vanhoorne, V., Toiviainen, M., Panouillot, P.-E., Juuti, M., Vervaet, C., Remon, J. P., Gernaey, K. V., Beer, T. D., and Nopens, I. (2015). Conceptual framework for model-based analysis of residence time distribution in twin-screw granulation. European Journal of Pharmaceutical Sciences, 71:25 – 34.

[90] Kumar, S. and Ramkrishna, D. (1996a). On the solution of population balance equations by discretization-I. a fixed pivot technique. Chemical Engineering Science, 51(8):1311 – 1332.

[91] Kumar, S. and Ramkrishna, D. (1996b). On the solution of population balance equations by discretization-II. a moving pivot technique. Chemical Engineering Science, 51(8):1333 – 1342.

[92] Kumar, S. and Ramkrishna, D. (1997). On the solution of population balance equations by discretization-III. nucleation, growth and aggregation of particles. Chemical Engineering Science, 52(24):4659 – 4679.

[93] Lawrence, X. Y. (2008). Pharmaceutical quality by design: product and process development, understanding, and control. Pharmaceutical research, 25(4):781–791.

[94] Lee, K. F., Dosta, M., McGuire, A. D., Mosbach, S., Wagner, W., Heinrich, S., and Kraft, M. (2017). Development of a multi-compartment population balance model for high-shear wet granulation with discrete element method. Computers & Chemical Engineering, 99:171 – 184.

[95] Lee, K. F., Mosbach, S., Kraft, M., and Wagner, W. (2015a). A multi-compartment population balance model for high shear granulation. Computers & Chemical Engineering, 75:1 – 13.

[96] Lee, K. F., Patterson, R. I. A., Wagner, W., and Kraft, M. (2015b). Stochastic weighted particle methods for population balance equations with coagulation, fragmentation and spatial inhomogeneity. Journal of Computational Physics, 303:1 – 18.

[97] Lee, K. T., Ingram, A., and Rowson, N. A. (2012). Twin screw wet granulation: The study of a continuous twin screw granulator using positron emission particle tracking (PEPT) technique. European Journal of Pharmaceutics and Biopharmaceutics, 81(3):666 – 673.

[98] Leuenberger, H. (2001). New trends in the production of pharmaceutical granules: batch versus continuous processing. European Journal of Pharmaceutics and Biopharmaceutics, 52(3):289 – 296.

[99] Li, H., Thompson, M., and O'Donnell, K. (2014). Understanding wet granulation in the kneading block of twin screw extruders. Chemical Engineering Science, 113(0):11 – 21.

[100] Li, J., Freireich, B., Wassgren, C., and Litster, J. D. (2012). A general compartment-based population balance model for particle coating and layered granulation. AIChE Journal, 58(5):1397–1408.

[101] Li, Z., Kessel, J., Grünewald, G., and Kind, M. (2013). Coupled CFD-PBE simulation of nucleation in fluidized bed spray granulation. Drying Technology, 31(15):1888–1896.

[102] Lindberg, N. O., Tufvesson, C., Holm, P., and Olbjer, L. (1988). Extrusion of an effervescent granulation with a twin screw extruder, Baker Perkins MPF 50 D. influence on intragranular porosity and liquid saturation. Drug Development and Industrial Pharmacy, 14(13):1791–1798.

[103] Lindberg, N.-O., Tufvesson, C., and Olbjer, L. (1987). Extrusion of an effervescent granulation with a twin screw extruder, baker perkins mpf 50 d. Drug Development and Industrial Pharmacy, 13(9-11):1891–1913.

[104] Litster, J., Hapgood, K., Michaels, J., Sims, A., Roberts, M., Kameneni, S., and Hsu, T. (2001). Liquid distribution in wet granulation: dimensionless spray flux. Powder Technology, 114(1):32 – 39.

[105] Lourenço, V., Lochmann, D., Reich, G., Menezes, J. C., Herdling, T., and Schewitz, J. (2012). A quality by design study applied to an industrial pharmaceutical fluid bed granulation. European Journal of Pharmaceutics and Biopharmaceutics, 81(2):438 – 447.

[106] Lute, S. V., Dhenge, R. M., Hounslow, M. J., and Salman, A. D. (2016). Twin screw granulation: Understanding the mechanism of granule formation along the barrel length. Chemical Engineering Research and Design, 110:43 – 53.

[107] Maisels, A., Kruis, F. E., and Fissan, H. (2004). Direct simulation Monte Carlo for simultaneous nucleation, coagulation, and surface growth in dispersed systems. Chemical Engineering Science, 59(11):2231 – 2239.

[108] Man, P. L., Braumann, A., and Kraft, M. (2010). Resolving conflicting parameter estimates in multivariate population balance models. Chemical Engineering Science, 65(13):4038 – 4045.

[109] Maniruzzaman, M., Nair, A., Renault, M., Nandi, U., Scoutaris, N., Farnish, R., Bradley, M. S., Snowden, M. J., and Douroumis, D. (2015). Continuous twin-screw granulation for enhancing the dissolution of poorly water soluble drug. International Journal of Pharmaceutics, 496(1):52 – 62.

[110] Marchisio, D. L. and Fox, R. O. (2005). Solution of population balance equations using the direct quadrature method of moments. Journal of Aerosol Science, 36(1):43 – 73.

[111] McGuire, A. D., Lee, K. F., Dosta, M., Mosbach, S., Rosenboom, J.-G., Heinrich, S., and Kraft, M. (2017). Compartmental residence time estimation in batch granulators using a colourimetric image analysis algorithm and discrete element modelling. Advanced Powder Technology, 28(9):2239 – 2255.

[Meggle] Meggle. Meggle excipients and technology. https://www.meggle-pharma.com/en/productConfigurator.html. Accessed: 2018-01-30.

[113] Meier, R., Moll, K.-P., Krumme, M., and Kleinebudde, P. (2017). Impact of fill-level in twin-screw granulation on critical quality attributes of granules and tablets. European Journal of Pharmaceutics and Biopharmaceutics, 115(Supplement C):102 – 112.

[114] Meier, R., Thommes, M., Rasenack, N., Krumme, M., Moll, K.-P., and Kleinebudde, P. (2015). Simplified formulations with high drug loads for continuous twin-screw granulation. International Journal of Pharmaceutics, 496(1):12 – 23.

[115] Meng, W., Kotamarthy, L., Panikar, S., Sen, M., Pradhan, S., Marc, M., Litster, J. D., Muzzio, F. J., and Ramachandran, R. (2016). Statistical analysis and comparison of a continuous high shear granulator with a twin screw granulator: Effect of process parameters on critical granule attributes and granulation mechanisms. International Journal of Pharmaceutics, 513(1-2):357 – 375.

[116] Menz, W. J., Akroyd, J., and Kraft, M. (2014a). Stochastic solution of population balance equations for reactor networks. Journal of Computational Physics, 256:615–629.

[117] Menz, W. J., Brownbridge, G. P., and Kraft, M. (2014b). Global sensitivity analysis of a model for silicon nanoparticle synthesis. Journal of Aerosol Science, 76:188 – 199.

[118] Menz, W. J., Patterson, R. I. A., Wagner, W., and Kraft, M. (2013). Application of stochastic weighted algorithms to a multidimensional silica particle model. Journal of Computational Physics, 248(0):221–234.

[119] Meyer, K., Bück, A., and Tsotsas, E. (2015). Dynamic multi-zone population balance model of particle formulation in fluidized beds. Procedia Engineering, 102(Supplement C):1456 – 1465.

[120] MoDS (2015). (Model Development Suite). CMCL Innovations, Cambridge, United Kingdom. https://cmclinnovations.com/products/mods/.

[121] Mosbach, S., Braumann, A., Man, P. L., Kastner, C. A., Brownbridge, G. P., and Kraft, M. (2012). Iterative improvement of Bayesian parameter estimates for an engine model by means of experimental design. Combustion and Flame, 159(3):1303 – 1313.

[122] Mosbach, S., Hong, J. H., Brownbridge, G. P. E., Kraft, M., Gudiyella, S., and Brezinsky, K. (2014). Bayesian error propagation for a kinetic model of n-propylbenzene oxidation in a shock tube. International Journal of Chemical Kinetics, 46(7):389–404.

[123] Mosbach, S., Su, H., Kraft, M., Bhave, A., Mauss, F., Wang, Z., and Wang, J.-X. (2007). Dual injection homogeneous charge compression ignition engine simulation using a stochastic reactor model. International Journal of Engine Research, 8(1):41–50.

[124] Mu, B. and Thompson, M. (2012). Examining the mechanics of granulation with a hot melt binder in a twin-screw extruder. Chemical Engineering Science, 81:46 – 56.

[125] Müller, L., Klar, A., and Schneider, F. (2017). A numerical comparison of the method of moments for the population balance equation. arXiv preprint arXiv:1706.05854.

[126] Oullion, M., Reynolds, G., and Hounslow, M. (2009). Simulating the early stage of high-shear granulation using a two-dimensional Monte-Carlo approach. Chemical Engineering Science, 64(4):673 – 685.

[127] Paavolaa, M. K., El Hagrasy, A. S., Litster, J. D., and Leiviskäa, K. J. (2013). 3D population balance model for continuous twin screw granulator. Chemical Engineering Transactions, 32.

[128] Pan, M., Sikorski, J., Akroyd, J., Mosbach, S., Lau, R., and Kraft, M. (2016). Design technologies for eco-industrial parks: From unit operations to processes, plants and industrial networks. Applied Energy, 175:305 – 323.

[129] Pandya, J. and Spielman, L. (1983). Floc breakage in agitated suspensions: Effect of agitation rate. Chemical Engineering Science, 38(12):1983 – 1992.

[130] Parikh, D. M. (2016). Handbook of pharmaceutical granulation technology. CRC Press.

[131] Patterson, R. I. A. (2007). Numerical Modelling of Soot Formation. PhD dissertation, The University of Cambridge.

[132] Patterson, R. I. A. (2013). Convergence of stochastic particle systems undergoing advection and coagulation. Stochastic Analysis and Applications, 31(5):800–829.

[133] Patterson, R. I. A., Singh, J., Balthasar, M., Kraft, M., and Norris, J. (2006). The linear process deferment algorithm: A new technique for solving population balance equations. SIAM Journal on Scientific Computing, 28(1):303–320.

[134] Patterson, R. I. A. and Wagner, W. (2012). A stochastic weighted particle method for coagulation–advection problems. SIAM Journal on Scientific Computing, 34(3):B290–B311.

[135] Patterson, R. I. A., Wagner, W., and Kraft, M. (2011). Stochastic weighted particle methods for population balance equations. Journal of Computational Physics, 230(19):7456 – 7472.

[136] Pearson, K. (1894). Contributions to the mathematical theory of evolution. Philosophical Transactions of the Royal Society of London. A, 185:71–110.

[137] Poon, J. M.-H., Ramachandran, R., Sanders, C. F., Glaser, T., Immanuel, C. D., III, F. J. D., Litster, J. D., Stepanek, F., Wang, F.-Y., and Cameron, I. T. (2009). Experimental validation studies on a multi-dimensional and multi-scale population balance model of batch granulation. Chemical Engineering Science, 64(4):775 – 786.

[138] Pradhan, S. U., Sen, M., Li, J., Litster, J. D., and Wassgren, C. R. (2017). Granule breakage in twin screw granulation: Effect of material properties and screw element geometry. Powder Technology, 315(Supplement C):290 – 299.

[139] Ramachandran, R. and Chaudhury, A. (2012). Model-based design and control of a continuous drum granulation process. Chemical Engineering Research and Design, 90(8):1063 – 1073.

[140] Ramkrishna, D. (2000). Population Balances: Theory and Applications to Particulate Systems in Engineering. Elsevier Science.

[141] Reynolds, G. K., Sanders, C. F. W., Salman, A. D., and Hounslow, M. J. (2004). The kinetics of high-shear granulation. In Antony, S. J., Hoyle, W., Ding, Y., and Ding, Y., editors, Granular Materials: Fundamentals and Applications, pages 296–318. The Royal Society of Chemistry.

[142] Rjasanow, S. and Wagner, W. (1996). A stochastic weighted particle method for the Boltzmann equation. Journal of Computational Physics, 124(2):243 – 253.

[143] Roberge, D. M., Zimmermann, B., Rainone, F., Gottsponer, M., Eyholzer, M., and Kockmann, N. (2008). Microreactor technology and continuous processes in the fine chemical and pharmaceutical industry: Is the revolution underway? Organic Process Research & Development, 12(5):905–910.

[144] Rosenboom, J.-G., Antonyuk, S., Heinrich, S., and Kraft, M. (2015). Characterisation of lactose powder and granules for multivariate wet granulation modelling. Chemical Engineering Science, 123:395 – 405.

[145] Saleh, M. F., Dhenge, R. M., Cartwright, J. J., Hounslow, M. J., and Salman, A. D. (2015). Twin screw wet granulation: Effect of process and formulation variables on powder caking during production. International Journal of Pharmaceutics, 496(2):571 – 582.

[146] Sayin, R. (2016). Mechanistic Studies of Twin Screw Granulation. PhD dissertation, Purdue University.

[147] Sayin, R., El Hagrasy, A., and Litster, J. (2015). Distributive mixing elements: Towards improved granule attributes from a twin screw granulation process. Chemical Engineering Science, 125:165 – 175.

[148] Schaafsma, S. H., Vonk, P., Segers, P., and Kossen, N. W. (1998). Description of agglomerate growth. Powder technology, 97(3):183–190.

[149] Schaber, S. D., Gerogiorgis, D. I., Ramachandran, R., Evans, J. M. B., Barton, P. I., and Trout, B. L. (2011). Economic analysis of integrated continuous and batch pharmaceutical manufacturing: A case study. Industrial & Engineering Chemistry Research, 50(17):10083–10092.

[150] Schæfer, T. and Mathiesen, C. (1996). Melt pelletization in a high shear mixer. IX. effects of binder particle size. International Journal of Pharmaceutics, 139(1):139 – 148.

[151] Seem, T. C., Rowson, N. A., Gabbott, I., de Matas, M., Reynolds, G. K., and Ingram, A. (2016). Asymmetric distribution in twin screw granulation. European Journal of Pharmaceutics and Biopharmaceutics, 106:50 – 58.

[152] Seem, T. C., Rowson, N. A., Ingram, A., Huang, Z., Yu, S., de Matas, M., Gabbott, I., and Reynolds, G. K. (2015). Twin screw granulation - a literature review. Powder Technology, 276:89 – 102.

[153] Sen, M. and Ramachandran, R. (2013). A multi-dimensional population balance model approach to continuous powder mixing processes. Advanced Powder Technology, 24(1):51–59.

[154] Sherrington, P. and Oliver, R. (1981). Granulation, Heyden.

[155] Shi, D. and McCarthy, J. (2008). Numerical simulation of liquid transfer between particles. Powder Technology, 184(1):64 – 75.

[156] Shirazian, S., Kuhs, M., Darwish, S., Croker, D., and Walker, G. M. (2017). Artificial neural network modelling of continuous wet granulation using a twin-screw extruder. International Journal of Pharmaceutics.

[157] Singh, R., Barrasso, D., Chaudhury, A., Sen, M., Ierapetritou, M., and Ramachandran, R. (2014). Closed-loop feedback control of a continuous pharmaceutical tablet manufacturing process via wet granulation. Journal of Pharmaceutical Innovation, 9(1):16–37.

[158] Smoluchowski, M. (1916). Drei vortrage uber diffusion. Brownsche bewegung und koagulation von kolloidteilchen. Z. Phys., 17:557–585.

[159] Snow, R. H., Allen, T., Ennis, B. J., and Litster, J. D. (1984). Perry's Chemical Engineers' Handbook Chapter 20: Size Reduction and Enlargement, volume 20.

[160] Spettl, A., Dosta, M., Klingner, F., Heinrich, S., and Schmidt, V. (2017). Copula-based approximation of particle breakage as link between DEM and PBM. Computers & Chemical Engineering, 99(Supplement C):158 – 170.

[161] Spielman, L. and Levenspiel, O. (1965). A monte carlo treatment for reacting and coalescing dispersed phase systems. Chemical Engineering Science, 20(3):247 – 254.

[162] Tan, H., Goldschmidt, M., Boerefijn, R., Hounslow, M., Salman, A., and Kuipers, J. (2004). Building population balance model for fluidized bed melt granulation: lessons from kinetic theory of granular flow. Powder Technology, 142(2-3):103 – 109.

[163] Tardos, G. I. and Gupta, R. (1996). Forces generated in solidifying liquid bridges between two small particles. Powder Technology, 87(2):175 – 180.

[164] Tardos, G. I., Khan, M. I., and Mort, P. R. (1997). Critical parameters and limiting conditions in binder granulation of fine powders. Powder Technology, 94(3):245 – 258.

[165] Thompson, M. and Sun, J. (2010). Wet granulation in a twin-screw extruder: Implications of screw design. Journal of Pharmaceutical Sciences, 99(4):2090–2103.

[166] van Peborgh Gooch, J. R. and Hounslow, M. J. (1996). Monte carlo simulation of size-enlargement mechanisms in crystallization. AIChE Journal, 42(7):1864–1874.

[167] Vercruysse, J., Burggraeve, A., Fonteyne, M., Cappuyns, P., Delaet, U., Assche, I. V., Beer, T. D., Remon, J., and Vervaet, C. (2015a). Impact of screw configuration on the particle size distribution of granules produced by twin screw granulation. International Journal of Pharmaceutics, 479(1):171 – 180.

[168] Vercruysse, J., Díaz, D. C., Peeters, E., Fonteyne, M., Delaet, U., Assche, I. V., Beer, T. D., Remon, J., and Vervaet, C. (2012). Continuous twin screw granulation: Influence of process variables on granule and tablet quality. European Journal of Pharmaceutics and Biopharmaceutics, 82(1):205 – 211.

[169] Vercruysse, J., Peeters, E., Fonteyne, M., Cappuyns, P., Delaet, U., Assche, I. V., Beer, T. D., Remon, J., and Vervaet, C. (2015b). Use of a continuous twin screw granulation and drying system during formulation development and process optimization. European Journal of Pharmaceutics and Biopharmaceutics, 89:239 – 247.

[170] Vervaet, C. and Remon, J. P. (2005). Continuous granulation in the pharmaceutical industry. Chemical Engineering Science, 60(14):3949 – 3957.

[171] Vikhansky, A. and Kraft, M. (2005). Single-particle method for stochastic simulation of coagulation processes. Chemical Engineering Science, 60(4):963 – 967.

[172] Vonk, P., Guillaume, C., Ramaker, J., Vromans, H., and Kossen, N. (1997). Growth mechanisms of high-shear pelletisation. International Journal of Pharmaceutics, 157(1):93 – 102.

[173] Wang, F. and Cameron, I. (2007). A multi-form modelling approach to the dynamics and control of drum granulation processes. Powder Technology, 179(1):2 – 11.

[174] Wildeboer, W., Litster, J., and Cameron, I. (2005). Modelling nucleation in wet granulation. Chemical Engineering Science, 60(14):3751 – 3761.

[175] Willecke, N., Szepes, A., Wunderlich, M., Remon, J., Vervaet, C., and Beer, T. D. (2017). Identifying overarching excipient properties towards an in-depth understanding of process and product performance for continuous twin-screw wet granulation. International Journal of Pharmaceutics, 522(1):234–247.

[176] Zadow, J. G. (1984). Lactose: Properties and uses. Journal of Dairy Science, 67(11):2654–2679.

[177] Zhao, H., Kruis, F. E., and Zheng, C. (2009). Reducing statistical noise and extending the size spectrum by applying weighted simulation particles in Monte Carlo simulation of coagulation. Aerosol Science and Technology, 43(8):781–793.

[178] Zhao, H., Kruis, F. E., and Zheng, C. (2010). A differentially weighted Monte Carlo method for two-component coagulation. Journal of Computational Physics, 229(19):6931 – 6945.

[179] Zhao, H. and Zheng, C. (2006). Stochastic algorithm and numerical simulation for drop scavenging of aerosols. Applied Mathematics and Mechanics, 27(10):1321–1332.

[180] Zhao, H. and Zheng, C. (2009). A new event-driven constant-volume method for solution of the time evolution of particle size distribution. Journal of Computational Physics, 228(5):1412 – 1428.

[181] Zhao, H. and Zheng, C. (2013). A population balance-Monte Carlo method for particle coagulation in spatially inhomogeneous systems. Computers & Fluids, 71:196 – 207.

[182] Zhao, H., Zheng, C., and Xu, M. (2005). Multi-Monte Carlo approach for general dynamic equation considering simultaneous particle coagulation and breakage. Powder Technology, 154(2-3):164 – 178.

Appendix A

Derivations

A.1 Appendix: derivation of transport scaling factor

It is desired show that the weight scaling factor applied to inflow particles within the transport jump process (7.58) has the form:

$$F_{\mathrm{c}}(z,t) = \left[\frac{V_{\mathrm{samp}}(z,t)}{V_{\mathrm{samp}}(z-1,t)}\right]\left[\frac{N_{\mathrm{agg}}(z-1,t)}{N_{\mathrm{agg}}(z,t)}\right]. \tag{A.1}$$

in the context of a non-droplet zone compartment ($z \neq 1$) for a twin-screw model system.

This starts with the assertion that each compartment in the network is one of constant mass and volume (i.e $M_{\mathrm{real}}(z), V_{\mathrm{real}}(z) \neq f(t)$ and thus, to provide continuity, the mass flow rate through each compartment $\dot{m}_{\mathrm{feed}}$ is the same). It follows that the concentration of mass flow entering/leaving the sample volume (denoted by the superscript $^{\mathrm{SV}}$) for compartment z must be the same as that entering the physical system i.e.

$$\frac{\dot{m}^{\mathrm{SV}}_{\mathrm{inflow}}(z,t)}{V_{\mathrm{samp}}(z)} = \frac{\dot{m}^{\mathrm{SV}}_{\mathrm{outflow}}(z,t)}{V_{\mathrm{samp}}(z,t)} = \frac{\dot{m}_{\mathrm{feed}}}{V_{\mathrm{real}}(z)} \tag{A.2}$$

Thus, one can express the mass flow of aggregate particles entering the systems based on the mass fraction of aggregates (in a mixture of aggregates and primary

particles) in the preceding compartment (at steady state) as

$$\underset{z\in\mathbb{L},\, z>1}{\dot{m}^{\mathrm{SV}}_{\mathrm{agg,inflow}}(z,t)} = \dot{m}^{\mathrm{SV}}_{\mathrm{inflow}}(z,t)\frac{M^{\mathrm{SV}}_{\mathrm{agg}}(z-1,t)}{M^{\mathrm{SV}}_{\mathrm{total}}(z-1,t)} \tag{A.3}$$

$$= \frac{\dot{m}_{\mathrm{feed}} M^{\mathrm{SV}}_{\mathrm{agg}}(z-1,t) V_{\mathrm{samp}}(z,t)}{V_{\mathrm{real}}(z) M^{\mathrm{SV}}_{\mathrm{total}}(z-1,t)}, \tag{A.4}$$

where $M^{\mathrm{SV}}_{\mathrm{agg}}(z,t)$ and $M^{\mathrm{SV}}_{\mathrm{total}}(z,t)$ are the mass of aggregates and the total mass (primary particles and aggregates) in the sample volume, respectively.

Let the average mass of computational particles (aggregate) in the sample volume associated with compartment z be defined as

$$\langle mw \rangle_{z,t} = \frac{M^{\mathrm{SV}}_{\mathrm{agg}}(z,t)}{N_{\mathrm{agg}}(z,t)}. \tag{A.5}$$

It is required that the inflow process to compartment z sample the particle distribution from compartment $z-1$. Thus, one is free to scale the weights of particles sampled from the preceding reactor by some constant scaling factor F_{c}, prior to their inception into the current reactor. This scaling has no effect on the physical particle distribution in compartment $z-1$. Incorporating this scaling factor, the average mass of a particle incepted into compartment z from compartment $z-1$ during an inflow event is

$$F_{\mathrm{c}} \langle mw \rangle_{z-1,t}. \tag{A.6}$$

One may write the mass inflow rate into compartment z in an alternative form, which is based on the rate of inflow events $R^{\mathrm{SWA}}_{\mathrm{inflow}}(z,t)$, as

$$\underset{z\in\mathbb{L},\, z>1}{\dot{m}^{\mathrm{SV}}_{\mathrm{agg,inflow}}(z,t)} = R^{\mathrm{SWA}}_{\mathrm{inflow}}(z,t) F_{\mathrm{c}} \langle mw \rangle_{z-1,t}. \tag{A.7}$$

Equating (A.4), (A.7) and substituting (A.5), permits one to write

$$\underset{z\in\mathbb{L},\, z>1}{R^{\mathrm{SWA}}_{\mathrm{inflow}}(z,t)} = \frac{\dot{m}_{\mathrm{feed}} V_{\mathrm{samp}}(z,t) N_{\mathrm{agg}}(z-1,t)}{V_{\mathrm{real}}(z) M^{\mathrm{SV}}_{\mathrm{total}}(z-1,t) F_{\mathrm{c}}}. \tag{A.8}$$

Using the residence time definition

$$\dot{m}_{\text{feed}} := \frac{M_{\text{real}}(z-1)}{\tau(z-1)} \tag{A.9}$$

$$= \frac{M^{\text{SV}}_{\text{total}}(z-1,t)V_{\text{real}}(z-1)}{\tau(z-1)V_{\text{samp}}(z-1,t)}, \tag{A.10}$$

one may write (A.8) as

$$R^{\text{SWA}}_{\substack{\text{inflow}\\ z\in\mathbb{L},\, z>1}}(z,t) = \left[\frac{V_{\text{real}}(z-1)}{V_{\text{real}}(z)}\right]\left[\frac{V_{\text{samp}}(z,t)}{V_{\text{samp}}(z-1,t)}\right]\left[\frac{N_{\text{agg}}(z-1,t)}{F_{\text{c}}\tau(z-1)}\right]. \tag{A.11}$$

Equation (A.11) can be further simplified by acknowledging that a series of compartments with constant mass and constant volume has the property

$$\frac{V_{\text{real}}(z-1)}{V_{\text{real}}(z)} = \frac{M_{\text{real}}(z-1)}{M_{\text{real}}(z)}, \tag{A.12}$$

and, again, applying the residence time definition to each compartment in (A.12), one sees that

$$\frac{V_{\text{real}}(z-1)}{V_{\text{real}}(z)} = \frac{\tau(z-1)}{\tau(z)}. \tag{A.13}$$

Substitution of (A.13) into (A.11) yields

$$R^{\text{SWA}}_{\substack{\text{inflow}\\ z\in\mathbb{L},\, z>1}}(z,t) = \left[\frac{V_{\text{samp}}(z,t)}{V_{\text{samp}}(z-1,t)}\right]\left[\frac{N_{\text{agg}}(z-1,t)}{F_{\text{c}}\tau(z)}\right]. \tag{A.14}$$

Now, if the inflow jump is to be coupled with the outflow jump process for any non-droplet zone ($z \neq 1$) then it is required that

$$R^{\text{SWA}}_{\substack{\text{inflow}\\ z\in\mathbb{L},\, z>1}}(z,t) = R^{\text{SWA}}_{\substack{\text{outflow}\\ z\in\mathbb{L},\, z>1}}(z,t) = \frac{N_{\text{agg}}(z)}{\tau(z)}. \tag{A.15}$$

Finally, equating (A.14) and (A.15) one arrives at an expression for the inflow weight scaling factor

$$F_{\text{c}}(z,t) = \left[\frac{V_{\text{samp}}(z,t)}{V_{\text{samp}}(z-1,t)}\right]\left[\frac{N_{\text{agg}}(z-1,t)}{N_{\text{agg}}(z,t)}\right]. \tag{A.16}$$

A.2 Appendix: layering rate equation

The layering source term in the primary particle PBE (7.2) has the form

$$\left.\frac{\mathrm{d}c_{\mathrm{pp}}}{\mathrm{d}t}\right|_{\mathrm{layer}} = -\int_{\mathbb{X}_{\mathrm{agg}}} r_{\mathrm{layer}}(z,t,x,c_{\mathrm{pp}})\lambda(z,t,\mathrm{d}x) \tag{A.17}$$

$$\approx -\frac{1}{V_{\mathrm{samp}}(z,t)} \sum_{i=1}^{N_{\mathrm{agg}(z,t)}} r_{\mathrm{layer}}(z,t,x_i,c_{\mathrm{pp}})w_i. \tag{A.18}$$

Hence, in number form

$$\left.\frac{\mathrm{d}N_{\mathrm{pp}}}{\mathrm{d}t}\right|_{\mathrm{layer}} \approx -\sum_{i=1}^{N_{\mathrm{agg}(z,t)}} r_{\mathrm{layer}}(z,t,x_i,c_{\mathrm{pp}})w_i, \tag{A.19}$$

and the change in the number of primaries over the global deferment step is then characterised as

$$N_{\mathrm{pp}}(z,t_{\mathrm{target}}) \leftarrow N_{\mathrm{pp}}(z,t) - \sum_{i=1}^{N_{\mathrm{agg}(z,t)}} \int_{t_{\mathrm{p}}}^{t_{\mathrm{target}}} r_{\mathrm{layer}}(z,t,x_i,c_{\mathrm{pp}})w_i \,\mathrm{d}t. \tag{A.20}$$

Re-arranging (7.15) yields

$$r_{\mathrm{layer}}(z,t,x,c_{\mathrm{pp}}) = \frac{1}{v_{\mathrm{pp}}} \left.\frac{\mathrm{d}s_{\mathrm{o}}(x)}{\mathrm{d}t}\right|_{\mathrm{layer}} \tag{A.21}$$

and since

$$\left.\frac{\mathrm{d}s_{\mathrm{o}}(x)}{\mathrm{d}t}\right|_{\mathrm{consol}} = 0, \tag{A.22}$$

then, by way of (7.24),

$$r_{\mathrm{layer}}(z,t,x,c_{\mathrm{pp}}) = \frac{1}{v_{\mathrm{pp}}} \left.\frac{\mathrm{d}s_{\mathrm{o}}(x)}{\mathrm{d}t}\right|_{\mathrm{defer}}. \tag{A.23}$$

Substitution of (A.23) into (A.20) and assuming that changes in N_{pp} over the deferment step are small yields

$$N_{\mathrm{pp}}(z,t_{\mathrm{target}}) \leftarrow N_{\mathrm{pp}}(z,t_{\mathrm{target}}) - \frac{1}{v_{\mathrm{pp}}} \sum_{i=1}^{N_{\mathrm{agg}(z,t)}} \left[s_{\mathrm{o}}(x_i)_{t_{\mathrm{target}}} - s_{\mathrm{o}}(x_i)_{t_{\mathrm{p}}}\right] w_i, \tag{A.24}$$

which completes the derivation.

The argument above can be applied in the context of local deferment steps by summing only over the sequence of particles which are involved in the local deferment step (and hence the subsequent jump process).

A.3 Appendix: derivation of primary particle transport rate

It is desired to show that the primary particle flow rate for a linear network of constant mass, constant volume compartments has the form

$$\left.\frac{\mathrm{d}N_{\mathrm{pp}}(z)}{\mathrm{d}t}\right|_{\mathrm{transport}} = \begin{cases} \dfrac{\dot{m}_{\mathrm{feed}} V_{\mathrm{samp}}(z,t)}{V_{\mathrm{real}}(z)\rho_s \nu_{\mathrm{pp}}} - \dfrac{N_{\mathrm{pp}}(z,t)}{\tau(z)}, & \text{if } z = 1, \\ \dfrac{V_{\mathrm{real}}(z-1)}{V_{\mathrm{real}}(z)} \dfrac{V_{\mathrm{samp}}(z)}{V_{\mathrm{samp}}(z-1)} \dfrac{N_{\mathrm{pp}}(z-1,t)}{\tau(z-1)} - \dfrac{N_{\mathrm{pp}}(z,t)}{\tau(z)}, & \text{otherwise.} \end{cases} \tag{A.25}$$

A component balance on the primary particles based on the transport processes (inflow and outflow) is

$$\left.\frac{\mathrm{d}N_{\mathrm{pp}}(z)}{\mathrm{d}t}\right|_{\mathrm{transport}} = R_{\mathrm{inflow,pp}}(z,t) - R_{\mathrm{outflow,pp}}(z,t), \tag{A.26}$$

where $R_{\mathrm{inflow,pp}}(z,t)$ and $R_{\mathrm{outflow,pp}}(z,t)$ are the rates of primary particle inflow and outflow (number based) to/from the sample volume for compartment z, respectively. One wishes to define the forms of both terms of the RHS of (A.26) $\forall\, z \in \mathbb{L}$.

Firstly, consider the outflow term in (A.26). Using the mass-based definition of residence time, one can write the mass outflow rate of primary particles from the sample volume of compartment z as

$$\dot{m}^{\mathrm{SV}}_{\mathrm{pp,outflow}}(z) = \frac{M^{\mathrm{SV}}_{\mathrm{pp}}(z,t)}{\tau(z)}, \tag{A.27}$$

where $M^{\mathrm{SV}}_{\mathrm{pp}}(z,t)$ is the total mass hold-up of primary particles in the sample volume for compartment z.

Hence, the rate of primary particle outflow from the sample volume of compartment z is

$$R_{\text{outflow,pp}}(z,t) = \frac{\dot{m}^{\text{SV}}_{\text{pp,outflow}}(z)}{\rho_{\text{s}} v_{\text{pp}}} \tag{A.28}$$

$$= \frac{M^{\text{SV}}_{\text{pp}}(z,t)}{\rho_{\text{s}} v_{\text{pp}} \tau(z)}. \tag{A.29}$$

The total mass hold-up of primary particles can be written as

$$M^{\text{SV}}_{\text{pp}}(z,t) = N_{\text{pp}}(z,t)\rho_{\text{s}} v_{\text{pp}}. \tag{A.30}$$

It follows from (A.29) and (A.30) that

$$R_{\text{outflow,pp}}(z,t) = \frac{N_{\text{pp}}(z,t)}{\tau(z)} \quad \forall z \in \mathbb{L}. \tag{A.31}$$

Moving on to the inflow term in the RHS or (A.26), consider the first reactor in the network i.e. $z = 1$. Since the mass feed to this compartment consists purely of primary particles, the mass feed rate to the physical first compartment is simply the operating mass feed rate i.e.

$$\dot{m}_{\text{pp,inflow}}(1) = \dot{m}_{\text{feed}}. \tag{A.32}$$

Thus, the mass feed rate of primary particles into the first compartment with sample volume $V_{\text{samp}}(z,t)$ is

$$\dot{m}^{\text{SV}}_{\text{pp,inflow}}(1,t) = \dot{m}_{\text{pp,inflow}}(1)\frac{V_{\text{samp}}(1,t)}{V_{\text{real}}(1)} \tag{A.33}$$

$$= \dot{m}_{\text{feed}}\frac{V_{\text{samp}}(1,t)}{V_{\text{real}}(1)}. \tag{A.34}$$

The rate of primary particle inflow (number based) into the sample volume of the first compartment is then

$$R_{\text{inflow,pp}}(1,t) = \frac{\dot{m}^{\text{SV}}_{\text{pp,inflow}}(1,t)}{\rho_{\text{s}} v_{\text{pp}}} \tag{A.35}$$

$$= \frac{\dot{m}_{\text{feed}} V_{\text{samp}}(1,t)}{V_{\text{real}}(1)\rho_{\text{s}} v_{\text{pp}}}. \tag{A.36}$$

Together, (A.26), (A.31) and (A.36) prove (A.25) for the case $z = 1$.

In order to formulate an expression for $R_{\text{inflow,pp}}(z,t)\ \forall\, z \neq 1$, one first enforces continuity (in terms of the primary particle phase) across the boundary between two compartments. This requires that the equality

$$R^{\text{real}}_{\text{inflow,pp}}(z,t) = R^{\text{real}}_{\text{outflow,pp}}(z-1,t)\ \ \forall\, z \neq 1 \tag{A.37}$$

be satisfied $\forall\, z \in \mathbb{L}, z > 1$, where $R^{\text{real}}_{\text{inflow,pp}}(z,t)$ and $R^{\text{real}}_{\text{inflow,pp}}(z,t)$ are the number flowrate of primary particles into and out of the physical compartment with indices z and $z-1$, respectively.

Suppose that the physical compartment z can be constructed from $n(z,t)$ identical sample volumes of size $V_{\text{samp}}(z,t)$. Applying the same logic to $z-1$ one may write (A.37) as

$$n(z,t)R_{\text{inflow,pp}}(z,t) = n(z-1,t)R_{\text{outflow,pp}}(z-1,t)\ \ \forall\, z \neq 1. \tag{A.38}$$

Since all sample volumes are identical, one may also write

$$n(z,t) = \frac{V_{\text{real}}(z)}{V_{\text{samp}}(z,t)}. \tag{A.39}$$

Substitution of (A.39) into (A.38) and re-arranging for $R_{\text{inflow,pp}}(z,t)$ yields

$$\underset{z\in\mathbb{L},\ z>1}{R_{\text{inflow,pp}}(z,t)} = \frac{V_{\text{real}}(z-1)}{V_{\text{real}}(z)}\frac{V_{\text{samp}}(z)}{V_{\text{samp}}(z-1)}R_{\text{outflow,pp}}(z-1,t). \tag{A.40}$$

Using the expression for $R_{\text{outflow,pp}}$ in (A.31) in (A.40) gives

$$\underset{z\in\mathbb{L},\ z>1}{R_{\text{inflow,pp}}(z,t)} = \frac{V_{\text{real}}(z-1)}{V_{\text{real}}(z)}\frac{V_{\text{samp}}(z)}{V_{\text{samp}}(z-1)}\frac{N_{\text{pp}}(z-1,t)}{\tau(z-1)}, \tag{A.41}$$

which, combined with (A.26) and (A.31), completes the derivation.